THE UNIVERSITY OF
WARWICK

University of Warwick institutional repository: http://go.warwick.ac.uk/wrap

A Thesis Submitted for the Degree of PhD at the University of Warwick

http://go.warwick.ac.uk/wrap/71038

This thesis is made available online and is protected by original copyright.

Please scroll down to view the document itself.

Please refer to the repository record for this item for information to help you to cite it. Our policy information is available from the repository home page.

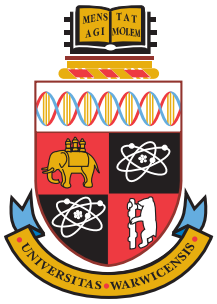

The role of gap junctions in the excitability of the myometrial smooth muscle network

by

Rachel Emma Sheldon

Thesis

Submitted to the University of Warwick

for the degree of

Doctor of Philosophy

in

Mathematical Biology and Biophysical Chemistry

Supervisors: Dr Hugo A. van den Berg, Dr Andrew M. Blanks, and Dr Anatoly Shmygol

MOAC Doctoral Training Centre

December 2014

THE UNIVERSITY OF WARWICK

In loving memory of Grandma

Contents

List of Figures

List of Tables

Abbreviations

ADP	Adenosine 5'-diphosphate
ATP	Adenosine 5'-triphosphate
AV Node	Atrioventricular Node
BVP	Bonhoeffer-van der Pol
cAMP	3'-5'-cyclic adenosine monophosphate *or* cyclic AMP
cDNA	Complementary Deoxyribonucleic Acid
Cx40	Connexin-40
Cx43	Connexin-43
Cx45	Connexin-45
DAG	Diacylglycerol
EHG	Electrohysterogram
EMG	Electromyogram
FHN	FitzHugh-Nagumo
FSH	Follicle Stimulating Hormone
GHK	Goldman-Hodgkin-Katz
GnRH	Gonadotropin-Releasing Hormone
GRP	Gastrin-Releasing Peptide
hCG	Human Chorionic Gonadotropin
HH	Hodgkin-Huxley
IP_3	Inositol 1,4,5-trisphosphate
LCM	Laser-Capture Microdissection
LH	Luteinizing Hormone
MMP	Matrix Metalloproteinase

MRDTI	Magnetic Resonance Diffusion Tensor Imaging
PGC	Primordial Germ Cell
PIP_2	Phosphatidylinositol 4,5-bisphosphate
PKA	Protein Kinase A
PKC	Protein Kinase C
PPH	Postpartum Hæmorrhage
RIN	RNA Integrity Number
RMP	Resting Membrane Potential
RNA	Ribonucleic Acid
ROC	Receptor-Operated Channel
SD	Standard Deviation
SEM	Standard Error of the Mean
SP	Substance P
SR	Sarcoplasmic Reticulum
VIP	Vasoactive Intestinal Polypeptide

Acknowledgements

First and foremost, I would like to thank my supervisors Dr Hugo van den Berg, Dr Andrew Blanks, and Dr Anatoly Shmygol for all of their advice and direction throughout my PhD.

Thank you to Prof. Alison Rodger and the staff in the Molecular Organisation and Assembly in Cells (MOAC) Doctoral Training Centre for their support over the last 4 years. I would like to give particular thanks to the MOAC 2010 intake and the Reproductive Health lab group for making my MSc and PhD years so enjoyable. Thank you also to the Engineering and Physical Sciences Research Council (EPSRC) for funding my research.

I am very grateful to Alexander Parker for his kindness and support. Thank you for keeping me focused and for always encouraging me to reach my full potential.

I could not have completed this thesis without the support from my family. Thank you to my Mum, Dad, Henry, and Faye for always being at the end of a phone and being willing to offer a helping hand. A very special thank you to my Mum and Dad for helping me see the bigger picture.

This thesis is for my Grandma, who would have been so proud to see it completed.

Declarations

The work presented in this thesis is entirely original and my own work, except where acknowledged in the text. I confirm that this thesis has not been submitted for a degree at another University. The work in Chapter 2 builds upon work carried out in mini-projects as part of my MOAC MSc degree (awarded January 2011), and Marc Baghdadi's MOAC MSc degree (awarded January 2011).

All figures were drawn by myself. Illustrations adapted from previously published figures are indicated in the captions.

Chapter 2 was published as:
Sheldon, R.E., Baghdadi, M., McCloskey, C., Blanks, A.M., Shmygol, A. & van den Berg, H.A. 2013 Spatial heterogeneity enhances and modulates excitability in a mathematical model of the myometrium. *J. R. Soc. Interface*, **10**(86), 20130458.

Chapter 3 was published as:
Sheldon, R.E., Mashayamombe, C., Shi, S-Q., Garfield, R.E., Shmygol, A., Blanks, A.M. & van den Berg, H.A. 2014 Alterations in gap junction connexin43/connexin45 ratio mediate a transition from quiescence to excitation in a mathematical model of the myometrium. *J. R. Soc. Interface*, **11**(101), 20140726.

Abstract

Dysfunction of the myometrium is a major contributor to preterm labour. The current limitations to effective management of preterm labour is in large part due to our, as yet, incomplete insight into the mechanisms that underlie uterine excitability. The uterus goes through a period of activation towards the end of pregnancy during which the myometrium develops the ability to deliver the baby. Gap junctions are among the most important molecular entities involved in this activation process.

In this thesis, a mathematical model based on FitzHugh-Nagumo dynamics is used to study the role that gap junctions play in controlling the excitability of the myometrium. Spatial heterogeneity is introduced into the network through stochastic assignment of coupling strengths based on physiological statistics. It is demonstrated that heterogeneity amplifies the ability of a locally applied stimulus to generate global activity and that the ability of the stimulus to excite the network is strongly dependent on the local spatial correlation structure of the couplings. In networks driven by a pacemaker cell, large coupling strengths preclude activity by reducing the frequency of the stimulating oscillations.

The model is extended to incorporate voltage-dependent gap junctions. It is established in the literature that gap-junctional conductance is dependent on the transjunctional voltage of neighbouring myocytes. Two conductance relationships have been observed corresponding to gap junctions composed of connexin-43 or connexin-45 proteins. It is demonstrated here that networks with only connexin-45 proteins are unable to exhibit global excitability whereas networks with connexin-43 proteins always display full activity. The mathematical models are supported by analysis of human and rat RNA expression data which shows that connexin-45 is down-regulated at term. It is hypothesised that connexin-45 blocks activity in the uterus throughout gestation, and is down-regulated at term to allow the uterus to deliver the powerful contractions associated with labour.

Chapter 1

Introduction

The aim of this thesis is to develop an understanding of the way in which gap junctions govern the excitability of the myometrial smooth muscle network. The excitability of the myometrium is closely linked to the contraction-relaxation cycle of the smooth muscle cells of the uterus (Marshall, 1962). While the process of uterine contraction is well understood, relatively little is known about the way the uterus prepares for labour (Aguilar & Mitchell, 2010). A lack of understanding of the mechanisms behind contractility could preclude proper diagnosis and treatment of preterm labour and postpartum hæmorrhage.

1.1 Clinical background

The distribution of the length of human pregnancies has a strong negative skew with a mean of around 280 days and a standard deviation of approximately 10 days (Kieler *et al.*, 1995). A preterm birth is defined as a delivery before 37 weeks gestation. Globally, 15 million babies are born prematurely each year (Blencowe *et al.*, 2012) and 1 million of these babies do not survive as a direct result of their gestational immaturity (World Health Organization, 2013) making prematurity the leading cause of newborn mortality worldwide. Babies that survive preterm birth may face disabling lifelong conditions such as reduced cognitive abilities as well as problems with vision and hearing. Despite medical advances, it remains the case that only 12 – 13 % of babies born between 22 and 26 weeks gestation will be alive at the age of $2\,{}^{1}/_{2}$ years (Wood *et al.*, 2000).

In the UK, 40 % of preterm births do not have an identified cause (Macdonald & Magill-Cuerden, 2011). The large number of spontaneous preterm labour and preterm births mean that reliable prediction and prevention could have a huge beneficial impact. However, this poses a considerable challenge. Treatment of preterm labour focuses on inhibition of uterine contractions and prevention of cervical dilation while the mother is still in the early stages of labour (Macdonald & Magill-Cuerden, 2011). The aim is to delay delivery long enough to allow for the opportunity to administer steroids to the mother to promote the development of the infant's lungs. The infant mortality rate per 1000 live births in England and Wales as a function of gestational age is shown in Figure 1.1 (Office for National Statistics, 2009 and 2013). Gestational age is recorded as completed weeks *in utero* as estimated by the mother. Birth weights were checked for consistency with gestational age; data where birth weights were considered to be inconsistent were not included in the graph. The steepness of the curve around 24 weeks gestation suggests

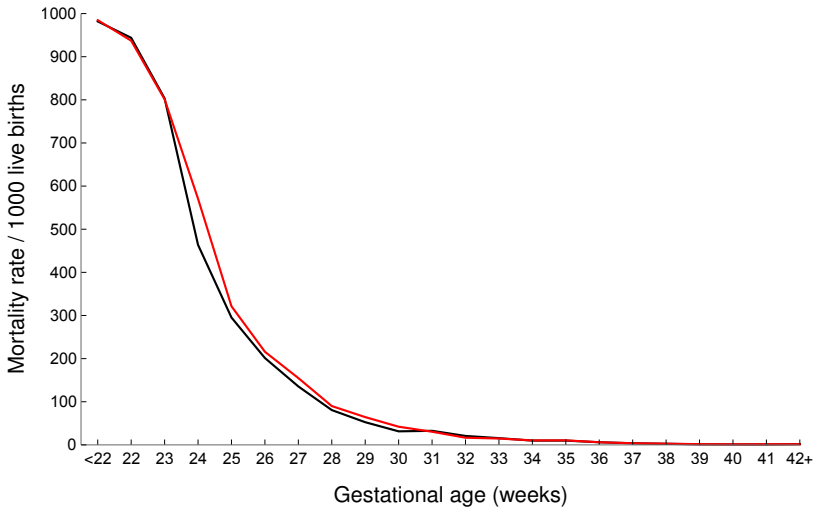

Figure 1.1: Infant mortality rate per 1000 live births in England and Wales by gestational age. Data from 2006 are shown in red, and data from 2011 are shown in black. Data from outside this time period are not available. Gestational age is recorded as completed weeks *in utero*. In most cases, a baby is not resuscitated when born before a gestation of 23 weeks. Data for gestational ages under 22 weeks only include births where birth weight was under 1000 g. Birth weights over 1000 g were considered to be inconsistent with the gestational age. Based on data published by the UK government (Office for National Statistics, 2009 and 2013).

that extending a pregnancy by even one week at this stage can greatly improve the chance of survival and reduce neonatal complications. In the face of the prevalence of preterm birth and its importance as a clinical problem, our knowledge of the mechanisms governing uterine contraction remains remarkably limited (Aguilar & Mitchell, 2010).

Whereas preterm birth is due to the uterus contracting when it should not be contracting, postpartum hæmorrhage (PPH) is, in a sense, the converse problem, where the muscle fails to contract when it should be contracting. Failure to contract after the placenta has been delivered may lead to severe loss of blood through the wound left by the placenta. PPH is the leading cause of maternal mortality in low-income countries and accounts for nearly a quarter of all maternal deaths worldwide (Khan *et al.*, 2006; Campbell *et al.*, 2006). While advanced maternal age and obesity have been demonstrated to increase the likelihood of PPH (Combs *et al.*, 1991; Stones *et al.*, 1993; Bais *et al.*, 2004; Magann *et al.*, 2005), not every occurrence is expected or avoidable (Sherman *et al.*, 1992).

The contractile component of the uterine wall is the myometrium, which consists of layers of smooth muscle cells. The myometrium undergoes a period of activation prior to labour where the muscle becomes more excitable; that is, it becomes more susceptible to stimulation by the pro-contractile hormones (Lye *et al.*, 1998). The smooth muscle cells are themselves excitable; an individual cell is considered to be excitable if a small stimulus (such as a current input) triggers a large response before returning to rest. Developing a greater understanding of the function of the myometrium is an important part of improving diagnosis and management of preterm labour and PPH. The two key aspects in this regard are the way that activity is triggered and the way in which it spreads through the smooth muscle cell network.

1.2 Development of the female reproductive system

The mammalian urogenital system (comprising the kidneys, gonads, and associated tracts) begins to be formed during early embryogenesis, shortly after gastrulation, in which the early embryo is reorganised into a structure with three germ layers: the ectoderm, the mesoderm, and the endoderm (Sadler, 2012).

In the blastocyst stage of development (Figure 1.2a), the embryo consists of an inner cell mass and surrounding trophectoderm. By gestational day 9, the inner cell mass has differentiated into a primitive endoderm (the hypoblast) and primitive ectoderm (the epiblast); (Figure 1.2b). Gastrulation begins with the formation of the primitive streak as an invagination of the epiblast cells (Figure 1.2c). The first cells to invaginate and displace the hypoblast form the endoderm which becomes the innermost layer of the embryo. The next layer to form is the mesoderm which is made up of invaginating cells between the newly formed endoderm and the epiblast. The cells that remain in the epiblast form the ectoderm: the outermost layer of the embryo (Figure 1.2d). As development progresses, the mesoderm can be further subdivided into cardiac, axial, paraxial, intermediate, and lateral-plate mesoderm (Figure 1.2e). With the exception of cardiac mesoderm, the layers are named according to their position from the centre of the embryo. The cells in this trilaminar structure form all of the tissues and organs in the embryo.

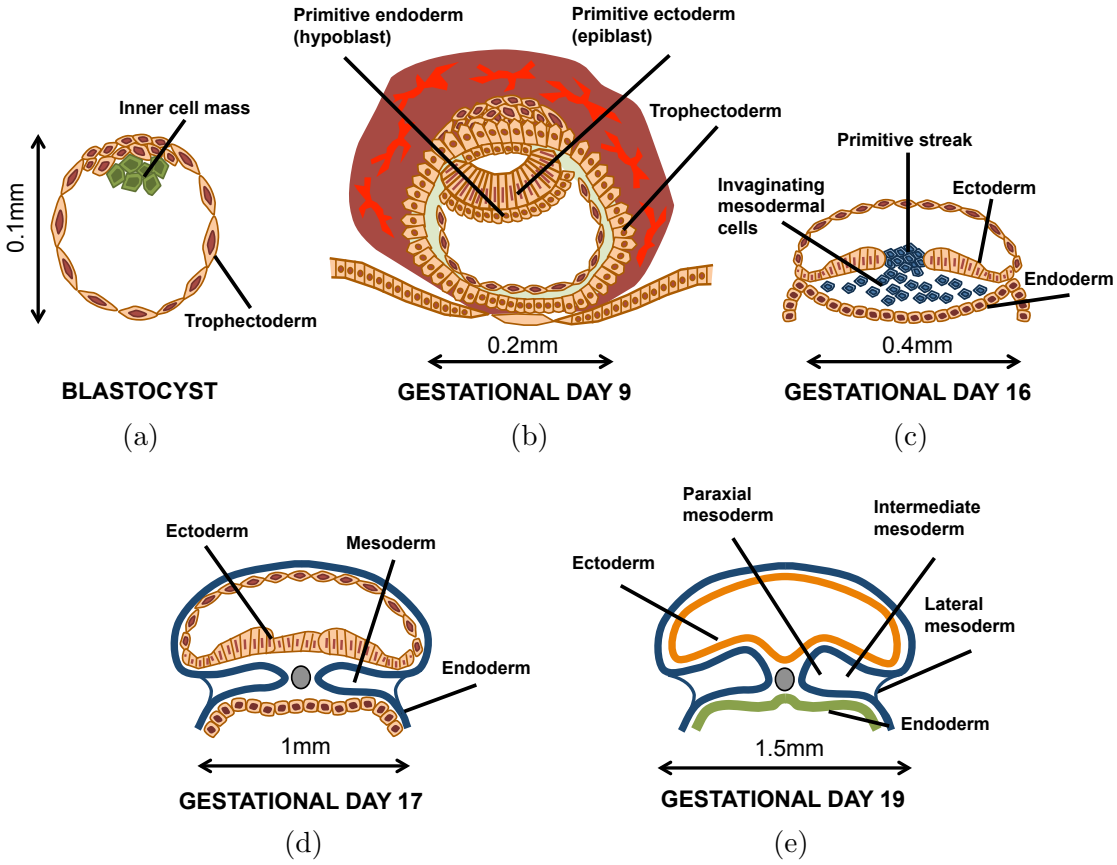

Figure 1.2: Two-dimensional cross-section of the development of the early human embryo as established by electron microscopy. (a) The blastocyst stage. The embryo is made up of an inner cell mass and the trophectoderm; (b) gestational day 9. The inner cell mass differentiates into the hypoblast and epiblast, and has now implanted into the uterine wall; (c) gestational day 16 (uterine wall not shown for clarity). The primitive streak appears in the epiblast. Invaginating epiblast cells displace the hypoblast to form the endoderm and the mesoderm; (d) gestational day 17. Cells that do not ingress through the streak form the ectoderm; (e) gestational day 19. The mesoderm can be further subdivided into layers including the paraxial, intermediate, and lateral mesoderm. Adapted from Pansky (1982).

The endoderm forms the inner lining of the gastrointestinal tract, the respiratory tract, the lining of the thyroid gland and thalamus, the epithelium of the auditory system, and the urinary bladder and part of the urethra (Figure 1.3a); the mesoderm develops into the heart, connective tissue, the kidneys, the reproductive system, skeletal muscle, and the skeleton (Figure 1.3b); the ectoderm forms the central nervous system and the epidermis of the skin (Figure 1.3c); (Coward & Wells, 2013).

(a) (b) (c)

Figure 1.3: Derivatives of the germ layers (a) The endoderm (green) develops into the lining of the gastrointestinal tract, the reproductive tract, the lining of the endocrine glands, the epithelium of the auditory system, and the urinary bladder and part of the urethra; (b) the mesoderm (blue) forms the heart, connective tissue, kidneys, reproductive system, skeletal muscle, and the skeleton; (c) the central nervous system and epidermis of the skin are derived from the ectoderm (orange). Adapted from Pansky (1982).

The following discussion of the development of the urogenital system is adapted from Sadler (2012) and Coward & Wells (2013), unless otherwise stated. The urinary and genital systems are derived from the intermediate mesoderm that runs along the length of the embryo. The urogenital system is split into three segments from anterior to posterior: the pronephros, mesonephros, and metanephros (Figure 1.4). These segments lie along the Wolffian ducts which are the continuous tubes that run along the length of the early embryo. The pronephros is non-functional in amniotes (*i.e.* birds, mammals, and reptiles) and regresses during development (Howland, 1916). However, in some primitive fish, the pronephros is still functional and provides an osmoregulatory role (Tytler *et al.*, 1996). The mesonephros initially performs the role of an excretory organ, but ultimately develops into the gonads. The metanephros forms a permanent kidney through an interaction

between the Wolffian duct and metanephric mesenchyme.

The gonads first appear as genital ridges made up of somatic cells from the mesonephros and primordial germ cells (PGCs). The PGCs migrate from the yolk sac, to the wall of the gut, and then to the dorsal body wall where they settle either side of the midline (Schoenwolf *et al.*, 2008). The ridges differentiate into testes or ovaries, depending on the chromosomal sex of the embryo.

The symmetrical Müllerian ducts are formed from cells located at the anterior end of the mesonephros. These ducts run parallel to the Wolffian ducts for the length of the mesonephros, before turning towards the midline and stretching towards the cloaca (Figure 1.4). In a female embryo, the pair of Müllerian ducts differentiate into the oviducts, uterus, cervix, and upper part of the vagina (Cunha, 1975), whereas the Wolffian ducts regress. If the embryo is genetically male, the Müllerian ducts regress and it is the Wolffian ducts that differentiate to form the reproductive tracts.

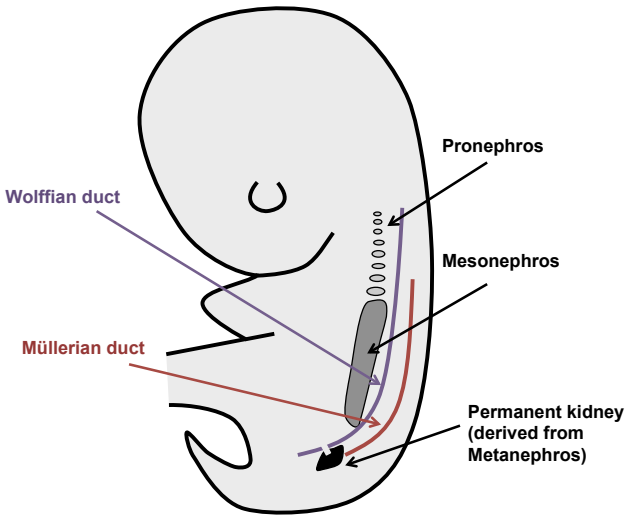

Figure 1.4: The origin of the urogenital system. The urogenital system can be divided into the pronephros, mesonephros, and metanephros. The developing reproductive tracts are the Wolffian and Müllerian ducts. If the embryo is genetically male, the Wolffian ducts will differentiate, and the Müllerian ducts will regress. If the embryo is female, it is the Müllerian ducts that differentiate to form the oviducts, uterus, cervix, and upper part of the vagina. The gonads develop on the surface of the mesonephros. Adapted from Coward & Wells (2013).

1.3 Structure of the female reproductive system

The female reproductive system of every mammal includes the Fallopian tubes, uterus, cervix, and vagina, with the morphology of these depending on the species (Gartner & Hiatt, 2009). Four different uterine structures have been described in mammals (Figure 1.5). The differences in morphology are dictated by the degree of Müllerian duct fusion in embryogenesis (Feldhamer *et al.*, 2007). Marsupials, rodents, and lagomorpha (such as rabbits, hares, and pika) have duplex uteri (Figure 1.5a) since little or no Müllerian duct fusion occurs in these species. A duplex uterus consists of two distinct 'horns,' each with a Fallopian tube and a cervix. Domestic animals tend to exhibit more extensive Müllerian

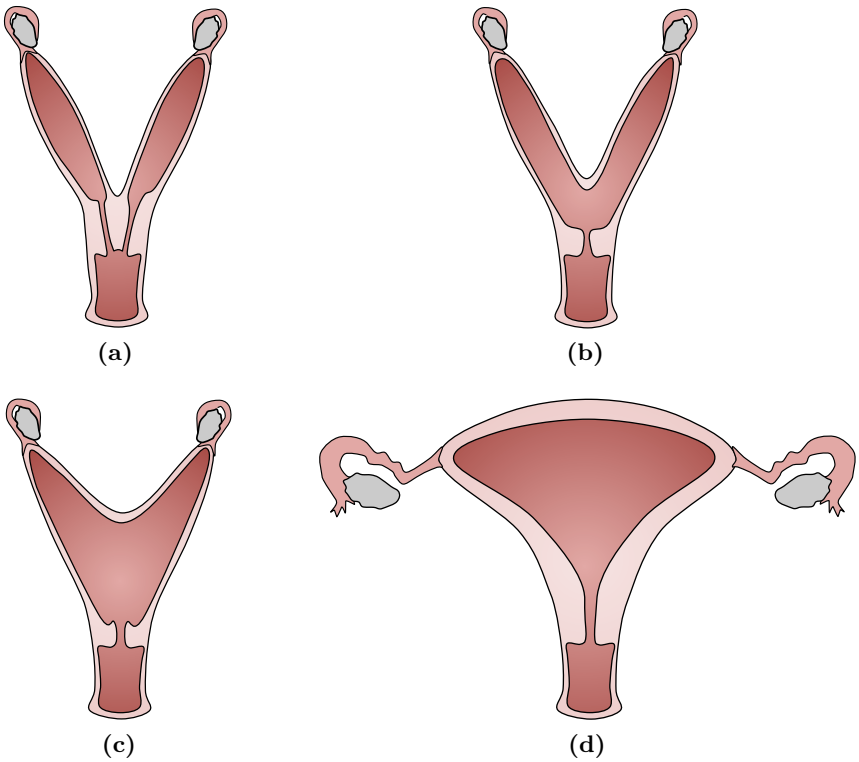

Figure 1.5: The four uterine structures observed in mammals. (a) A duplex uterus has two uteri and two cervices; (b) a bicornate uterus has two uteri but one cervix; (c) a bipartite uterus has distinct upper cavities, but the lower parts form a single structure; (d) a simplex uterus is a single organ with a convex uterine cavity.

duct fusion. The result can be a bicornate uterus (Figure 1.5b) in which the Müllerian ducts have partially fused posterially, the upper parts of the uterus remaining distinct but the lower parts forming a single structure. Bicornate uteri are found in dogs, pigs, and primates. Cats and ruminants (such as cows and sheep) have a bipartite uterus (Figure 1.5c) where the two uteri are separate for most of their length, but share a cervix. Humans and higher primates are unusual among mammals in that they have a 'simplex' uterus where the Müllerian ducts have fused more completely and the entire uterus has an undivided cavity (Figures 1.5d and 1.6). Mammals with a simplex uterus, and larger mammals such as cattle, horses, and elephants typically have singleton pregnancies, whereas smaller mammals will usually have multiparous births.

The human uterus is divided into two main components: the uterus proper and the ovaries,

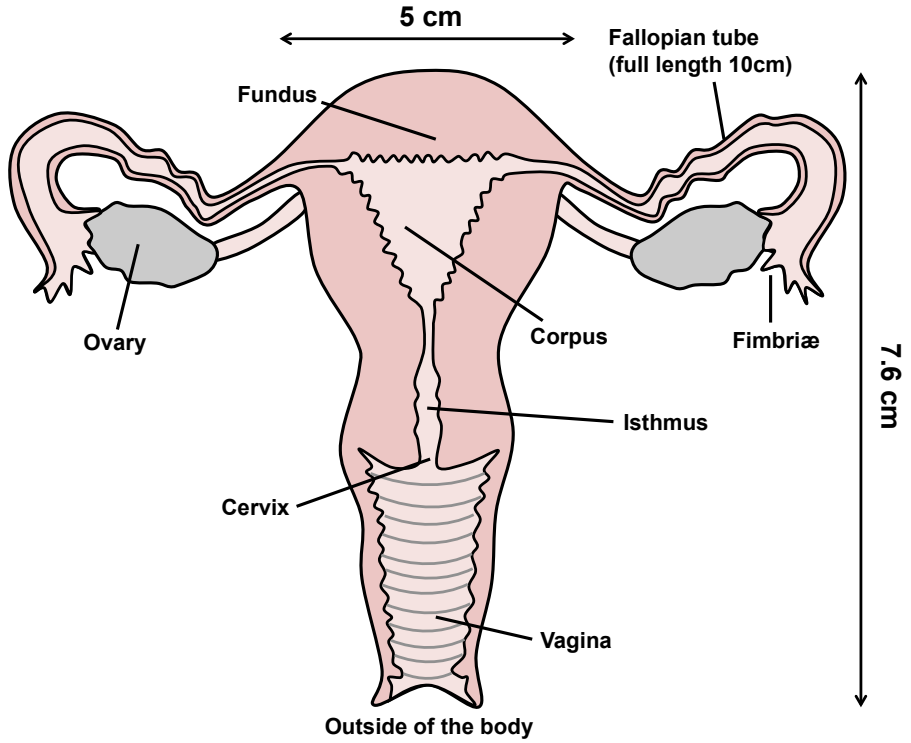

Figure 1.6: The non-gravid, post-pubescent human female reproductive system. The locations of the ovaries, Fallopian tubes, fimbriæ, fundus, corpus, isthmus, cervix, and vagina are labelled.

which are connected by the Fallopian tubes (Figure 1.6). The Fallopian tubes are embedded in the uterine wall and run diagonally upward from the uterine cavity, connecting the body of the uterus to the ovaries. The walls of the Fallopian tubes are made up of a muscular outer coat and an inner mucous membrane. The muscular layer can be further subdivided into an outer longitudinal layer and an inner circular layer. These alternately oriented muscles cooperate to generate peristaltic rhythmic contractions which vary in magnitude and frequency throughout the maturation of a Graafian follicle within an ovary. Fallopian tube contractions are most frequent and intense when an ovum has been released from an ovary and is travelling towards the uterine cavity.

The uterus itself can be divided into the cervix, the isthmus, the corpus, and the fundus (see Figure 1.6). The uterine wall consists of three distinct layers: the perimetrium, the myometrium, and the endometrium (Coward & Wells, 2013). The perimetrium is the outermost serosal layer of the uterus, made up of mesothelium and a layer of connective tissue. The myometrium is the thickest layer of the uterus consisting of interconnected smooth muscle cells derived from the mesoderm. Ultrasound and intrauterine pressure studies have demonstrated that the smooth muscle cells contract from cervix to fundus throughout most of the menstrual cycle, reaching a peak in magnitude at ovulation, and from fundus to cervix during menstruation and in labour (Bulletti *et al.*, 2000). The myometrium will be discussed in more detail in Section 1.5. The endometrium is derived from the endoderm during embryogenesis and forms the innermost layer of the uterus. It can be further subdivided into the stratum functionalis and the underlying stratum basalis. The stratum functionalis receives the embryo during implantation. It undergoes cyclical changes in structure and function in response to hormonal changes in the body, as discussed below.

1.4 Function of the female reproductive system

The release of the ovum coincides with a maximum receptiveness of the uterine wall. This coordination in time is controlled by the cyclical rise and fall of hormones which form the menstrual cycle.

1.4.1 The menstrual cycle

The length of a menstrual cycle varies between women with a mean of 29.1 days and a standard deviation of 7.46 days (Chiazze Jr *et al.*, 1968). There is also variability within women with a standard deviation of 2.84 days for mean cycle length (Liu *et al.*, 2004). The cycle can be subdivided into the changes that take place in the ovaries and in the uterus. These changes are summarised in Figure 1.7.

Ovarian cycle An oocyte begins its development in a follicle in one of the ovaries. Low-frequency pulses (with one every 3 to 5 hours) of gonadotropin-releasing hormone (GnRH) in the pituitary during the first few days of the menstrual cycle result in an increase in follicle stimulating hormone (FSH) levels (Marshall *et al.*, 1993; Lüking Jayes *et al.*, 1997). An increase in FSH stimulates the maturation of several ovarian follicles. In most cases, one follicle will dominate and reach full maturity, at which time it is referred to as a Graafian follicle.

Halfway through the menstrual cycle, high-frequency pulses of GnRH (with a pulse approximately every 60 to 90 minutes) in the pituitary trigger a rise in luteinizing hormone (LH), leading to the release of an oocyte from the Graafian follicle (Marshall *et al.*, 1993; Lüking Jayes *et al.*, 1997). In most cases, the fimbriæ (see Figure 1.6) sweep the oocyte into the Fallopian tube ready for fertilisation. Once the oocyte matures, it is referred to as an ovum.

The high levels of FSH and LH induce the empty Graafian follicle to convert into a corpus luteum. The corpus luteum produces progesterone, which in turn triggers an increase in estrogen. If the ovum is not fertilised, the levels of FSH and LH begin to fall. The corpus luteum will then involute causing progesterone levels to fall as well. The fall in progesterone induces the expression of matrix metalloproteinases (MMPs) and suppresses the inhibitors of these enzymes. As a result, the endometrial tissue and extracellular matrix are therefore digested (Marbaix *et al.*, 1995, 1996; Kokorine *et al.*, 1996; Brosens & Gellersen, 2006; Brosens *et al.*, 2009; Brun *et al.*, 2009; Gaide Chevronnay *et al.*, 2009). The endometrial mucous covering is shed as a result, and removed from the uterus. The efflux of this material via the vagina is known as menstruation. The unfertilised ovum is swept along and removed from the uterus.

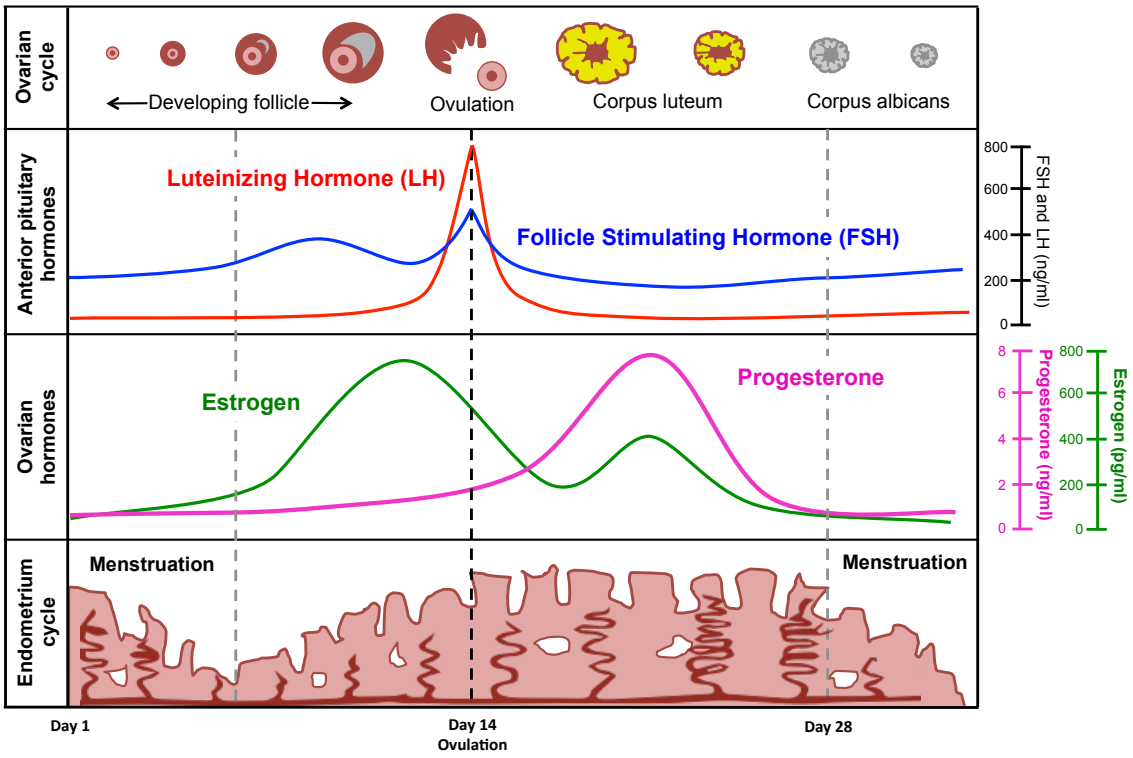

Figure 1.7: Hormonal changes during the menstrual cycle highlighting the changes in the ovary, the endometrium, and levels of the following hormones: luteinizing hormone (LH), follicle stimulating hormone (FSH), estrogen, and progesterone. Adapted from Wuttke (1987) and Gartner & Hiatt (2009).

If the ovum is fertilised, the resulting zygote begins to undergo embryogenesis and is moved by the cilia in the Fallopian tube towards the body of the uterus. The fertilised ovum takes around three days to reach the uterus, and may take a further three days to implant into the uterine wall, by which time it is referred to as a 'blastocyst.' The blastocyst produces the hormone human chorionic gonadotropin (hCG) which preserves the corpus luteum and, in turn, the secretion of progesterone which maintains the pregnancy. By the tenth week of gestation, the placenta has begun to produce the latter hormone and the corpus luteum degenerates into the corpus albicans (Wulff *et al.*, 2001).

Uterine cycle During the menstrual cycle, the endometrium undergoes a substantial transformation in which the uterus becomes receptive to the implantation of an embryo (Dey *et al.*, 2004; Brosens *et al.*, 2009). Once a Graafian follicle has developed in the ovaries, the increase in estrogen from the follicle causes the epithelial cells of the luminal stratum functionalis to proliferate. The post-ovulatory rise in progesterone triggers the decidualisation of the endometrium in which endometrial stromal cells are transformed into specialised secretory decidual cells (Dey *et al.*, 2004; Gellersen *et al.*, 2007). The progesterone increase halts the proliferation process, causes an influx of immune cells, and promotes angiogenesis (Brosens *et al.*, 1999; Gellersen & Brosens, 2003; Gellersen *et al.*, 2007). This new tissue state is preserved by constantly high progesterone levels. If a pregnancy occurs, the corpus luteum, and subsequently the placenta, continue to secrete progesterone to preserve the decidualised endometrium. If the ovum is not fertilised, the corpus luteum degenerates and accordingly progesterone levels fall. The fall in progesterone induces the MMPs to digest the stratum functionalis and its extracellular matrix leading to menstruation. After each cycle, the remaining stromal cells in the stratum basalis proliferate to regenerate the stratum functionalis (Coward & Wells, 2013).

1.4.2 Maintaining a pregnancy

The uterus protects the growing fœtus and its placenta during pregnancy. The production of progesterone by the placenta supports uterine quiescence by suppressing the genes in the myometrium that underlie uterine contractility. These genes regulate connexin-43, calcium channels, and calcium and oxytocin receptors (Petrocelli & Lye, 1993; Helguera *et al.*, 2002; Grazzini *et al.*, 1998). Additional effects of progesterone are the upregulation of the nitric oxide system which promotes muscle relaxation (Izumi *et al.*, 1993) and the suppression the release of pro-inflammatory cytokines and prostaglandins (Soloff *et al.*, 2011; Garfield *et al.*, 1998).

During the course of pregnancy, the uterus increases in volume 500-fold whilst accommodating the growing fœtus (Blackburn, 2007). The main component of this expansion is a 10-fold increase in cell size in the myometrial layer (hypertrophy) which is regulated by steroid hormones and mechanical distention. There is also an increase in cell number (hyperplasia) but, after implantation, this makes a far less important contribution (Afting & Schenk, 1978). Throughout the majority of pregnancy, the myometrial cells are poorly electrically connected, if at all (Garfield *et al.*, 1977). Therefore, any contractile activity is localised and not able to propagate through the network of cells, as demonstrated through electrohysterogram (EHG) and electromyogram (EMG) observations of the pregnant uterus (Buhimschi *et al.*, 1997). This is a key factor in global (organ-level) quiescence.

1.4.3 Parturition

In preparation for labour, the uterus undergoes functional changes that allow a transition from an inactive to an active state. These changes have been shown to comprise two major steps: a conditioning phase and active labour (Sadler, 2012) which have been characterised

by Garfield *et al.* (1998) as follows. The conditioning phase serves to prepare the cervix and uterus for labour. From 25 weeks gestation, the cervix begins to ripen. The inflammatory cascade is activated which includes the release of proinflammatory cytokines, an influx of white blood cells, the release of MMPs, a change in the synthesis of extracellular matrix proteins, an increase in collagen turnover, changes in the ratio of decorin to collagen, and an increase in extracellular fluid (Leppert, 1992, 1995; Rechnerger *et al.*, 1996). The dominant hormone involved in cervical ripening is progesterone, as is shown by the observation that ripening is promoted by the inhibition of progesterone (Chwalisz, 1994). However, while a decrease in progesterone is observed in most mammals at the end of pregnancy, cervical ripening begins much earlier in humans which points to the involvement of other mechanisms that are independent of progesterone. Humans, guinea pigs, and higher primates are unique in that a systemic progesterone withdrawal is not observed. Instead it is thought that a 'functional' progesterone withdrawal occurs in which the actions of progesterone are suppressed at term (Karalis *et al.*, 1996; Kalkhoven *et al.*, 1996; Casey & MacDonald, 1997; Thomson *et al.*, 1999; Mendelson & Condon, 2005). The exact mechanisms controlling this are not yet well understood (Zakar & Hertelendy, 2007). The other important humoral mechanisms include the prostaglandin PGE_2, inflammatory cytokines, and nitric oxide, all of which promote cervical ripening (Ito *et al.*, 1987; Osmers *et al.*, 1992; Kelly *et al.*, 1993; Kelly, 1994; Chwalisz *et al.*, 1994; Chwalisz, 1994).

Uterine changes as part of the conditioning phase occur over a much shorter timescale: from 37 weeks to term (Garfield *et al.*, 1998). In the myometrium there is an increase in the synthesis of connexin proteins, ion channels, and oxytocin and prostaglandin receptors. The elevated expression of these proteins increases the gap junction density and premature excitability of the muscle tissue. The inhibitory nitric oxide system is also down-regulated. The mechanisms through which these changes promote synchronised uterine contractility are discussed in Section 1.9.

The active phase of labour commences with synchronised uterine contractions which allow

the mother to deliver the baby (second stage of labour) and placenta (third stage of labour). Once active labour has started, delivery cannot be delayed for more than five days (Garfield *et al.*, 1998). It is therefore of paramount clinical importance to be able to identify preterm labour before active labour begins, in order to prolong gestation. Insufficient contractions are also of clinical importance. Without the contractions to shear off and expel the placenta in the third stage, severe blood loss can occur, a serious condition known as postpartum hæmorrhage.

1.5 The myometrium

The structure of the non-gravid human myometrium has been the subject of debate for a number of years. Goerttler (1968) suggested a two-layered myometrium with counter-rotating spirals of fibres based on studies using unstained myometrium sections viewed under crosslight and transmitted light with polarisation filters. In contrast, Wetzstein & Renn (1970) carried out experiments on hæmatoxylin-stained myometrium sections and proposed that the human myometrium could be subdivided into three poorly defined layers as follows. The inner myometrium (stratum subvasculare) lies immediately under the endometrium and consists of bundles of smooth muscle cells which are arranged concentrically around the longitudinal axis. This 'circular' layer is the only layer to display a clear muscle fibre orientation. The middle layer is the stratum vasculare in which the muscle fibres branch out and run in all directions. The stratum vasculare also contains fibroblasts, blood and lymphatic vessels, immune cells, and connective tissue. The outermost myometrial layer (the stratum supravasculare, or longitudinal layer) lies under the perimetrium and contains smooth muscle bundles organised into four tiers.

Weiss *et al.* (2006) used Magnetic Resonance Diffusion Tensor Imaging (MRDTI) to verify the structure proposed by Wetzstein & Renn (1970) and found data in broad agreement with this structure. The diffusion tensors suggested that fibres in the stratum subvasculare

run in a common direction, oriented circularly around the uterine cavity and endometrium. No clear orientation could be demonstrated in any other myometrial layer, with the exception of the cervical section of the uterus, in which clear circular and longitudinal layers were identified.

In contrast to the human myometrium, the myometrium of most mammals has oriented layers which are more distinct (Brody & Cunha, 1989a,b; McLaren *et al.*, 1996; Mueller *et al.*, 2006). The inner myometrium is made up of circularly oriented fibres and the outer myometrium consists of longitudinally oriented fibres (Figure 1.8).

1.5.1 Smooth muscle cells

Three types of muscle tissues are found in the body: cardiac, skeletal, and smooth muscle (Gartner & Hiatt, 2009). Cardiac muscle propels blood round the body, whereas

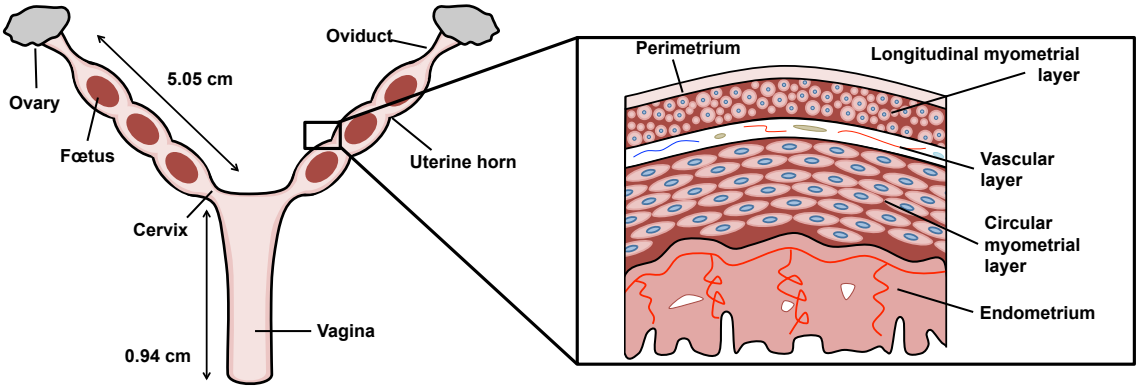

Figure 1.8: The rat reproductive system. (a) The duplex uterus of the rat (gross anatomy). Each horn has its own ovary and oviduct, and is able to support multiple pups. Dimensions as published by Muhammad *et al.* (2013); (b) the uterine wall (histological structure). The outermost layer is the perimetrium and the inner most layer is the endometrium. The rat myometrium has two distinct longitudinal and circular layers with a region of overlap bridging the gap. The uterine wall contains a vascular layer running between the longitudinal and circular layers. Cells increase in size 3-fold during pregnancy and have a volume of around $770\,\mu m^3$ at term (Shynlova *et al.*, 2010).

skeletal muscle is involved in bodily movement, and smooth muscle is found in the walls of nearly all visceral tissue that is arranged in the shape of tubes or bags, such as the bile duct, bladder, blood vessels, gut, myometrium, prostate, sphincter, and trachea (Mitchell & Peel, 2009). Common to all muscle tissue is their mesodermal derivation and their elongation parallel to their direction of contraction. Muscle cells contain a large number of mitochondria as well as the contractile elements actin and myosin. Skeletal and cardiac tissue are known as striated muscle since they have arrays of actin and myosin which create patterns of uniform banding along their length. The myosin arrays are the dark, anisotropic filaments which make up the 'A' band. The length of these filaments remain constant throughout a contraction with a length in a mammalian skeletal muscle cell of $\sim$1.54 μm (Dreizen *et al.*, 1984; Plonsey & Barr, 2007). The actin arrays are the light filaments which make up the 'I' band. In a relaxed skeletal muscle cell, the I band has a length of 2.05 μm (Plonsey & Barr, 2007). However, during a contraction the apparent length of the I band shortens as it passes underneath the A band. In contrast to skeletal and cardiac muscle, the contractile elements of smooth muscle tissue have an irregular arrangement making the tissue non-striated.

Smooth muscle cells are long and spindle-shaped (Figure 1.9a); in the non-pregnant human uterus, relaxed myocytes are around 5 μm in width and 50 μm in length (Blackburn, 2007). When contracted, the smooth muscle cells become much shorter and wider (Figure 1.9b). Eddinger & Meer (2001) showed that contracted rabbit stomach smooth muscle cells have a 3-fold decrease in length, and are approximately double the width of relaxed smooth muscle cells. Throughout pregnancy, the cells increase in size reaching a peak at the time of delivery with a 10-fold increase in volume when compared to their size at implantation (Afting & Schenk, 1978; Blackburn, 2007). The individual cells are grouped together into sheets or bundles by layers of connective tissue and gap junction proteins which link adjacent cells (Section 1.6). For most of gestation the uterus remains quiescent. The density of gap junctions in the network is low, as a result of which smooth muscle con-

tractions are kept localised (Garfield *et al.*, 1977). However, by the end of pregnancy, the gap junction density has dramatically increased and muscle cells are well-connected, which allows them to generate the synchronised contractions needed to deliver the fœtus.

The sarcoplasmic reticulum (SR) makes up between 2 and 7.5 % of the total volume of a smooth muscle cell (Alberts *et al.*, 2008b; Somlyo, 1980). The main functions of the SR are to store the calcium which activates the contractions of the cell and to act as a site for protein synthesis. In addition, uterine smooth muscle cells contain a plasma membrane, a single, elongated nucleus, myofilaments, microtubules, and various organelles. The plasma membrane of a smooth muscle cell is an 8 nm thick, bimolecular structure which provides a means of transmitting signals in an excitable cell (Singer & Nicolson, 1972; Matlib *et al.*, 1979). The majority of the cytoplasm consists of myosin and actin myofilaments which work together to generate muscular contractions after receiving a calcium signal. A

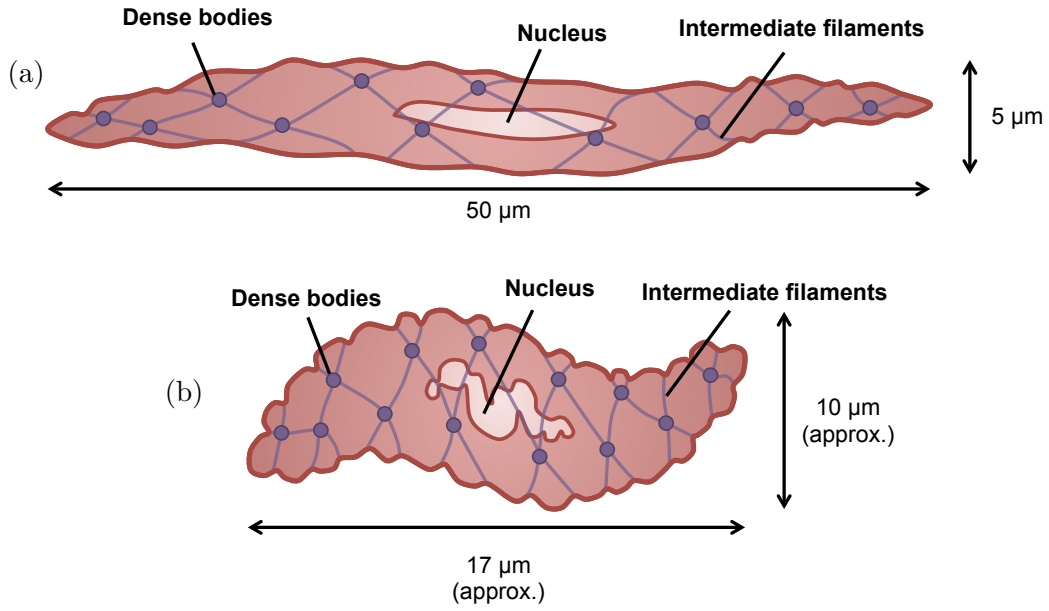

Figure 1.9: Smooth muscle cell contraction. (a) A relaxed smooth muscle cell is around 50 μm in length, and 5 μm in width; (b) a contracted smooth muscle cell is 3-fold shorter and twice as wide. Adapted from Gartner & Hiatt (2009).

third type of filament identified in uterine smooth muscle cells is the intermediate desmin filament (Aguilar & Mitchell, 2010). The intermediate filaments are attached at random throughout the inner surface of the smooth muscle cells at sites called 'dense bodies.'

Smooth muscle contains three main calcium regulatory proteins: calmodulin, caldesmon, and calponin (Aguilar & Mitchell, 2010). The most important protein for contractility is the calcium-binding protein calmodulin. Once bound to calcium, it activates the myosin light-chain kinase to trigger a contraction. Caldesmon enhances the ability of the SR to maintain tension by tethering the actin and myosin. Calponin is a load-bearing protein that inhibits the ATPase activity of myosin (discussed in Section 1.8). When calcium binds to calmodulin, calponin is phosphorylated and no longer inhibits the smooth muscle ATPase (Li *et al.*, 2012).

1.6 Gap junctions

Intercellular pores known as connexons have been identified between cells in almost every tissue type with the exception of fully developed skeletal muscle and mobile cells such as blood cells and immunocytes. In the uterus, connexons connect the myometrial smooth muscle cells and play a crucial role in synchronising contractions during labour (Garfield *et al.*, 1988). Each channel creates a 4 nm aperture which allows the passage of ions, small metabolites (under 1000 kDa in size), and electrical impulses between the cytoplasm of neighbouring cells (Alberts *et al.*, 2008c). The passage of electrical impulses through connexons causes the myometrium to behave as an excitable medium; that is, signals can be transmitted between cells with little damping. The contractions of adjacent smooth muscle cells can therefore synchronise during labour (Garfield *et al.*, 1988). The way in which this electrical activity is propagated between smooth muscle cells, and how this affects contractility is discussed further in Section 1.7.

Connexons are made up of connexin proteins which span the cell membrane (Figure 1.10). A hemichannel consists of a hexamer assembly of six connexin proteins; a hemichannel is contributed by each cell to form the connexon. Hundreds of connexon channels assemble along the cell membrane to form the gap junction plaque.

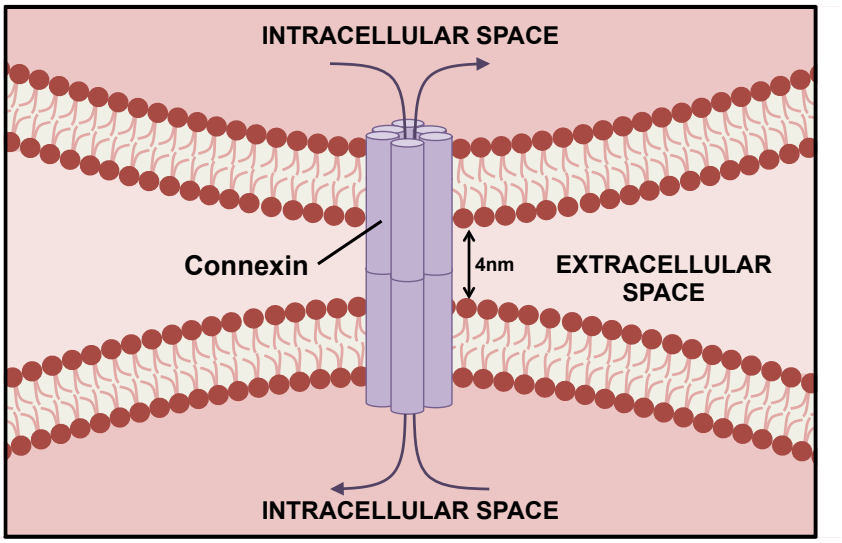

Figure 1.10: A connexon assembled between two neighbouring myometrial cells. Each cell contributes six connexin proteins to the channel. The pore formed by the connexin protein assembly allows the transfer of ions and metabolites between cells.

Many types of connexin protein exist; twenty connexin isoforms have been identified in human tissue (Willecke *et al.*, 2002). In the uterus, the most abundant of these is connexin-43 (Cx43), named for its molecular mass of 43 kD. Other prominent connexins in the uterus are connexin-40 (Cx40) and connexin-45 (Cx45). The gap junction plaque can be heterotypic in which each hemichannel can be made up of a hexmer of different connexin proteins (Sosinsky, 1995; Kilarski *et al.*, 2001). However, some connexin proteins are incompatible for a heterotypic junction; it has been shown that channels formed from Cx40 and Cx43 are not functional in either *Xenopus* oocytes or transfected mammalian cells (Bruzzone *et al.*, 1993; Elfgang *et al.*, 1995). Connexin proteins have very short half-lives of the order of several hours (Berthoud *et al.*, 2004; Laird, 2006). Thus, connexins are continually biosynthesised and degraded allowing connexin composition to be up- or

down-regulated throughout gestation.

Each connexin protein carries its own conductance which contributes to the total channel conductance. Conductance is the reciprocal of resistance; Kirchhoff's laws for parallel resistors can be used to determine the total resistance, R, and so total conductance, G, of the gap junction plaque:

$$G = \frac{1}{R} = \frac{1}{r_1} + \frac{1}{r_2} + ... + \frac{1}{r_n}, \tag{1.1}$$

where r_i is the resistance of connexon i in the n connexons making up the gap junction plaque. The resistance in the gap junction channel is lower than the membrane resistance and so charge will flow through the channel during an action potential (see Section 1.7.3). Therefore, the composition of the connexons directly affects the conductance of the gap junction plaque, and thereby its function.

At the start of pregnancy, as in the non-pregnant uterus, few gap junctions exist between uterine muscle cells (Miller *et al.*, 1989). However, the number of gap junctions increases dramatically in the days leading up to labour, reaching a peak at delivery (Cole & Garfield, 1985; Miller *et al.*, 1989) as indicated in Figure 1.11. During normal delivery, an individual cell will have around 1000 gap junctions which increase in diameter to around 250 nm (Garfield *et al.*, 1977). Within 24 hours of expulsion of the fœtus, the majority of these gap junctions has disappeared.

Gap junctions play a central role in the transition of the myometrium from a quiescent to an excitable state. The channels enable electrical signals to be transmitted throughout the myometrium and so allow the uterus to synchronise contractions in labour. The gap junction proteins are regulated primarily through endocrine mechanisms. In particular, the protein density is up-regulated by estrogen and prostaglandins, and down-regulated by progesterone. The permeability of the junctions is up-regulated by oxytocin, and down-regulated by relaxin. While an increase in the gap junction density increases tissue conductance, neurogenic and myogenic mechanisms are required to promote activity within

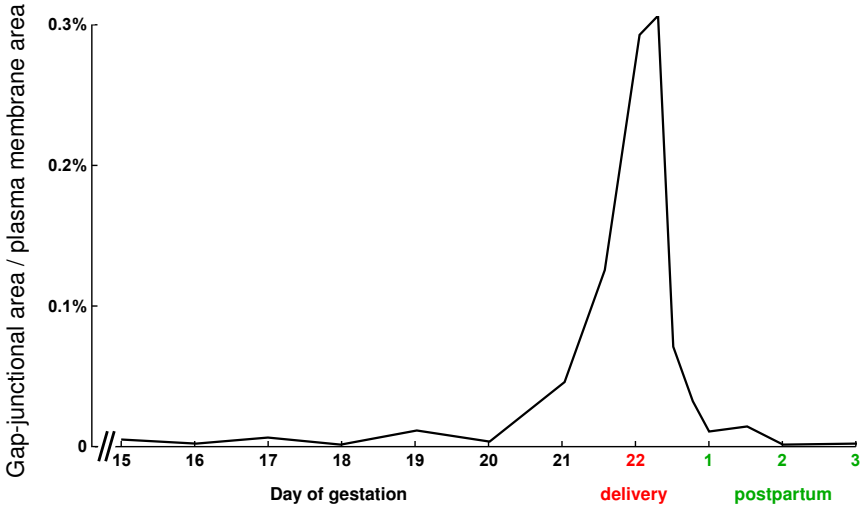

Figure 1.11: Gap-junctional area in rat myometrium from gestational day 15 to 3 days after delivery. Gap-junctional area is determined as percentage of plasma membrane area. The gap-junctional area stays low until gestational day 21, rapidly increases to a peak at delivery where gap junctions comprise 0.3 % of the plasma membrane area, and rapidly declines to a negligible proportion of the plasma membrane within 24 hours of delivery.

the cell. Myogenic mechanisms are a suggested intrinsic property of the cell which are much disputed in the literature (see Section 1.9.3). Neurotransmitters affect the quality and quantity of contractions; the expression of receptor nerve fibres for inhibitory neurotransmitters has been shown through tissue staining to decrease at the end of pregnancy in humans and rats (Thorbert, 1978; Marshall, 1981; Garfield, 1986). The excitability of the uterus is discussed in more detail in Section 1.7 and the modulation of uterine contractility is discussed further in Section 1.9.

1.7 Uterine excitability

The ability of the uterus to contract is a consequence of the underlying electrical activity of the myometrial cells (Wolfs & van Leeuwen, 1979; Anderson *et al.*, 1981). It was first established by Ringer (1882a,b, 1883a,b, 1884) that ions play a vital role in excitable tissue. In the case of uterine smooth muscle, excitation relies on the movement of calcium,

potassium, and to a lesser extent sodium and chloride ions, through their respective ionic channels (Fatt & Ginsborg, 1958). An influx of calcium depolarises the cell and triggers a muscle contraction whereas an efflux of potassium leads to repolarisation that causes cell relaxation. These phenomena indicate that the excitability of the uterus is modulated through ionic transport and relies on the gating properties of ion channels.

1.7.1 Ion channels

Ion channels are macromolecular pores that connect the cytosol to the cell exterior (Alberts *et al.*, 2008a). They are found in every cell and allow hydrated ions to diffuse rapidly across the lipid bilayer down their electrochemical gradient, namely down the potential and ionic concentration gradient. The ion channels are highly selective for specific ions (Figure 1.12). The pore is narrow enough to allow diffusing ions to come into contact with the channel wall, where its charge can be identified (Alberts *et al.*, 2008a). As such, the channel only permits ions of a certain charge and size to cross the membrane.

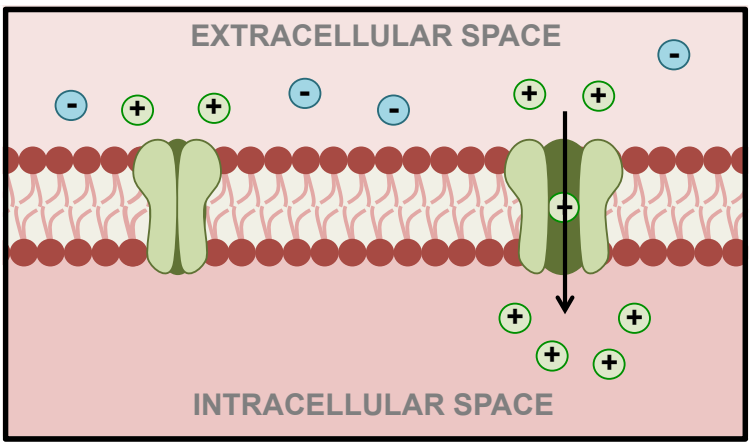

Figure 1.12: Gated ion channel for a membrane permeable to one ionic species. The pore on the left is closed, and no ions can pass through. The pore on the right is open, and selective for positively charged ions of the correct size. The pore is sufficiently narrow to allow the ion to come into contact with the channel wall where its charge can be identified.

1.7.1.1 Ion channel gating

Ion channel pores are not continually open; they are able to open and close rapidly in response to simuli. The pores can be gated (and, therefore, characterised) in one of three main ways; by a change in the voltage across the membrane, by mechanical stress, or by ligand binding. The following description of the types of ion channel gating is adapted from Hille (1992).

Voltage-gated ion channels are activated by a change in the membrane potential near the channel. The electrical field created across the membrane by a potential difference increases the probability of a conformational change in the channel which, in turn, may alter the shape of the channel proteins. A membrane depolarisation (in which the membrane potential becomes less negative, see Section 1.7) generally induces the pore to open, allowing a flux of ions down their electrochemical gradient. A further change in membrane potential may induce the pore to close and stop the ionic flux. In the smooth muscle cell, the channels that respond to changes in membrane potential include voltage-gated calcium, potassium, and sodium channels. Voltage-gated calcium channels come in two forms: 'L-type' which is activated for a long time (around 2000 ms) and has a large conductance of between 22 and 28 pS in 100 mM Ba^{2+}, and 'T-type' which is activated for a short time (approximately 100 times shorter than L-type channels) and has a smaller conductance of around 5 to 10 pS in 100 mM Ba^{2+} (Hagiwara *et al.*, 1975; Fishman & Spector, 1981; Fox *et al.*, 1991).

Ion channels activated by mechanical stress were first identified by Guharay & Sachs (1984). The channels respond to a membrane deformation such as a change in thickness or curvature. Consequently, the cells are able to detect stimuli such as vibration, pressure, and stretch (Patel *et al.*, 2010; Martinac, 2011; Del Valle *et al.*, 2012). The deformation causes a depolarisation of the cell membrane, which may trigger an action potential in an excitable cell. Stretch-induced calcium release has been demonstrated in smooth muscle

by Ji *et al.* (2002) and stretch-activated potassium channels have been identified in myometrial tissue (Tichenor *et al.*, 2005). Since it has been established that fœtal growth during pregnancy causes stretch of the myometrium (Shynlova *et al.*, 2010), it is likely that stretch-activated ion channels play an important part in the inhibition of labour throughout the majority of pregnancy, and the initiation of labour in late pregnancy (days 19 to 22 in the rat).

Ligand-gated ion channels open in response to the binding of a chemical messenger such as a hormone or neurotransmitter, at the extracellular domain. Messenger binding, and subsequent opening of the channel, causes a small depolarisation of the cell membrane of the order of 10 mV (Alberts *et al.*, 2008a). If the depolarisation is sufficient (typically around 20 mV for a smooth muscle cell), voltage-gated ion channels will open, which may trigger an action potential (Section 1.7.3). An important ligand-gated ion channel in smooth muscle is the P2X receptor channel which opens in response to adenosine 5'-triphosphate (ATP) binding (Benham & Tsien, 1987). The subsequent membrane depolarisation opens the voltage-gated calcium channels, allowing calcium ions to enter the cell. These chemical messengers are first messengers. Some ligand-gated ion channels rely on the binding of second messengers for activation; that is, they rely on intracellular signalling molecules released by the cell itself under agonist stimulation. For instance, inward-rectifying potassium channels rely on the second messenger phosphatidylinositol 4,5-bisphosphate (PIP_2) in order to be activated (Hilgemann & Ball, 1996; Fan & Makielski, 1997; Logothetis *et al.*, 2007). One such channel important in myometrial smooth muscle is Kir7.1 which plays a key role in inhibiting activity throughout gestation (McCloskey *et al.*, 2014). In mid-gestation, Kir7.1 expression is high which keeps the membrane potential of the myocytes hyperpolarised, that is, the membrane potential becomes more negative. Thus, the depolarising stimulus required to excite a cell is high. At term, a down-regulation of Kir7.1 removes the dampening of excitability observed in pregnancy.

1.7.1.2 Ionic pumps

A more essential method of ionic transportation is across the membrane against their electrochemical gradient (Hille, 1992). The ionic 'pumps' are membrane-spanning enzymes responsible for the active transport of ions in one of three ways (Alberts *et al.*, 2008a). Transporters mediate the movement of ions at a rate determined by the binding constant of the transporter to the ion, and maximum diffusion rate. If one ion is being transported down an electrochemical gradient, the channel is a uniporter (Figure 1.13). Coupled transporters use the free energy released during the downhill transport of one ion across the membrane, an energetically favourable process, to power the uphill transport of another ion across the membrane, an energetically unfavourable process. The ions could be being transported in the same direction, in which case the transporter is a symporter, or in opposing directions, where the transporter is an antiporter (Figure 1.13). One such antitransporter in the smooth muscle membrane is the sodium-calcium exchanger. One calcium ion is removed from the cell against its concentration gradient by coupling the transport with the influx of three sodium ions down their concentration gradient (Blaustein & Lederer, 1999). The sodium-calcium antiporter therefore maintains a quiescent environment within the muscle cell by keeping the intracellular calcium concentration low.

ATP-driven transporter pumps hydrolyse adenosine 5'-triphosphate (ATP) and form adenosine 5'-diphosphate (ADP) and a free phosphate ion (Alberts *et al.*, 2008a). The ADP released is used to transport ions across the membrane against the electrochemical gradient. The sodium-potassium pump (discovered by Skou, 1957) is one such ATP-driven transport mechanism which functions as an antiporter. A high concentration of potassium ions and a low concentration of sodium ions inside a cell is maintained by the transfer of three sodium ions out of the cell for every two potassium ions transferred in. The sodium gradient maintained by the sodium-potassium pump then fuels the sodium-calcium exchanger described above. The calcium pumps in the plasma membrane and the membrane of the

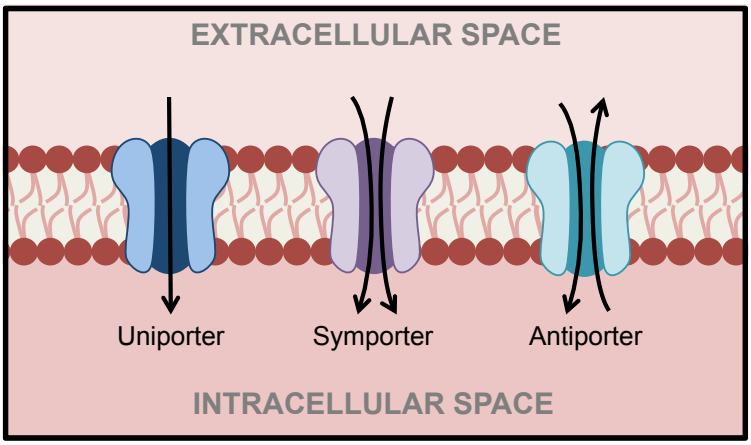

Figure 1.13: Types of transporter-mediated movement. Uniporters mediate the movement of a single type of ion across the membrane. Symporters involve the simultaneous transfer of two ions in the same direction across the membrane. Antiporters transfer a second ion in an opposite direction to the first. Both symporters and antiporters utilise the free energy released during the downhill transport of one ion across the membrane to power the uphill transport of another.

sarcoplasmic reticulum also use ATP to remove excess calcium from the cell cytoplasm and maintain the quiescent environment (Tribe *et al.*, 2000).

Ionic pumps typically transfer ions across a membrane slower than an ion channel since the ions have to be transported against their electrochemical gradient (Gadsby, 2009). The rate of transfer is determined by the gating kinetics; an ion channel has only one gate, whereas a pump can be considered to have at least two gates which must never be open simultaneously. The gating reactions have a frequency of around 100 Hz (calculated by the tracking of rapid current bursts across a membrane) meaning that an ionic pump can be at least twice as slow as an ion channel (Gadsby, 2009). The reduced rate of transfer in an ionic pump means that a pump can transfer between 10^2 and 10^3 across a membrane per second, whereas an ion channel can transfer 10^7 ions per second (van Eldik & Hubbard, 2009). The ionic pumps are important for maintaining quiescence in the uterus and keeping Ca^{2+} concentrations low, whereas ions which promote cellular excitation are transferred into the cell through ion channels; the slow transfer rates of pumps relative to channels means that any damping of the excitation is minimal.

1.7.2 The membrane potential

The maintenance of a constant cell volume is of prominent importance to the survival of any biological cell. This is achieved through regulation of the intracellular composition of the cell using the ion transport processes described above. One consequence of the constant cell volume is the potential difference across the cell membrane, termed the membrane potential, which is defined as the difference in electrical potential between the intra- and extracellular regions. The Nernst equation gives the potential difference across a selectively permeable membrane when the voltage gradient balances the concentration gradient for a given ion.

1.7.2.1 Derivation of the Nernst equation

The ionic current through a membrane channel protein is driven by the electrochemical gradient for that ion (Hille, 1992). The electrochemical gradient is a combination of the voltage gradient and the concentration gradient of the ion across the membrane. When the voltage gradient balances the concentration gradient, the electrochemical gradient for that ion is zero and there is no net flow of the ions through the channel. The voltage gradient at which this equilibrium is reached is the equilibrium potential for the ion.

To derive the Nernst equation, we follow the derivation given by van den Berg (2011). Consider N particles which can assume one of a set of discrete energy levels $\epsilon_0, \epsilon_1, \epsilon_2, \ldots$ The Boltzmann energy distribution states that the probability of a particular energy state j is proportional to the energy of that state ϵ_j:

$$p_j = \frac{n_j}{N} = \frac{\exp\{-\epsilon_j / k_B T\}}{\sum_\ell \exp\{-\epsilon_\ell / k_B T\}}, \tag{1.2}$$

where n_j is the number of particles assigned energy state ϵ_j, k_B is the Boltzmann constant, T is the temperature (in Kelvin), and $\sum_\ell$ represents the sum over all ℓ energy states.

We now consider the N particles to be distributed between a biological cell of volume V_i and a finite extracellular space of volume V_e. Using the Boltzmann energy distribution, for each one of the N particles we calculate the probability of that particle being found inside the cell:

$$\mathbb{P}[\text{particle in cell}] = \frac{\sum_{V_i} \exp\{-\epsilon_j/k_BT\}}{\sum_{V_i+V_e} \exp\{-\epsilon_j/k_BT\}}, \tag{1.3}$$

where $\sum_{V_i}$ is the sum over all states where the particle is inside the cell and $\sum_{V_i+V_e}$ is the sum over all states where the particle is either inside or outside of the cell. The concentration of particles inside the cell is $C_i = N\mathbb{P}[\text{particle in cell}]/V_i$, and the concentration of particles outside the cell is $C_e = N\mathbb{P}[\text{particle outside cell}]/V_e$. Therefore,

$$\frac{\mathbb{P}[\text{particle in cell}]}{\mathbb{P}[\text{particle outside cell}]} = \frac{C_iV_i}{C_eV_e}. \tag{1.4}$$

When the membrane is permeable to the particles and the particles carry no charge, at equilibrium the particle concentrations inside and outside of the cell will be equal. Combining Equations (1.3) and (1.4) gives:

$$\frac{V_i}{V_e} = \frac{\sum_{V_i} \exp\{-\epsilon_j/k_BT\}}{\sum_{V_e} \exp\{-\epsilon_j/k_BT\}}, \tag{1.5}$$

where $\sum_{V_e}$ is the sum over all states where the particle is outside the cell. If the particles are charged, $\Delta\epsilon$ represents the work done on the particle to transport it inside the cell. Then,

$$\begin{aligned} \frac{C_iV_i}{C_eV_e} &= \frac{\mathbb{P}[\text{particle in cell}]}{\mathbb{P}[\text{particle outside cell}]}, \\ &= \frac{\sum_{V_i} \exp\{-(\epsilon_j+\Delta\epsilon)/k_BT\}}{\sum_{V_e} \exp\{-\epsilon_j/k_BT\}}, \\ &= e^{-\Delta\epsilon/k_BT} \frac{\sum_{V_i} \exp\{-\epsilon_j/k_BT\}}{\sum_{V_e} \exp\{-\epsilon_j/k_BT\}}. \end{aligned} \tag{1.6}$$

Substituting Equation (1.5) gives:

$$\frac{C_i}{C_e} = e^{-\Delta\epsilon/k_BT} \quad \text{or} \quad \Delta\epsilon = k_BT \ln \frac{C_e}{C_i}. \tag{1.7}$$

The charge of each particle is zq where z is the valency of the particle and q is the charge carried by a single proton. The work done on a particle entering the cell is the charge multiplied by the potential difference across the membrane (V_m). The work done can therefore be written $\Delta\epsilon = V_m zq$ and so we obtain the Nernst equation:

$$V_m = \frac{k_BT}{zq} \ln \frac{C_e}{C_i}. \tag{1.8}$$

Consider a membrane permeable to ion X only. At equilibrium, there will be no net flow of X ions through the membrane, and the membrane potential will be equal to the Nernst potential. The ions of interest in the myometrial cell are potassium, calcium, sodium, and chloride. We can write the equations for the Nernst potentials for these ions:

$$\begin{aligned}
V_{\mathrm{K}} &= \frac{k_BT}{q} \ln \left(\frac{[\mathrm{K}^+]_e}{[\mathrm{K}^+]_i} \right), \\
V_{\mathrm{Ca}} &= \frac{k_BT}{2q} \ln \left(\frac{[\mathrm{Ca}^{2+}]_e}{[\mathrm{Ca}^{2+}]_i} \right), \\
V_{\mathrm{Na}} &= \frac{k_BT}{q} \ln \left(\frac{[\mathrm{Na}^+]_e}{[\mathrm{Na}^+]_i} \right), \\
V_{\mathrm{Cl}} &= \frac{k_BT}{q} \ln \left(\frac{[\mathrm{Cl}^-]_i}{[\mathrm{Cl}^-]_e} \right).
\end{aligned} \tag{1.9}$$

In the Nernst equation for chloride ions, the logarithm is inverted to take into account the negative charge of the ion. In a typical mammalian cell at rest, approximate Nernst potential values are $E_{\mathrm{K}} = -45\,\mathrm{mV}$, $E_{\mathrm{Ca}} = 123\,\mathrm{mV}$, $E_{\mathrm{Na}} = 36\,\mathrm{mV}$, and $E_{\mathrm{Cl}} = -32\,\mathrm{mV}$ (calculated from ionic concentrations given by Alberts *et al.* (2008a)).

The Nernst equation may also be written as follows:

$$V_m = \frac{RT}{zF} \ln \left(\frac{[\mathrm{X}]_e}{[\mathrm{X}]_i} \right), \tag{1.10}$$

where $F = qN_A$ is Faraday's constant and the relationship $k_B = R/N_A$ has been used, where R is the universal gas constant and N_A is Avogadro's number. This version of the Nernst equation will be used in the derivation of the Goldman-Hodgkin-Katz equation below.

1.7.2.2 Goldman-Hodgkin-Katz Equation

Equilibrium potentials generated from the Nernst equation give the membrane potential of a cell that is permeable to only one ion. However, in myometrial smooth muscle cells the contributions of potassium, calcium, sodium, and chloride ions need to be considered. The Goldman-Hodgkin-Katz (GHK) equation calculates the equilibrium potential across the cell membrane taking into account all the ions that the membrane is permeable to. The derivation of the GHK equation given below is adapted from Hille (1992) and Keener & Sneyd (2004).

We assume that the membrane is homogeneous and that the electrical field is constant so that it varies linearly with distance across the membrane. It is assumed that the ions do not need to diffuse to the permeating surface, and that the permeant ions do not interact with each other. The movement of ions is affected by their electrochemical gradient, that is the concentration gradient of the ions and the electrical field. The flow due to the electrical field can be determined by Planck's equation:

$$\mathbf{J} = -u \frac{z}{|z|} c \nabla \phi, \tag{1.11}$$

where u is the mobility of the ion (the velocity of the ion under a constant unit electrical

field), z is the valence of the ion, c is the concentration of the ion, and ϕ is the electrical potential so that $-\nabla\phi$ is the electrical field.

The Nernst-Einstein relationship between u and Fick's diffusion constant, D, is as follows:

$$D = \frac{uRT}{|z|F}, \tag{1.12}$$

where R is the universal gas constant, T is temperature (K) as before, and F is Faraday's constant. Combining the effect of concentration gradients ($\boldsymbol{J} = -D\nabla c$) and electrical gradients (Equation (1.11)), we arrive at the Nernst-Planck equation:

$$\boldsymbol{J} = -D\left(\nabla c + \frac{zF}{RT}c\nabla\phi\right). \tag{1.13}$$

If the membrane potential is not equal to the reversal potential of ion X, then a current I_{X} will flow. The current is related to the flux as follows:

$$I_X = z_{\mathrm{X}}FJ_{\mathrm{X}}. \tag{1.14}$$

Combining Equations (1.13) and (1.14) in one dimension gives:

$$I_{\mathrm{X}} = -z_{\mathrm{X}}FD\left(\frac{dc_{\mathrm{X}}}{ds} + \frac{z_{\mathrm{X}}Fc_{\mathrm{X}}}{RT}\frac{d\phi}{ds}\right), \tag{1.15}$$

where s is the distance across the membrane. Integrating the concentration c_{X} across a membrane of thickness L, and doing some rearranging, gives the Goldman-Hodgkin-Katz current equation for ion X:

$$I_{\mathrm{X}} = P_{\mathrm{X}}\,\frac{z_{\mathrm{X}}^2F^2V_{\mathrm{m}}}{RT}\,\frac{[\mathrm{X}]_i - [\mathrm{X}]_e\exp(-z_{\mathrm{X}}FV_{\mathrm{m}}/RT)}{1-\exp(-zFV_{\mathrm{m}}/RT)}, \tag{1.16}$$

where $P_{\mathrm{X}} = D/L$ is the permeability of the membrane to ion X. If the flow of ions is zero, then Equation (1.16) becomes Equation (1.10) once more (the Nernst equation).

We finally consider all ions that the membrane is permeable to; the flow of each of these ions is described by its own current-voltage relationship. The total ionic current is then equal to the sum of the currents of the individual ions. At equilibrium, there will be no net current flow through the membrane. Using Kirchhoff's current law, the total current flow will then be zero:

$$I = 0 = I_{\mathrm{Na}} + I_{\mathrm{K}} + I_{\mathrm{Cl}} + I_{\mathrm{Ca}}. \tag{1.17}$$

Solving for V, and substituting in our ions of interest, we then obtain:

$$V = -\frac{RT}{F} \ln \left(\frac{P_{\mathrm{Na}} \left[\mathrm{Na}^+\right]_i + P_{\mathrm{K}} \left[\mathrm{K}^+\right]_i + P_{\mathrm{Cl}} \left[\mathrm{Cl}^-\right]_e + 4P_{\mathrm{Ca}} \left[\mathrm{Ca}^{2+}\right]_i}{P_{\mathrm{Na}} \left[\mathrm{Na}^+\right]_e + P_{\mathrm{K}} \left[\mathrm{K}^+\right]_e + P_{\mathrm{Cl}} \left[\mathrm{Cl}^-\right]_i + 4P_{\mathrm{Ca}} \left[\mathrm{Ca}^{2+}\right]_e} \right), \tag{1.18}$$

which is the Goldman-Hodgkin-Katz voltage equation (Goldman, 1943; Hodgkin & Katz, 1949), modified to incorporate divalent ions such as calcium (Chang, 1983).

The GHK equation gives the membrane potential at which the net flow of ions is zero. This potential is called the resting membrane potential (RMP) and is the state of an excitable cell in the absence of excitation, or the membrane potential of a non-excitable cell. A human myometrial cell typically has an RMP ranging between -45 and $-80\,\mathrm{mV}$, determined by the stage of pregnancy (Kumar & Barnes, 1961; Pressman *et al.*, 1988; Inoue *et al.*, 1990). If the membrane potential becomes more negative than the RMP it is said to be hyperpolarised (more polarised); if the membrane potential becomes less negative than the RMP then the cell is depolarised (less polarised).

1.7.3 Action potentials

Smooth muscle cells are excitable cells, that is if a sufficiently large current is applied to a cell, its membrane potential will go through a large excursion before returning to rest. The excursion is called an action potential. A smooth muscle action potential follows a characteristic shape (Figure 1.14): the cell is initially at rest and the net flow of

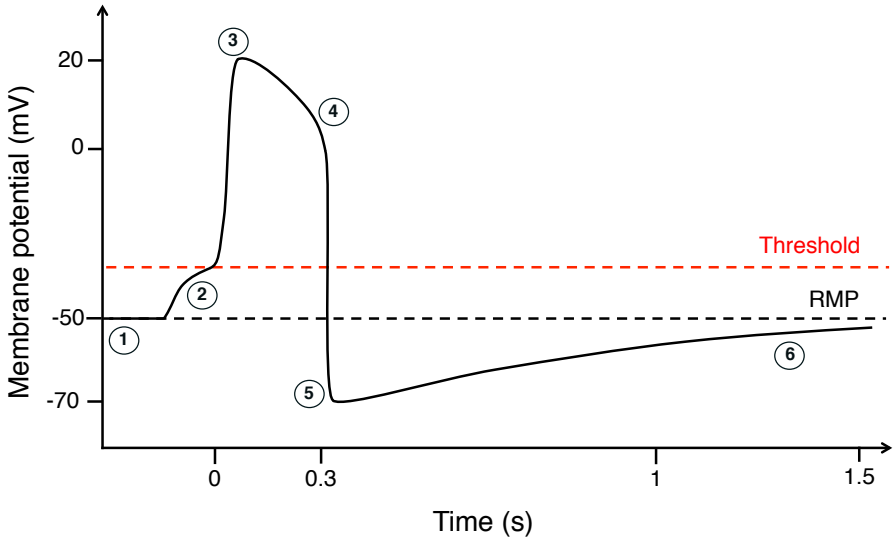

Figure 1.14: Schematic of the changes in the membrane potential of an excitable cell during an action potential. ① the cell is initially at rest; ② a sufficiently large current stimulus depolarises the membrane to its threshold potential; ③ the membrane undergoes a large depolarisation and is considered to be 'excited'; ④ the membrane potential remains in an excited state for 0.3 seconds (for a typical muscle action potential); ⑤ the membrane rapidly repolarises, undershooting the rest state: it is not able to be re-excited at this stage; ⑥ the membrane slowly returns to rest: this repolarisation may take up to 10 seconds in ureter smooth muscle (Burdyga & Wray, 2005).

ions across its membrane is zero; a current stimulus depolarises the cell membrane to its threshold potential; in response to the stimulus, the membrane potential has a large increase and the cell is considered to be 'excited'; after a period of excitation, the membrane repolarises rapidly and undershoots the rest state; the cell is now in a 'refractory' state and the threshold for re-excitation is very high; the membrane finally returns slowly to rest at which point it is able to become excited once again. An excitable cell can either respond in full to a stimulus or not at all meaning that any transmitted signal will also exhibit 'all-or-nothing' behaviour. Thus a signal can be reliably transmitted with minimal damping.

The first quantitative model of membrane dynamics during an action potential was derived by Hodgkin & Huxley (1952a,b,c,d) using experiments conducted on the squid giant axon. They interpreted their experimental results in terms of sodium and potassium channels.

An influx of sodium was found to underlie the rapid depolarisation, and the rapid repolarisation was determined to correlate with an efflux of potassium. Sodium was widely believed to be the ion with the largest contribution to the action potential until Fatt & Katz (1953) observed action potentials without sodium ions in crab leg muscle fibres. Fatt & Ginsborg (1958) subsequently identified an inflow of calcium ions coinciding with the action potential upstroke in muscle cells. The Nernst potential for calcium is more positive than the Nernst potential for sodium ions (Section 1.7.2.1), which explains the positive potential of the depolarising spike seen in muscle cells.

The gating kinetics of the calcium and potassium ion channels generates the characteristic shape of the smooth muscle action potential. The applied stimulus depolarises the membrane to the potential at which voltage-dependent calcium channels will rapidly open (Figure 1.15b). Calcium ions then enter the cell, down their concentration gradient, which further depolarises the membrane. The increase in intracellular calcium concentration triggers the pathway to contract the muscle cell. When the membrane is sufficiently depolarised, the potential attains a value at which voltage-dependent potassium channels open and the voltage-dependent calcium channels close (Figure 1.15c). The activation of the potassium channels, and the closure of the calcium channels are slow processes, which account for the 'lag' at point ④ in Figure 1.14. Once the potassium channels are open, and the calcium channels are closed, the membrane rapidly repolarises as potassium ions leave the cell. The potassium channels are slow to close (Figure 1.15d). Therefore once the RMP is reached, the membrane potential continues to become more negative until the potassium channels close fully so stopping the repolarisation. Until the membrane potential returns to rest, the threshold for exciting the cell is infinitely high and the cell is said to be in a refractory stage. This stage is followed by a relative phase in which the threshold is finite, but still elevated. The threshold slowly returns to its initial value as the RMP is restored.

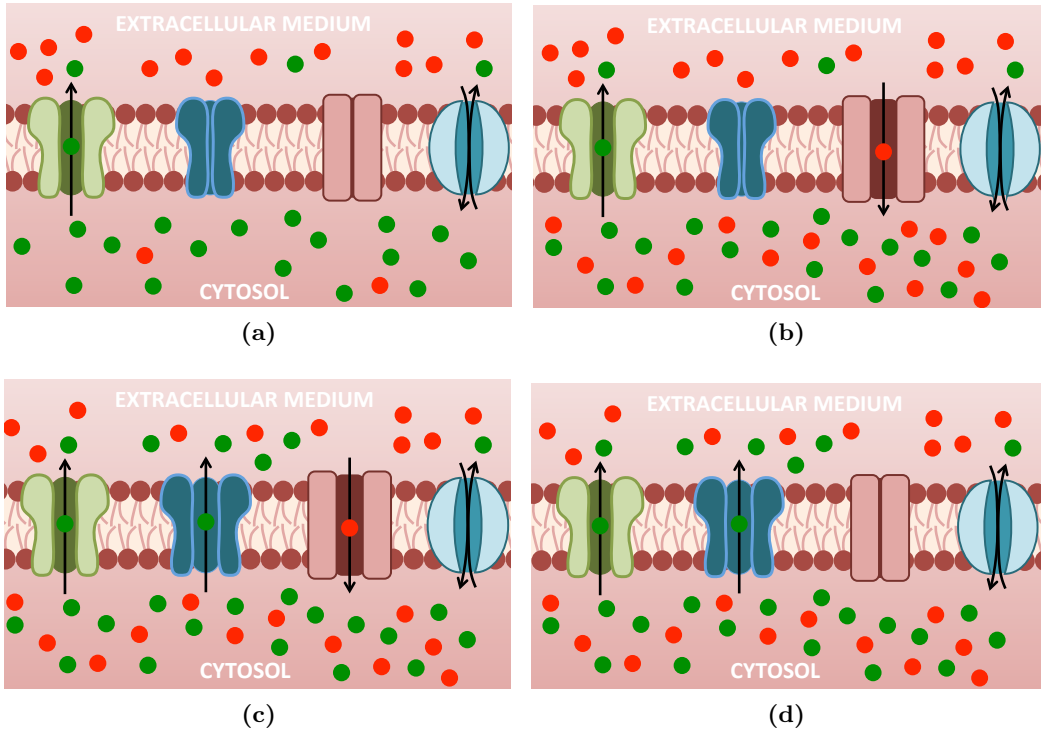

Figure 1.15: Sequence of events during an action potential. Potassium ions are indicated as green dots, calcium ions as red dots. A potassium leak channel is indicated in light green and a voltage-gated potassium channel in dark blue. A voltage-gated calcium channel is indicated in mauve. An active ion pump is indicated in light blue. (a) The rest state: the membrane is permeable for potassium and the membrane potential is close to the equilibrium potential for that ion. Active ion exchange maintains ionic gradients between the cytosol and the extracellular medium; (b) the membrane has undergone a slight depolarisation causing voltage-gated calcium channels to open, leading to further depolarisation of the membrane potential. The increase in calcium triggers the cell contraction pathway; (c) the elevated membrane potential operates voltage-gated potassium channels, leading to an increased permeability for that ion and a return to the resting membrane potential (repolarisation); (d) the voltage-gated calcium channels have closed.

1.8 Uterine contractility

Contraction of uterine smooth muscle is mediated by intracellular calcium concentration, as described by Webb (2003). Cytosolic calcium concentration is increased in one of two main ways (Figure 1.16). The first is an influx of calcium ions through voltage-operated calcium channels as described in Section 1.7.3. The second is through calcium release from the sarcoplasmic reticulum. Neurotransmitter and hormonal agonists bind to G-protein coupled receptors in the cell membrane (Smrcka *et al.*, 1991). This coupling increases phospholipase C (PLC) activity within the cell. The role of PLC is to cleave the membrane lipid phosphatidylinositol 4,5-bisphosphate (PIP_2) to produce two secondary messengers: diacylglycerol (DAG) and inositol 1,4,5-trisphosphate (IP_3) (Alberts *et al.*, 2008d; Berridge, 1993; Exton, 1996). The IP_3 messenger binds to receptors on the sarcoplasmic reticulum, stimulating the release of calcium from the internal stores. The DAG messenger activates protein kinase C (PKC) which phosphorylates calcium channels and cross-bridge cycling proteins.

The intracellular calcium ions trigger a smooth muscle contraction, as follows (Figure 1.16). The calcium ions bind the protein calmodulin which is abundant within the cell and activates protein kinase C (PKC) which phosphorylates calponin and removes the inhibiton of the myosin ATPase activity (Babu *et al.*, 1985; Li *et al.*, 2012). The calcium-calmodulin complex binds and activates the myosin light-chain kinase which phosphorylates the light-chain of myosin (Means *et al.*, 1991). Cross-bridge cycling of actin and the myosin light-chain occurs causing the smooth muscle cell to contract (Aguilar & Mitchell, 2010).

The smooth muscle cell relaxes through removal of the contractile trigger or by direct inhibition of the contractile mechanism. Both pathways result in a decreased intracellular calcium concentration and increased myosin light-chain phosphatase activity (Morgan, 1990; Somlyo *et al.*, 1999). Calcium uptake into the sarcoplasmic reticulum is dependent

on ATP hydrolysis (Carsten, 1969). The calcium-magnesium-ATPase binds two calcium ions and transfers then to the luminal side of the sarcoplasmic reticulum (Webb, 2003). Magnesium, which has an intracellular concentration of 0.6 mM, binds to the catalytic site of the ATPase which releases a phosphate ion and the ADP required for the enzyme activity (Zhang *et al.*, 1992). The plasma membrane also contains calcium-magnesium-ATPases which act to reduce the intracellular concentration of calcium. In addition, the presence of sodium-calcium exchangers in the membrane keep the concentration of intracellular calcium low at around 10 nM and maintain relaxation (Matthew *et al.*, 2004).

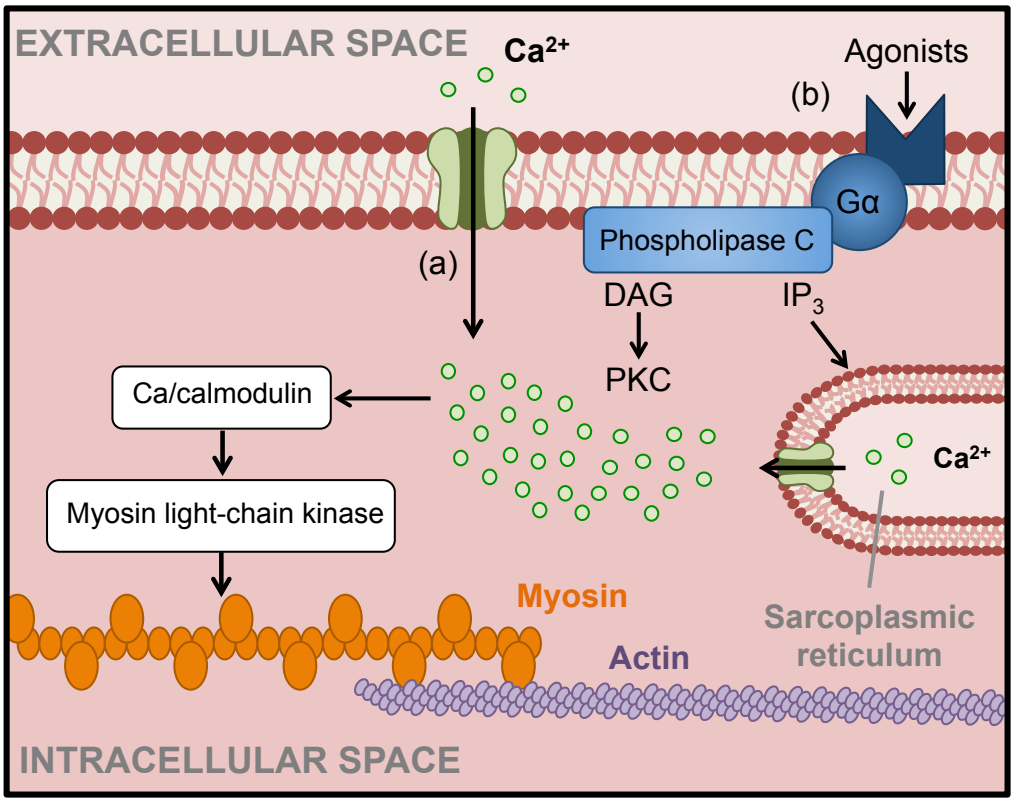

Figure 1.16: Mechanisms of smooth muscle contraction. The intracellular calcium binds calmodulin, which binds and activates the myosin light-chain kinase. The light-chain of myosin is phosphorylated resulting in cross-bridge cycling of actin and myosin which contracts the smooth muscle cell. Calcium ions enter the cell through two pathways. (a) Calcium enters through voltage-gated calcium channels; (b) Agonists bind to G-protein coupled receptors in the cell membrane, increasing the PLC activity within the cell. The role of PLC is to cleave PIP_2 to produce DAG and IP_3. The IP_3 binds to the SR, stimulating calcium release. The DAG messenger activates PLC which phosphorylates calcium channels and cross-bridge cycling proteins.

1.9 Control of uterine contractility

The contractility of myometrial smooth muscle is regulated by myogenic, neurogenic, and hormonal mechanisms (Figure 1.17). These mechanisms regulate both uterine conductance, that is the ability of the tissue to propagate electrical signals through gap junctions, and the electrical activity of the myometrium (Figure 1.18). Gap junction structure is primarily under hormonal control. Estrogen, oxytocin, and prostaglandins increase the density and permeability of gap junctions; progesterone and relaxin decrease density and permeability. An increase in gap junction expression increases the conductance of the myometrial tissue.

An action potential in the myometrium can be triggered by a depolarisation of the membrane of the smooth muscle cells (Figure 1.18). This depolarisation may be triggered either through receptor-operated channels (ROCs) which are controlled by neurogenic and hor-

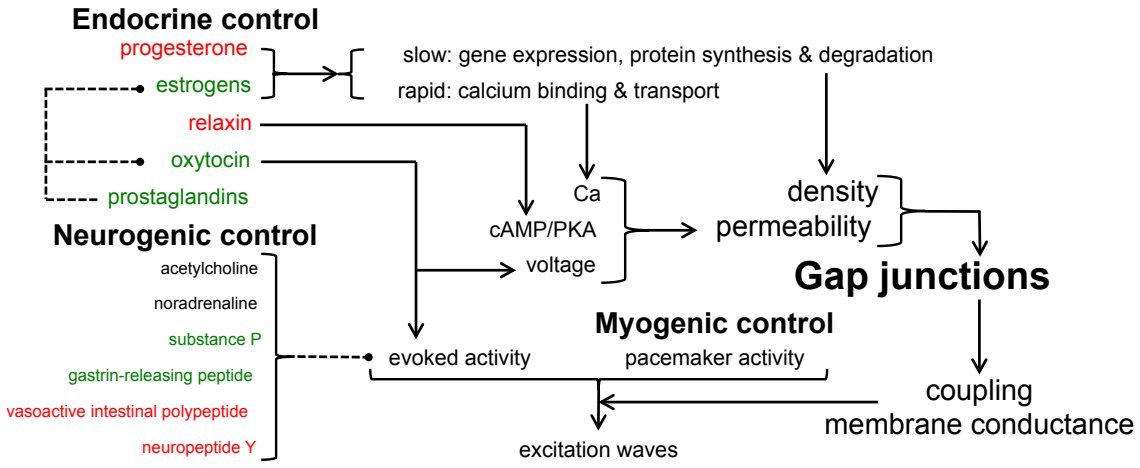

Figure 1.17: Mechanisms controlling uterine contractility. Gap junctions are regulated through endocrine mechanisms. Uterine activity is modulated through endocrine, neurogenic, and myogenic mechanisms. Modulators which are up-regulated for labour are shown in green; modulators which are down-regulated for labour are shown in red. The neurotransmitter noradrenaline is inhibitory to the longitudinal muscle layer in the rat throughout pregnancy; in contrast, it excites the circular layer in mid-pregnancy and inhibits contractions at term. The neurotransmitter acetylcholine has an excitatory effect on the myometrium throughout pregnancy. An increase in the number of gap junctions increases tissue conductance which in turn regulates the contractility of the uterus.

monal mechanisms, or by a pacemaker cell which is myogenic, that is an intrinsic property of the cell (Berridge, 2014). If the membrane depolarises sufficiently, voltage-gated calcium channels open, depolarising the membrane further.

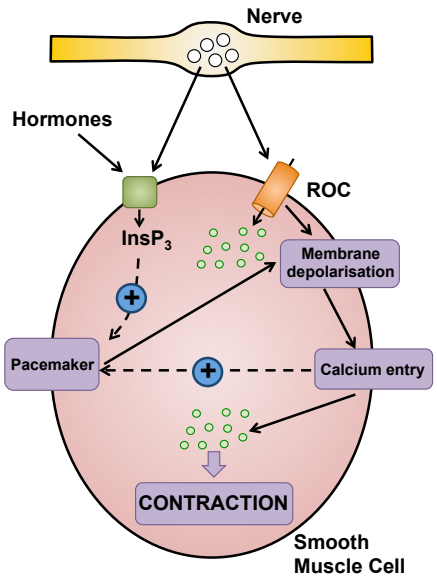

Figure 1.18: Mechanism for generating the Ca^{2+} transients that trigger contractions. The contractility is regulated by myogenic, neurogenic, and hormonal mechanisms. Neurotransmitters and hormones act as stimuli for inositol 1,4,5-trisphosphate (IP_3). An increase in IP_3 expression is thought to positively affect the myogenic properties of a pacemaker cell. Neurotransmitters can also affect the receptor-operated channels (ROCs). Either ROCs or a pacemaker can trigger membrane depolarisation. The depolarised membrane opens voltage-gated calcium channels allowing an influx of Ca^{2+} ions which cause the cell to contract. The increase in intra-cellular calcium may also provide positive feedback to the pacemaker. Adapted from Berridge (2014).

1.9.1 Hormonal control

Myometrial contractility is dominantly controlled through mechanisms of the hormones progesterone, estrogen, prostaglandins, oxytocin, and relaxin (Marshall, 1962, 1981; Thorburn & Challis, 1979). These hormones modulate the myogenic properties of the myometrium and neurogenic mechanisms. The rate of synthesis of steroid hormones changes prior to both normal and preterm labour in almost all species of animals. Csapo (1956, 1975) proposed two, related, theories in which pregnancy is maintained through a balance

of stimulants and suppressors. The 'progesterone block theory' (Csapo, 1956) describes pregnancy as a balance between progesterone acting as a relaxant, and estrogen acting as a stimulant. Csapo proposed that labour is initiated with the balance was shifted in favour of estrogen. The 'seesaw theory' (Csapo, 1975) developed this idea further. Pregnancy was now considered to be a balance between the relaxant progesterone and the stimulants prostaglandins, oxytocin, estrogen, and myometrial stretch. Csapo now proposed that labour was initiated by a functional withdrawal of progesterone.

Common to both theories is that the decrease of progesterone at term causes a regulatory imbalance that allows the stimulants to be the dominant force. It is now well-established that in most mammals, a decrease in progesterone levels occurs immediately prior to labour which causes the myometrium to change from being inactive to active muscle (Fuchs, 1978; Keelan *et al.*, 1997; Zakar & Hertelendy, 2007). Humans, guinea pigs, and higher primates are unusual in that the progesterone withdrawal has never been observed *in vivo*; progesterone levels remain high until after the delivery of the fœtus (Thorburn & Challis, 1979). However, it has been demonstrated that an artificially induced progesterone withdrawal will still induce labour in humans. It has been proposed that humans exhibit a 'functional' progesterone withdrawal in which the action of progesterone is inhibited at term rather than a change in synthesis of the hormone (Casey & MacDonald, 1997; Karalis *et al.*, 1996; Thomson *et al.*, 1999; Kalkhoven *et al.*, 1996; Mendelson & Condon, 2005).

Estrogen and progesterone have opposing effects on the myogenic properties of the muscle cells. Whereas progesterone has an inhibitory role, estrogen stimulates the smooth muscle cells and levels rise prior to labour in most species (Thorburn & Challis, 1979). Estrogen depolarises the smooth muscle cell membrane such that a smaller stimulus is needed to excite the cell. Action potentials are therefore readily initiated, and there is an increase in the number of impulses. Estrogen has also been shown to promote bursting action potentials displayed in the circular muscle of the late-pregnant rat (Kawarabayashi & Marshall,

1981); induce gap junction formation, so enhancing cell-to-cell coupling (Kuriyama & Suzuki, 1976; Garfield *et al.*, 1977; Sims *et al.*, 1982); stimulate prostaglandin production (Thorburn & Challis, 1979; Wilson Jr., 1983); and modulate the number of agonist receptors (such as oxytocin and relaxin receptors) in the myometrium (Kuriyama & Suzuki, 1976; Alexandrova & Soloff, 1980; Fuchs, 1983).

Prostaglandins $PGF_{2\alpha}$, PGE_1, and PGE_2 increase the activity of the smooth muscle network through an increase in contraction frequency (up to 4-fold in the rat) and up to a 7-fold increase in tonic tension (Reiner & Marshall, 1976; Chamley & Parkington, 1984). It has been demonstrated in the rat that the contractile change results from an inward sodium current where the calcium current remains unchanged (Reiner & Marshall, 1976; Grosset & Mironneau, 1977). The increase in tension is due to prostaglandin-stimulated calcium release from internal stores (Reiner & Marshall, 1976; Grosset & Mironneau, 1977; Anderson, 1978; Villar *et al.*, 1985). As labour approaches, the sensitivity of the myometrium to prostaglandins increases. In addition, prostaglandins modulate oxytocin release, inhibit progesterone synthesis, mediate cervical ripening, modify steroid receptors, and increase the expression of gap junctions between cells (Gillespie *et al.*, 1972; O'Grady *et al.*, 1972; Calder & Embrey, 1973; Garfield, 1980; Ulmsten *et al.*, 1982; Sanfillipo *et al.*, 1983).

Oxytocin can initiate contractions in quiescent uteri or increase the contractile frequency and force both *in vivo* and *in vitro* (Fuchs, 1978, 1983). This hormone increases the duration and frequency of spike burst discharges and increases electrical conduction. Oxytocin stimulates calcium entry into the cell (Mironneau, 1976) and raises intracellular calcium through release from intracellular stores (Sakai *et al.*, 1981; Batra, 1985). The uterine sensitivity to oxytocin increases as gestation progresses, coinciding with an increase in number of oxytocin binding sites, and reaching maximal levels just before term (Fuchs, 1978; Soloff *et al.*, 1979; Fuchs *et al.*, 1982; Chan, 1983; Sheldrick & Flint, 1985; Reimer *et al.*, 1986).

Relaxin plays a role in maintaining pregnancy and the control of cervical maturation (Porter *et al.*, 1979; Downing & Sherwood, 1985a,b,c). In the rat, levels of relaxin remain high throughout gestation yet decline just prior to labour (Sherwood *et al.*, 1980; Downing & Sherwood, 1985a). Relaxin has been shown to inhibit spontaneous activity in the rat myometrium; it is thought that relaxin is responsible for uterine quiescence despite progesterone withdrawal (Porter *et al.*, 1979; Downing & Sherwood, 1985b). There is no evidence to suggest that relaxin has an effect on the presence of myometrial gap junctions but it does have a negative effect on their permeability, decreasing the rate of diffusion across a gap junction 4-fold (Cole & Garfield, 1986). Relaxin has been shown to stimulate 3'-5'-cyclic adenosine monophosphate (cAMP) production in the rat uterus (Sanborn *et al.*, 1980). The production of cAMP stimulates protein kinase A (PKA) which inhibits cell contraction through an inhibition of myosin light-chain kinase (Gu *et al.*, 1992; Conti & Adelstein, 1981).

1.9.2 Neurogenic control

Neurogenic control of contractility involves neural stimulation and the effects of neurotransmitters on the muscle. In the uterus, neurogenic control does not regulate activity exclusively (Garfield *et al.*, 1988). Instead, it is superimposed on the myogenic mechanisms and influences the quality and quantity of contractility.

The uterus is supplied by postganglionic adrenergic and cholinergic fibres which form part of the autonomous nervous system (Owman *et al.*, 1967; Thorbert, 1978). Most adrenergic and cholinergic nerves have been shown to disappear at term in humans and other mammals in all sections of the uterus except for at the cervix and the tubal ends of the uterus (Marshall, 1981; Garfield, 1986). The adrenergic neurotransmitter noradrenaline has been shown to inhibit contractions in mid-gestation and at term in the longitudinal layer of rat tissue (Kawarabayashi & Osa, 1976; Chow & Marshall, 1981). In contrast, no-

radrenaline stimulates activity in mid-gestation and inhibits activity at term in the circular layer of rat tissue (Kawarabayashi & Osa, 1976; Osa & Watanabe, 1978; Chow & Marshall, 1981; Kishikawa, 1981). These results may suggest an association between the presence of adrenergic nerves and the initiation of labour (Thorbert, 1978; Marshall, 1981). However, noradrenaline has been shown to be present in the blood as a hormonal factor (Wuttke, 1987). As such, it may be the case that noradrenaline is delivered to the uterus without the need for afferent nerves. The cholinergic neurotransmitter acetylcholine promotes myometrial excitability throughout gestation (Marshall & Kroeger, 1973; Bengtsson *et al.*, 1984; Izumi, 1985). Thorbert (1978) proposed that the nerves that remain at term serve to initiate pacemaker activity at the utero-tubal junction.

Peptidergic nerves such as substance P (SP) and gastrin-releasing peptide (GRP) increase the frequency and amplitude of non-pregnant uterine contractions, whereas vasoactive intestinal polypeptide (VIP) inhibits both non-pregnant spontaneous and SP-stimulated contractions (Ottesen, 1981; Ottesen *et al.*, 1981, 1983; Stjernquist *et al.*, 1986). In the non-pregnant rat, neuropeptide Y has been shown to inhibit neurally-stimulated, but not spontaneous, contractions (Stjernquist *et al.*, 1983). In the human, VIP nerve fibres decrease during pregnancy, so reducing their contraction-inhibiting effects (Ottesen *et al.*, 1982).

1.9.3 Myogenic control

Myogenic activity occurs in the absence of neural or humoral influences *i.e.* activity generated autonomously within the muscle tissue itself. A membrane depolarisation is triggered by the spontaneous oscillation of the membrane potential of the pacemaker cells that are electrotonically coupled to the cell at hand (Berridge, 2014). This myogenic property of smooth muscle cells appears to be absent for most of pregnancy, with the uterus only developing pacemaker properties in the days leading up to labour. It has been hypothe-

sised that oscillating behaviour occurs in response to steroid changes and is responsible for synchronous myometrial contractility (Crane & Martin, 1992). Contrary to this hypothesis, the existence of pacemaker cells within the uterine smooth muscle network is much disputed in the literature (Duquette *et al.*, 2005; Wolfs & Rottinghuis, 1970; Kao, 1959; Marshall & Kroeger, 1973; Young, 2007). If pacemaker cells do exist, histological, cytochemical, and immunochemical studies have suggested that the cells must be anatomically similar to the remaining myocytes, and have no fixed location within the uterus (Wray *et al.*, 2001). It is therefore only possible to identify such cells in the uterus through spatio-temporal mapping and recognising cyclic patterns of electrical activity which are spread as action potentials through the myometrial system (Lodge & Sproat, 1981).

1.10 Mathematical modelling of the uterus

Mathematical models have been used extensively to describe uterine excitability at varying levels of detail. The simplest models consider each myometriocyte as a cellular automaton which has three distinct states with arbitrary time periods: active, refractory, and inactive (Markus & Hess, 1990; Gerhardt *et al.*, 1990a,b,c, 1991). With limited computational resources, simple models enable a large number of cells to be studied without any great detail about an individual cell. More complex models consider an excitation variable, a relaxation variable, and a variable describing calcium entry into the cell (Morris & Lecar, 1981). The most complex varieties model each individual ion channel in the cell membrane (Tong *et al.*, 2011; McCloskey *et al.*, 2014). In contrast to cellular automata, having a large amount of detail for each individual cell requires much greater computational power. Consequently, a more detailed model typically means that a much smaller number of cells in the network can be studied.

In this thesis, we use the FitzHugh-Nagumo (FHN) model which comprises an excitation variable and a relaxation variable (FitzHugh, 1960, 1961; Nagumo *et al.*, 1962). The

FHN model effectively describes the activity of an excitable element such as a myometrial smooth muscle cell with minimal state variables, which renders the model computationally efficient. Two-dimensional model networks of up to 625 cells used here were made feasible by this computational efficiency. The FHN model is now regarded as a qualitative simplification of the Hodgkin-Huxley (HH) mathematical model, to which we turn in the next section.

1.10.1 Hodgkin-Huxley model

Hodgkin & Huxley (1952a,b,c,d) developed the first biophysically detailed model of the propagation of an electrical signal using measurements of membrane conductance and cytoplasm conductivity taken from experiments on a squid giant axon. Ion channels had not been discovered at the time of Hodgkin and Huxley's investigation; the membrane ionic theory of excitation was developed as a consequence of their work. The HH model has since been used to model a wide range of excitable systems, including the myometrium (Ramón *et al.*, 1976; Tai *et al.*, 2005; Bursztyn *et al.*, 2007; Sun *et al.*, 2008; Barclay *et al.*, 2010).

In the squid giant axon, the ions of interest are sodium (Na^+) and potassium (K^+). The remaining currents are amalgamated into a 'leakage current.' The HH model has four state variables: v, which is the difference between the membrane potential V_m and the resting potential V_{eq}; m, which describes the sodium channel activation; n, which describes the potassium channel activation; and h, which describes the sodium channel inactivation.

The HH equations are as follows:

$$\begin{aligned} C_m \frac{dv}{dt} &= -\bar{g}_{\mathrm{K}} n^4 (v - v_{\mathrm{K}}) - \bar{g}_{\mathrm{Na}} m^3 h (v - v_{\mathrm{Na}}) - \bar{g}_{\mathrm{L}} (v - v_{\mathrm{L}}) + I_{app}, \\ \frac{dm}{dt} &= \alpha_m (1 - m) - \beta_m m, \\ \frac{dn}{dt} &= \alpha_n (1 - n) - \beta_n n, \\ \frac{dh}{dt} &= \alpha_h (1 - h) - \beta_h h, \end{aligned} \tag{1.19}$$

where C_m is membrane capacitance (in units of $\mu\mathrm{F/cm}^2$); $\bar{g}_{\mathrm{Na}}$, $\bar{g}_{\mathrm{K}}$, and $\bar{g}_{\mathrm{L}}$ are the maximal conductances of the sodium, potassium, and leakage channels, respectively (in units of $\mu\mathrm{S/cm}^2$); v_{Na}, v_{K}, and v_{L} are the equilibrium potentials of the corresponding channels (in units of mV); I_{app} is the applied current (in units of $\mu\mathrm{A/cm}^2$); and α_m, α_n, α_h, β_m, β_n, and β_h are functions in units of $(\mathrm{ms})^{-1}$ with equations as follows:

$$\begin{aligned} \alpha_m &= 0.1 \frac{25 - v}{\exp\left(\frac{25 - v}{10}\right) - 1}, \\ \beta_m &= 4 \exp\left(\frac{-v}{18}\right), \\ \alpha_h &= 0.07 \exp\left(\frac{-v}{20}\right), \\ \beta_h &= \frac{1}{\exp\left(\frac{30 - v}{10}\right) + 1}, \\ \alpha_n &= 0.01 \frac{10 - v}{\exp\left(\frac{10 - v}{10}\right) - 1}, \\ \beta_n &= 0.125 \exp\left(\frac{-v}{80}\right). \end{aligned} \tag{1.20}$$

When Hodgkin and Huxley proposed these equations, the powers of h, m, and n were chosen so as to allow for a good fit to the experimental data. The physiological relevance of the powers has since been confirmed; the sodium channel has three m (activation) gates and a single h (inactivation) gate, and the potassium channel has four n (activation) gates. The variables m and v change rapidly as a result of the rapid activation of the sodium channel; n and h change relatively slowly due to the slow inactivation of sodium, and slow

activation of potassium. The kinetics of the variables give rise to the fast activation and slow repolarisation of the cell which is observed *in vivo*.

1.10.2 FitzHugh-Nagumo model

In this thesis, we use the FHN differential equations to model the excitable cells within the myometrium. The FHN model is a projection of the HH equations onto two dimensions, capturing the key qualitative dynamics of the model. FitzHugh (1960, 1961) gave a qualitative description of the HH model to better understand its behaviour. He identified that some of the model variables had fast kinetics (*i.e.* m and v which describe the fast sodium channel activation and the rapid change in membrane potential, respectively) whereas others had slow kinetics (*i.e.* n and h which describe the slow inactivation of the sodium channels and the slow activation of the potassium channels, respectively). In the early stages of the action potential, the slow-gated variables remain constant whereas the fast-gated variables change rapidly. Thus the full phase space can be studied at the start of an action potential by fixing the slow-gated variables and just studying the fast-gated variables. In a similar manner, different cross-sections can be taken of the four-dimensional phase plane to project the dynamics onto two-dimensions. FitzHugh considered a cross-section with one fast and one slow variable. The fast variable is extracted by assuming that the activation of the sodium channel acts on a faster time scale than the membrane potential; that is, that m is an instantaneous function of v. FitzHugh next observed that the value of $h + n$ remained approximately constant, allowing h to be eliminated from the equations. The HH model now contained a fast variable v and a slow variable n.

The analysis of the HH model and the derivation of the set of equations describing the fast-slow phase plane by FitzHugh (1961) was originally labelled the 'Bonhoeffer-van der Pol' (BVP) oscillator as a particular set of parameters rendered the equations identical to the van der Pol oscillator. The equivalent electrical circuit for this model was suggested

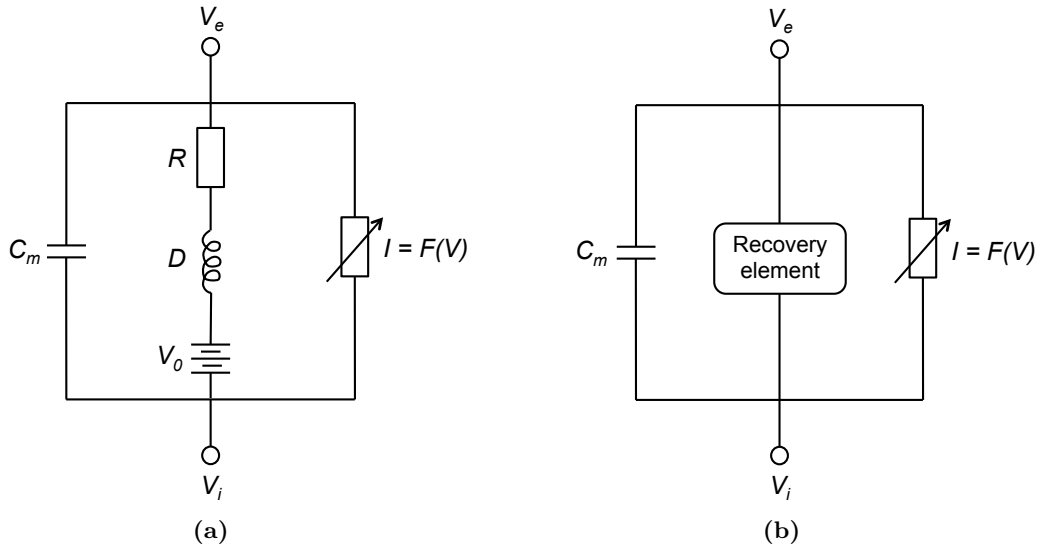

Figure 1.19: Circuit diagrams for the FitzHugh-Nagumo model. Adapted from Keener & Sneyd (2004). (a) A capacitor represents the membrane capacitance (C_m), a variable resistor represents the fast current (I) because of its dependence on membrane potential, and the resistor (R), inductor (D) and battery (V_0) in series represent the recovery current. The voltages inside and outside the cell are labelled V_i and V_e, respectively. (b) The circuit is generalised by highlighting the 'recovery element' responsible for cell recovery.

by Nagumo *et al.* (1962) who constructed the circuit with a tunnel diode as the non-linear element. The circuit diagram for the FHN model is shown in Figure 1.19a, with a more general form, indicating the excitable element, in Figure 1.19b. The membrane is modified as a capacitor (C_m) since it separates intra- and extracellular charges, a variable resistor represents the fast current (I) because it is dependent on the membrane potential, and the resistor (R), inductor (D), and battery (V_0) in series represent the recovery current.

In order to derive the FHN equations, we follow the derivation given by Keener & Sneyd (2004). Using the notation from Figure 1.19a and Kirchhoff's laws, we obtain:

$$C_m \frac{dV}{d\tau} + F(V) + i = -I_0, \tag{1.21a}$$

$$D \frac{di}{d\tau} + Ri = V - V_0, \tag{1.21b}$$

where I_0 is the applied external current, i is the current through the resistor-inductor,

$V = V_i - V_e$ is the membrane potential, V_0 is the potential gain across the battery, and τ is dimensional time. The function $F(V)$ is typically modelled as a cubic with three solutions: the smallest $V = 0$ and the largest $V = V_1$ are stable solutions of $dV/d\tau = -F(V)$ whereas the middle solution is unstable. Defining R_1 as the passive resistance of the nonlinear element, $R_1 = 1/F'(0)$, we can define the dimensionless variables $v = V/V_1$, $w = R_1 i/V_1$, $f(v) = -R_1 F(V_1 v)/V_1$, and $t = R_1\tau/D$. Equations (1.21a) and (1.21b) then become

$$\frac{dv}{dt} = \frac{1}{\varepsilon}(f(v) - w - w_0), \tag{1.22a}$$

$$\frac{dw}{dt} = v - \gamma w - v_0, \tag{1.22b}$$

where $\varepsilon = R_1^2 C_m/D$, $w_0 = R_1 I_0/V_1$, $v_0 = V_0/V_1$, and $\gamma = R/R_1$. For the FitzHugh-Nagumo model, we take the cubic function $f(v)$ to be

$$f(v) = Bv(v - \alpha)(1 - v), \tag{1.23}$$

where B and α are constants.

Whereas the HH model has four state variables, the FHN model has two; one fast variable (v) representing rapid excitation associated with fast-opening ion channels and one slow variable (w) representing the slower cell relaxation due to slow-opening channels. The fast variable has a cubic nullcline whereas the slow variable has a linear nullcline; the general FHN phase-plane diagram is given in Figure 1.20. The intersection of the two nullclines indicates the point at which the cell is at rest. This point is a fixed point of Equations (1.22). For most sets of parameter values, this fixed point is stable. Therefore, if all cells are considered to be at rest initially, an input of current is needed to stimulate the network. This input I is added to dv/dt in Equation (1.22a).

By examining the values of dv/dt and dw/dt at paired values (v, w) in Figure 1.21a, we can build up a portrait of the trajectory of the cell's membrane potential (Figure 1.21b).

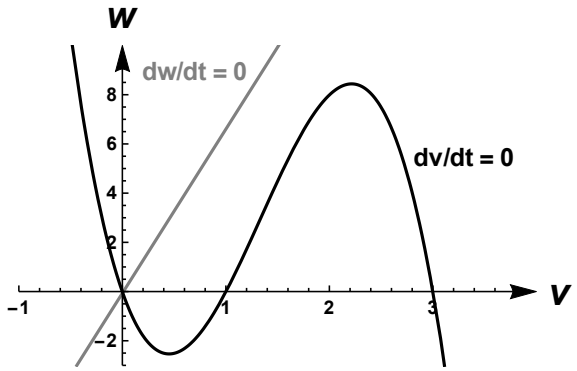

Figure 1.20: The general form of the FitzHugh-Nagumo phase-plane. The black line corresponds to the cell excitation null isocline (nullcline); the grey line corresponds to the cell relaxation nullcline. The intersection of the two nullclines represents a cell at rest. The dimensionless parameter values dictate the stability of the intersection point. Here, parameter values are chosen to create a stable fixed point at the intersection of the nullclines. A cell with these values requires an input of current in order to become excited.

A cell that is sufficiently perturbed from its rest state so as to cross the middle branch of the cubic nullcline moves rapidly towards the furthest right branch of the cubic nullcline and is considered to have been excited. The system then remains in an excited state, but is slowly pulled up towards the linear nullcline. At the local maximum of the cubic nullcline, the system undergoes a rapid relaxation and the cell moves over to the left-most branch of the cubic nullcline. The system then remains in a refractory period and no further activation can take place before returning to the rest state – the stable fixed point of the system.

If parameters are chosen such that the linear nullcline passes through the local minimum of the cubic nullcline (Figure 1.21c), the fixed point is unstable. Cells with these parameters are able to continually re-excite themselves (Figure 1.21d) and are considered to be 'pacemakers' (see Section 1.9.3). The system does then not need any additional current input, and, under certain conditions, is able to drive the excitation of the whole network. These conditions are discussed in Section 2.4.8.

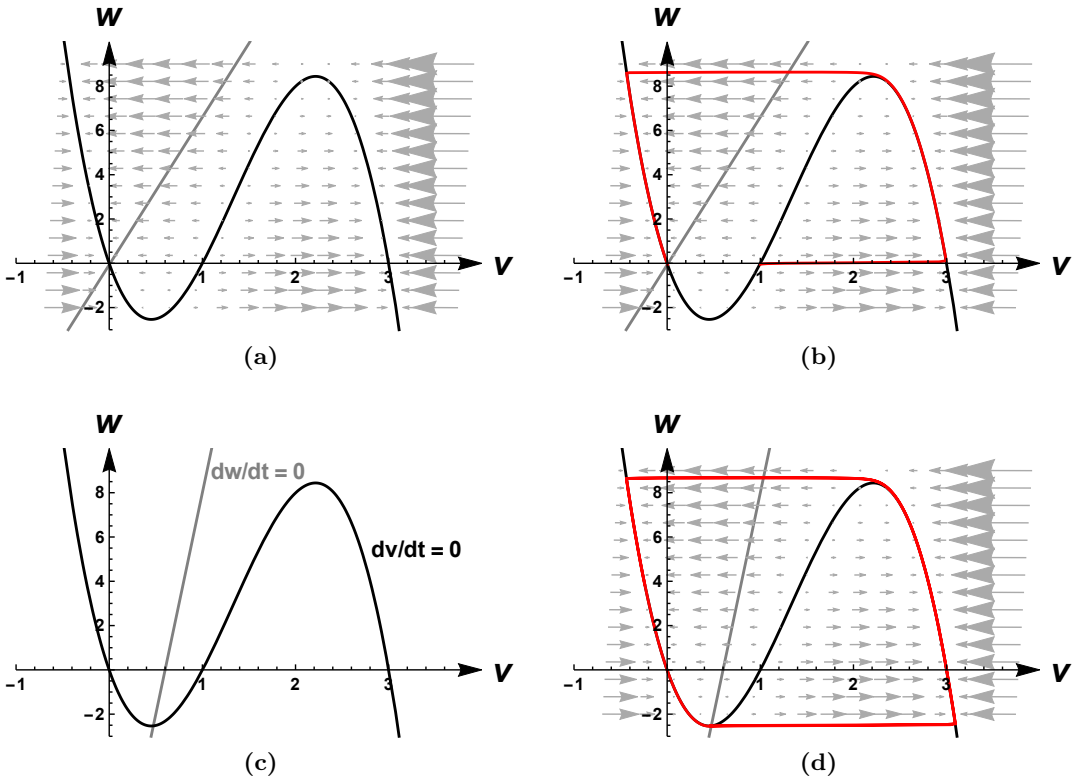

Figure 1.21: Phase-portrait diagram of an excited cell in the FHN model — dimensionless units. (a) Vector field showing arrows in the direction of $(dv/dt,\ dw/dt)$ at each pair of coordinates $(v,\ w)$; (b) the trajectory of an excited cell is shown in red and overlaid on the vector field and phase plane; (c) An unstable fixed point is generated at the intersection of the two nullclines when the linear nullcline intersects the cubic nullcline at its local minimum; (d) the trajectory of a pacemaker cell is shown in red and overlaid on the vector field and phase plane. A pacemaker cell is able to continually re-excite itself, and requires no addition current input.

1.11 Thesis outline and aims

A major contributor to preterm labour is dysfunction of the myometrium, the smooth muscle layer of the uterine wall. Globally, 15 million babies are born preterm each year and at least 1 million of these babies will not survive as a consequence of their prematurity. Effective management of preterm labour remains a huge challenge because of limitations in our knowledge of the mechanisms that govern uterine excitability and contraction. Throughout most of gestation, the uterus maintains a quiescent environment under the influence of the hormones progesterone and relaxin. The uterus undergoes a period of activation towards the end of pregnancy to provide the powerful contractions needed to deliver the baby. Gap junctions, which connect neighbouring myocytes, are one of the most important proteins involved in this activation process. While the uterus is quiescent, gap junction density is almost negligible and activity is not propagated through the network. By the end of pregnancy, gap junction density is high and the myometrium is well-connected. There is a paucity of quantitative data on the impact of gap junction regulation on the propagation of electrical excitation.

The overall aim of this thesis is to understand how intercellular communications mediated by gap junctions shape the dynamics of the myometrial smooth muscle network in its transition to an excitable state. The specific objectives are:

- to construct a mathematical model of signal propagation within the myometrium with parameters influenced by experimental data;
- to use the model to investigate the hypothesis that spatial heterogeneity is crucial in generating global activity in the myometrium; and
- to develop the model to incorporate voltage-dependent gap junctions and investigate the effect of the type of connexin that makes up the gap junction.

Chapters 2 and 3 are self-contained and consist of the manuscript of published papers.

1.11.1 Construction of the mathematical model and spatial heterogeneity

Chapter 2 (Sheldon *et al.*, 2013) introduces the FitzHugh-Nagumo model and the construction of the model network. A mathematical model is developed consisting of an array of 25×25 nodes representing the smooth muscle cells connected by resistors which represent the gap junctions. Each node in the network obeys FitzHugh-Nagumo dynamics. Initially, each cell is considered to be at rest. An exciting stimulus is given to the central cell in the network; the stimulus can take the form of a current input or a pacemaker cell. The strength and presence of inter-cell connections within the network are modified stochastically; that is, the couplings are drawn from statistical distributions and are considered to be non-deterministic. In addition, experimental data from human, mouse, and rat myometrial samples are used to inform the cell parameters and to draw more biologically relevant conclusions.

Chapter 2 (Sheldon *et al.*, 2013) next addresses the role of spatial heterogeneity in an excitable network. Heterogeneity is first introduced through the strength and presence of inter-cell connections. It is shown that in quiescent networks introducing even a modest degree of heterogeneity is sufficient to globally excite a network. In networks with a pacemaker cell as an exciting stimulus, it is demonstrated that a fully connected or strongly coupled network reduces the frequency of pacemaker oscillations. The correlation between the activity of the stimulus cell and its neighbours, as a function of their ℓ_1 separation, is also examined. It is shown that when the stimulus is strongly correlated with its immediate neighbours, excitation is not able to propagate any further. A less well-connected network is optimal for global activity.

1.11.2 Voltage-dependent gap junctions

Chapter 3 (Sheldon *et al.*, 2014) extends the mathematical model of the myometrium to incorporate voltage-dependent gap junctions. It was demonstrated by Miyoshi *et al.* (1996) that the conductance of a gap junction was dependent on the transjunctional voltage of two neighbouring rat myocytes. Two distinct conductance relationships were reported in the Miyoshi paper, which were shown to correspond to gap junctions with either a predominantly connexin-43 (Cx43) composition or a predominantly connexin-45 (Cx45) composition. The Boltzmann distribution fits proposed by Miyoshi are used in the model to calculate the conductance of the gap junction from a given transjunctional voltage. The models constructed in this paper suggest that networks with exclusively Cx45 are not able to propagate activity, whereas Cx43 networks exhibit global excitability. Analysis of human and rat RNA expression in myometrial samples from pregnancy and in labour suggests a down-regulation of Cx45 at term. A hypothesis is proposed in which Cx45 halts the spread of activity in the pregnant uterus, and is removed at the end of pregnancy to deliver the powerful contractions associated with labour.

Chapter 2

Spatial heterogeneity enhances and modulates excitability in a mathematical model of the myometrium

This chapter is the published manuscript of our paper demonstrating the importance of spatial heterogeneity in generating excitability in the myometrium. Herein, the construction of the two-dimensional model is described. The model has nodes assembled into a 25×25 grid with connections between each cell and its four neighbours. Closed boundary conditions are used; that is, the cells at the edge of the lattice are considered to have three neighbours (or two in the case of cells at a corner). Cells at one edge are not directly connected to cells at the other edges. Each node is modelled by the FitzHugh-Nagumo differential equations, and at the start of the simulations both equations are set to be zero, *i.e.* the rate of change of both the excitation and recovery variables is zero. A stimulus is applied to the central cell in the grid, and by changing parameters and the strengths of inter-node connections, the way in which the stimulus spreads throughout the network is investigated.

I first designed the mathematical model in an eight-week mini-project as part of my

Master's degree (awarded in 2012). During the project, I observed that the proportion of cells in the network that become excited after a stimulus to the central cell is dependent on the strength of the inter-cell connections. The bounds on the coupling strength are a function of the size of the applied stimulus.

The work was continued by Marc Baghdadi in a second eight-week mini-project as part of his Master's degree; the assessment method for the project was to write the manuscript for a publication. Marc noted that in networks with a coupling strength outside the excitable range, removing around 20 % of the connections between cells was enough to generate global activity. He also set up the network in which the magnitude of each connection is drawn from a uniform distribution. With uniformly distributed couplings strengths, the standard deviation is shown to be more important in predicting the level of activity than the total coupling magnitude.

I returned to the project in my doctoral studies. I increased the size of the lattices used in all simulations, examined spatial correlation as a function of distance from the stimulated cell, incorporated real-life cell capacitance and resting membrane potential (RMP) values into the cell parameters by fitting distributions to the raw data values, and investigated the effect of replacing the stimulated cell with a pacemaker cell. The rat myocyte capacitance values and RMP values were produced from patch-clamp experiments carried out by Dr Conor McCloskey. Using Marc's manuscript as a basis and incorporating my new results, I wrote the manuscript that is found in this chapter.

Spatial heterogeneity enhances and modulates excitability in a mathematical model of the myometrium

Rachel E. Sheldon[1,3], Marc Baghdadi[1], Conor McCloskey[3], Andrew M. Blanks[3], Anatoly Shmygol[3], and Hugo A. van den Berg[2]

[1] MOAC Doctoral Training Centre, University of Warwick

[2] Systems Biology, University of Warwick

[3] Division of Reproductive Health, Warwick Medical School

J. R. Soc. Interface, 2013, **10**(86), 20130458.

2.1 Abstract

The muscular layer of the uterus (myometrium) undergoes profound changes in global excitability prior to parturition. Here, a mathematical model of the myocyte network is developed to investigate the hypothesis that spatial heterogeneity is essential to the transition from local to global excitation which the myometrium undergoes just prior to birth. Each myometrial smooth muscle cell is represented by an element with FitzHugh-Nagumo dynamics. The cells are coupled through resistors that represent gap junctions. Spatial heterogeneity is introduced by means of stochastic variation in coupling strengths, with parameters derived from physiological data. Numerical simulations indicate that even modest increases in the heterogeneity of the system can amplify the ability of locally applied stimuli to elicit global excitation. Moreover, in networks driven by a pacemaker cell, global oscillations of excitation are impeded in fully connected and strongly coupled networks. The ability of a locally stimulated cell or pacemaker cell to excite the network is shown to be strongly dependent on the local spatial correlation structure of the couplings. In summary, spatial heterogeneity is a key factor in enhancing and modulating global excitability.

2.2 Introduction

The myometrium is the muscular layer that constitutes the bulk of the uterine wall. It is a syncytium of interconnected smooth muscle cells, forming an excitable medium (Garfield *et al.*, 1977), *i.e.* a nonlinear dynamical system that can propagate signals over long distances without damping. In the myometrium, these propagating signals trigger phasic contractions (Parkington *et al.*, 1999b). The behaviour of the myometrium as an excitable medium is thought to be influenced by the spatial variations in the excitability of individual muscle cells as well as the strength of their interconnections (Blanks *et al.*, 2007). The modulation of global excitation by network heterogeneity may play an important role in the myometrium during pregnancy. Sufficient coupling is needed for excitation to spread, but this coupling need not be uniform, or even exist between all cells. The aim of this paper is to examine how spatial heterogeneity, in particular local variations in cell connectivity, affects global excitability. Furthermore, we study the ability of pacemaker cells to drive the network as a function of its spatial heterogeneity.

In the rodent (as in most mammals), the myometrium consists of an inner circular layer and an outer longitudinal layer of smooth muscle cells (Brody & Cunha, 1989b). In humans these layers are less distinct (Weiss *et al.*, 2006). Through most of pregnancy, the myometrium remains in a predominantly quiescent state as the fœtus develops (Challis *et al.*, 2000). However, in the days leading up to parturition, contractile activity in the myometrium undergoes major changes which prepare the uterus for labour (Challis *et al.*, 2000). This activation phase involves molecular changes that lead to an increase in contraction frequency, when compared with mid-gestation (Parkington *et al.*, 1999a). A key characteristic of this phase is a profound change in the connectivity between the myometrial smooth muscle cells.

If a stimulus is applied to a smooth muscle cell, its membrane potential undergoes a de-

polarisation before eventually returning to the quiescent resting value. An excitable cell exhibits an all-or-nothing response: a cell either responds with a full excursion of the membrane potential, or barely at all. In particular, when the stimulus exceeds an excitability threshold, the response is an action potential whose magnitude is independent of the size of the (suprathreshold) stimulus. A consequence of this all-or-nothing behaviour is that a stimulus of sufficient amplitude can be reliably propagated across the network.

Pacemaker cells, by contrast, do not require an external stimulus, but exhibit periodic excitations that drive neighbouring non-pacemaker cells. The presence of specialised pacemaker cells in myometrial tissue is much disputed (Duquette *et al.*, 2005; Wolfs & Rottinghuis, 1970; Kao, 1959; Marshall & Kroeger, 1973). If present, it is likely that the pacemaker cells are not anatomically distinct from non-pacemaker cells and have no fixed location in the uterus (Wray *et al.*, 2001). Rather, they would occur dispersed within the matrix of non-pacemaker cells. Therefore the cells can only be recognised through patterns of electrical activity: a slow depolarisation of the smooth muscle membrane which results in the generation of an action potential (Lodge & Sproat, 1981). The oscillation frequency of a pacemaker cell dictates the rate of uterine contractions.

In order to generate action potentials, a myometrial cell maintains transmembrane gradients of several ionic species by means of active transport across the cell membrane. In humans, the action potential is initiated by an inward, depolarising current carried by calcium ions (Parkington *et al.*, 1999b). Post-excitation, the cells enter a refractory period, during which they are temporarily unable to become excited (Hodgkin & Huxley, 1952d). Electrical coupling between myometrial smooth muscle cells is maintained by intercellular channels through which ions and certain metabolites can pass from one cell to another. Each channel consists of two connexons, one contributed by each of the communicating cells; furthermore, each connexon is a complex of six connexin proteins (Kumar & Gilula, 1996). A gap junction is a cluster of such channels joining two cells electrically. Myometrial gap junctions vary in number over the course of gestation; in fact, an increase in the num-

ber of gap junctions in myometrial tissue is indicative of the onset of labour (Garfield *et al.*, 1977). Moreover, the precise nature of the conditions that stimulate the expression of gap junctions is of considerable clinical importance and an understanding of these conditions may ultimately aid early diagnosis and improve management of preterm labour (Garfield & Maner, 2007).

Heterogeneity has long been known to be a factor in the spatial patterns of activation in excitable systems (Steinberg *et al.*, 2006). In particular, electrical heterogeneities can play a role in cardiac arrhythmias and cause a decrease in propagation velocity through the tissue. The propagation of excitation in spatially extended systems through spiral waveforms has been well-studied (Barkley, 1991; Bub *et al.*, 2002). Here we focus on a question which has received much less attention: whether spatial heterogeneity in connectivity is sufficient to modulate global excitability. We use a mathematical model to investigate how the global excitation of the myometrium is affected by the spatial heterogeneity of the system. Benson *et al.* (2006) analysed a heterogeneously coupled model which is based on FitzHugh-Nagumo dynamics, but this was a continuum-model in which the coupling between cells was not represented explicitly. Spatial heterogeneity was found to assist the transition between quiescence and excitability. However, heterogeneity in coupling alone was not observed to produce synchronous activity. Following these authors, we use the FitzHugh-Nagumo model (FitzHugh, 1961; Nagumo *et al.*, 1962) and introduce heterogeneity by generating stochastic coupling structures based on several statistical distributions. These include empirical distributions obtained from experiments performed on myometrial cells taken from mice at the 15^{th} and 18^{th} day of pregnancy (*i.e.* towards the end of gestation). In addition, we investigate how spatial heterogeneity of the intercellular connections modulates the ability of a pacemaker cell to drive the network.

2.3 Methods

Both *in silico* and *in vitro* methods were employed. Myometrial tissue was simulated in a mathematical network model to determine the effect of spatial variations of coupling strengths on the spread of excitation. Since coupling depends on cell capacitance, as explained later, cell capacitance values were taken from pregnant mouse myometrium to define a statistical distribution for coupling values, which was used to construct an asymmetrically coupled model. Furthermore, data from pregnant mouse myometrial cells were used to simulate statistical variation in resting membrane potential for each cell. These physiologically realistic spatial statistics were also used to determine the efficacy of pacemaker cells.

2.3.1 Experimental methods

2.3.1.1 Electrophysiological measurements

Animals used were C57BL/6 mice which were time-mated (within a 2 hour period) to generate pregnancies with an accurate gestational age. Mice were sacrificed by carbon dioxide inhalation at gestation day 15 or 18, time points towards the end of pregnancy. Strips of myometrium from the longitudinal layer ($2 \times 2 \times 20\,\text{mm}$) were dissected from freshly isolated uteri in ice-cold physiological saline. The strips were washed in Ca^{2+} and Mg^{2+} free HBSS (Fisher Scientific) at $37\,^{\circ}\text{C}$ for 10, 20, and 30 minutes sequentially. This was followed by a 45 minute incubation in HBSS containing Liberase TM (Roche) at a final concentration of 0.13 units/ml. Digestion was terminated by several dilutions with fresh HBSS. Cells were dispersed by slow trituration through a wide-bore fire polished glass pipette in HBSS solution. Single myometrial cells were filtered through a $200\,\mu\text{m}$ gauze and stored in HBSS for use within 6 hours.

The cell membrane was perforated using the antibiotic amphotericin B (600 μg/ml) (Rae *et al.*, 1991). Cell capacitance was measured in the enzymatically isolated smooth muscle cells using the membrane test facility of the Axopatch 700B amplifier (Axon Instruments). Repetitive square voltage pulses of $\Delta V_m = 10\,\text{mV}$ were applied from the holding potential of $-60\,\text{mV}$ and the current response was measured. The integral of the current as a function of time over the decay phase equals the unloaded charge Q_c which is related to the step change in voltage by $Q_c = C_m \Delta V_m$, whence C_m can be calculated. Table 2.1 lists the cell capacitance data obtained in our experiments.

Transmembrane potentials were recorded with an amplifier (Axopatch 700B; Axon Instruments) and a Digidata 1440a computer interface running pCLAMP 10.2 software (Molecular Devices, Sunnyvale, CA, USA). Resting membrane potential values were taken as the mean potential (mV) for the 5 second period immediately after an action potential has occurred.

2.3.1.2 Data analysis

For the 18-day cell capacitance data, a distribution was fitted as follows. The coefficient of variation was calculated as $\xi_1 = \sigma_{18}/\mu_{18}$, where μ and σ are the mean and standard deviation of the experimental data, respectively. The data were normalised by the average value, giving a normalised mean of 1 and a normalised standard deviation of ξ_1. A log-normal distribution can be characterised by two parameters λ and τ such that the mean is equal to $\exp(\lambda + \tau^2/2)$ and the variance equals $\exp(2\lambda + \tau^2)(\exp\left(\tau^2\right) - 1)$. These parameters satisfy the following system:

$$\begin{aligned} 1 &= e^{\lambda + \frac{\tau^2}{2}}, \\ \xi_1^2 &= e^{2\lambda + \tau^2}(e^{\tau^2} - 1). \end{aligned} \tag{2.1}$$

Table 2.1: Cell capacitance data taken from mouse myometrium at 18 day and 15 day gestation.

Day 18 (pF)					Day 15 (pF)		
73	128	93.06	94.71	64.5	56.9	66.85	85.57
83	68	86.63	99.01	62.9	60.04	94.92	47.8
62.4	120	118.19	86.7	62.1	53.77	54.56	83.62
73	47.37	84.8	96.36	62.14	72.84	78.23	76.99
82	80.32	96.76	79.96	93.94	58.9	102.68	61.63
82.2	103.39	63.75	117.59	50.7	71.91	96.26	52.8
86	113.27	45.45	74.87	65.14	71.86	89.5	68.55
69	169.88	57.67	58.57	43.44	73.41	88.8	57.41
66.98	71.66	120.41	93.81	52.18	85.62	54.54	63.45
70	93.19	80.42	89.17	81.23	66.91	40.84	97.75
76.32	81.71	55.4	114.95	111.29	129.69	76.62	78.62
70	68.87	83.47	96.12	57.25	69.97	56.02	120.6
91.35	96.02	74.69	69.4	51.06	105.38	67.88	
62.13	113.15	64.27	75.15	76.51	78.73	62.46	
63.2	93.02	83.95	107.79	99.01	60.27	63.75	
67.89	73.2	82.01	64.65	71.15	59.02	49.11	
73.11	94.31	65.4	50.2	54.39	76.3	46.09	
58.64	73.48	77.12	89.62	106.4	53.58	70.17	
77.35	74.49	107.17	80.78	79.88	95.74	48.5	
110.97	65.16	96.46	63.56	63.5	105.9	66.14	
49.8	91.4	88.01	64.26	76.59	85.36	45.98	
82.17	85.3	61.18	64.56	59.7	54.7	55.01	
103.12	107.36	57.96	70.51		84.34	53.96	
102.31	88.09	114.35	56.65		53.18	73.05	
141.2	58.37	85.54	58.57		58.7	57.5	
64.5	53.05	106.43	68.09		74.91	79.92	
81.23	72.27	69.71	107.2		57.92	59.36	
56.09	59.09	84.84	97.73		60.74	67.66	
56.84	125.48	82.83	57.1		73.51	60.94	
48.78	171.77	107.16	78.62		87.68	52.35	
70.3	113.58	70.98	57.87		84.18	43.57	
88.27	55.54	98.95	83.89		42.93	95.18	
79	79.15	100.65	114.8		54.09	47.91	
70	78.63	63.41	52.9		57.41	64.06	
82	76.59	72.5	96.67		54.51	80.92	
76.41	89.47	114.82	86.9		41.66	43.36	

The non-dimensional cell capacitance for 18-day pregnant mouse data was found to be distributed as e^Z where Z follows a normal distribution with mean -0.03551 and standard deviation 0.2665.

The 15-day data were analysed in a similar fashion. The coefficient of variation was defined as $\xi_2 = \sigma_{15}/\mu_{15}$ using the mean and standard deviation of the experimental data. However, the data were normalised by the 18-day mean μ_{18}, with normalised mean $\alpha = \mu_{15}/\mu_{18}$. Hence

$$\begin{aligned} \alpha &= e^{\lambda+\frac{\tau^2}{2}}, \\ \xi_2^2 &= e^{2\lambda+\tau^2}(e^{\tau^2}-1). \end{aligned} \tag{2.2}$$

The non-dimensional cell capacitance for 15-day pregnant mouse data was found to be distributed as e^Z where Z follows a normal distribution with mean -0.2114 and standard deviation 0.3073.

2.3.2 Myometrial network model

The myometrial network model consists of excitable elements interconnected by resistors representing gap junctions. Heterogeneity is introduced in the form of random variations in the strength of the cell-to-cell couplings. We use various statistical models to generate the networks, including two based on cell population statistics taken from the mice data.

2.3.2.1 Cell model

The Hodgkin-Huxley model of electrogenic cell activity, proposed in 1952, forms the basis for the study of excitable systems (Hodgkin *et al.*, 1952; Hodgkin & Huxley, 1952a,b,c,d). While the Hodgkin-Huxley model has four state variables, FitzHugh (1961) pointed out that the essential dynamical properties are captured by a two-dimensional simplified model, for which Nagumo *et al.* (1962) proposed an electric analogue circuit. The simpli-

fied model is an excitation-relaxation oscillator with a fast ("excitation") state variable v that corresponds to the cell's membrane potential and a slow ("recovery") variable w that corresponds to gating kinetics which repolarise the excited cell. The following ordinary differential equations describe this two-variable model:

$$\frac{d}{dt}v(t) = \frac{1}{\varepsilon}Bv(t)\,(1 - v(t))(v(t) - \alpha) - w(t) - w_0 + I, \tag{2.3a}$$

$$\frac{d}{dt}w(t) = v(t) - \gamma w(t) - v_0, \tag{2.3b}$$

where I is the input current and B, α, γ, w_0, v_0, and ε are positive parameters. The values shown in Table 2.2 were used in the simulations presented in Sections 2.4.1 – 2.4.7, with the exception of ε which was scaled according to cell capacitance in Section 2.4.6.

Table 2.2: Parameter values used in the simulations in Section 2.4.1 – 2.4.7 with the exception of ε in Section 2.4.6 which is scaled according to the modal point of the cell capacitance distributions.

Parameter	B	α	γ	w_0	v_0	ε
Value	3	3	0.05	0.4	0.4	0.2

The equations were solved using the NDSolve function in Mathematica, which uses an LSODA (Livermore Solver for Ordinary Differential Equations) approach. Results were numerically stable under variation in step size.

The behaviour of an isolated cell with the input $I = 0$ is shown in a phase-plane diagram (Figure 2.1a). Whereas the null isocline of w is a straight line, the null isocline of v is a cubic polynomial with an unstable branch in the middle, indicated as a dashed line. In the region left of this unstable branch, the phase point tends towards the left stable branch and ultimately towards the intersection of the null isoclines, which forms a stable stationary point. To the right of the unstable branch, the phase point tends rapidly towards the right stable branch, where the slow dynamics of w will drive it upwards until the branch point is attained. The rapid dynamics of v subsequently drives the phase point back to the left stable branch.

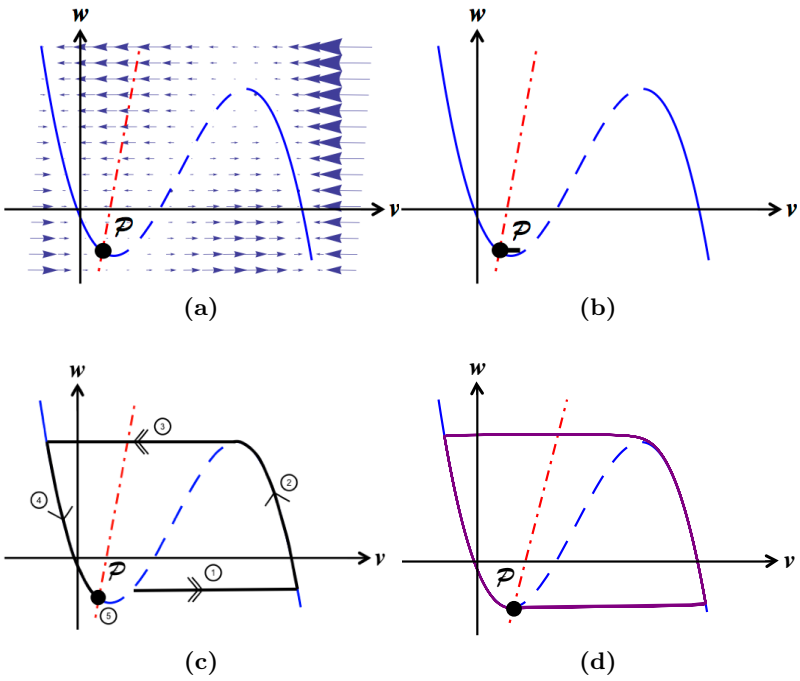

Figure 2.1: Axes labels v and w represent the non-dimensionalised excitation current and recovery current, respectively. (a) Local dynamics described by equations (2.3a) and (2.3b). The dot-dashed line represents the null isocline $\dot{w}(t) = 0$, and the curve represents the null isocline $\dot{v}(t) = 0$. The dashed section of the curve is the unstable branch. The fixed point of the dynamics is at P, where the null isoclines meet. Parameters are given in Table 2.2. (b) and (c) Trajectories, shown as thick, solid lines, vary depending on the initial perturbation from the equilibrium point P. (b) A small perturbation quickly relaxes back to rest. (c) A large perturbation triggers a substantial response. An initial rapid excitation (①) is followed by a period in which the system remains in an excited state (②). After a rapid relaxation (③), the system enters a refractory period in which no further excitation can take place (④), before regaining excitability as it returns to its rest state (⑤). (d) Local dynamics described by equations (2.3a) and (2.3b) for a pacemaker cell. Parameters as in Table 2.3. P is an unstable fixed point, causing continuous re-excitation of the cell after a refractory period.

Excitation corresponds to an excursion along the right stable branch. To reach this branch from the stationary point, a perturbation (Δv) has to be applied on v. If this perturbation is insufficient to move the phase point beyond the unstable branch, the phase point rapidly relaxes back to the equilibrium (Figure 2.1b), whereas sufficiently large perturbations trigger a substantial response (Figure 2.1c). The unstable branch of the null isocline $\dot{v}(t) = 0$ thus represents a threshold for excitation.

2.3.2.2 Lattice model

The individual excitable cells were coupled together through resistors into an $n \times n$ lattice, as illustrated in Figure 2.2a. The lattice was modelled with closed boundary conditions. The resistors represent the gap junctions between any two adjacent cells. The equivalent resistance of the gap junction can be calculated on the basis of the properties of the individual connexon channels. Let the individual connexon have a resistance r_i (Figure 2.2b). Suppose that the gap junction between a given pair of cells consists of n connexons. Since the connexons conduct in parallel, Kirchhoff's law for parallel resistors determines the total resistance R of the gap junction (Figure 2.2c):

$$\frac{1}{R} = \frac{1}{r_1} + \frac{1}{r_2} + ... + \frac{1}{r_n} \, . \tag{2.4}$$

If the connexons have equivalent resistance, $r_i \equiv r$, and $R = r/n$.

2.3.2.3 Coupling constants

A coupling constant K is assigned to each gap junction and defined as follows. The cell membrane is modelled as a capacitor in parallel with a resistor, as indicated in Figure 2.2d. Let Q_i denote the membrane charge of cell i, C_i the cell capacitance and V_i the membrane potential. These quantities are related by

$$\frac{dQ_i}{dt} = C_i \frac{dV_i}{dt} \, . \tag{2.5}$$

The gap junctional current between two cells i and j is given by $(V_j - V_i)/R_{ij}$. Define the coupling constant between cells i and j as $K_{ij} = (C_i R_{ij})^{-1}$ and consider a cell connected to four other cells in a rectangular grid, as shown in Figure 2.2d. The gap junctional

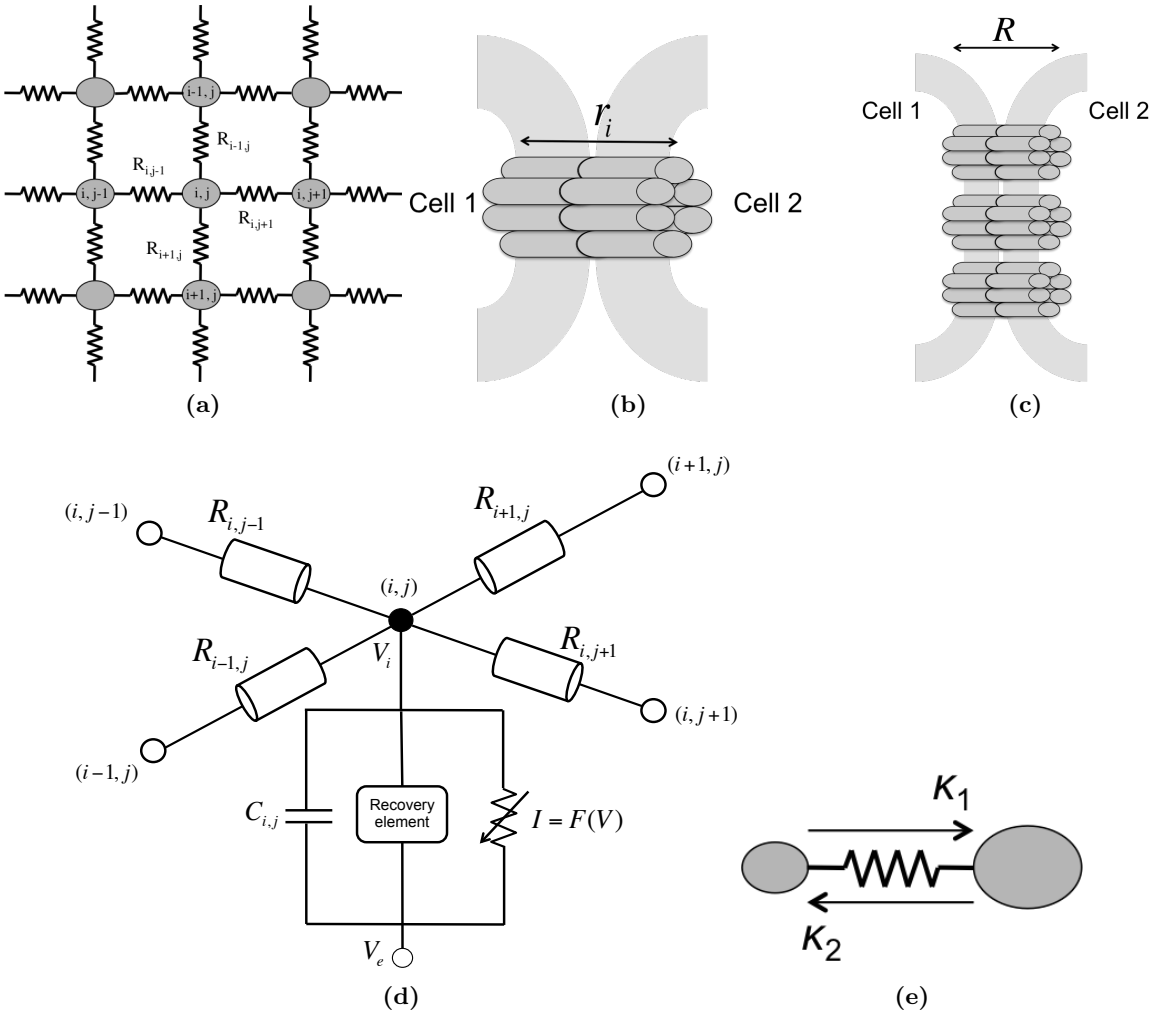

Figure 2.2: (a) Schematic representation of the lattice. Cells are referred to using i, j coordinates; the resistance between cells is denoted by R. The resistances are converted into dimensionless coupling values as detailed in Section 2.3.2.3. (b) and (c) The resistance of a gap junction. (b) The resistance r_i across an individual connexon (consisting of six connexins). (c) A number of connexons link the two cells. The individual connexons act in parallel, giving an equivalent resistance R. (d) Electrical circuit diagram representing the current flow between connected cells. Cell (i, j) is the cell of interest, coupled to four surrounding cells; R represents the resistances in gap junctions. The circuit at cell (i, j) represents a basic model of an excitable system (Keener & Sneyd, 2004). V_e represents the external potential; V_i represents the internal potential; $C_{i,j}$ is the cell capacitance; the recovery element represents the recovery current; and the non-linear current-voltage device (I) represents the fast current. (e) Asymmetry in coupling due to different cell sizes. $\kappa_1 > \kappa_2$.

current for the central cell is a sum of four gap junctional currents:

$$\frac{1}{R_{i+1,j}}(V_{i+1,j}-V_{i,j})+\frac{1}{R_{i,j+1}}(V_{i,j+1}-V_{i,j})+\frac{1}{R_{i-1,j}}(V_{i-1,j}-V_{i,j})+\frac{1}{R_{i,j-1}}(V_{i,j-1}-V_{i,j})$$

where (i,j) denotes the location of the cell on the grid. Hence the voltage dynamics for cell (i,j) is given by

$$\begin{aligned}\frac{d}{dt}V &= \frac{1}{C_{i,j}R_{i+1,j}}(V_{i+1,j}-V_{i,j})+\frac{1}{C_{i,j}R_{i,j+1}}(V_{i,j+1}-V_{i,j})+\frac{1}{C_{i,j}R_{i-1,j}}(V_{i-1,j}-V_{i,j})\\ &+ \frac{1}{C_{i,j}R_{i,j-1}}(V_{i,j-1}-V_{i,j})+\frac{I_{\mathrm{Ch}}}{C_{i,j}} \qquad (2.6)\end{aligned}$$

where I_{Ch} is the total current carried by the ion channels of cell (i,j). The coupling values between any two adjacent cells are as follows:

$$K_{i+1,j}=\frac{1}{C_{i,j}R_{i+1,j}}\,,\quad K_{i,j+1}=\frac{1}{C_{i,j}R_{i,j+1}}\,,\quad K_{i-1,j}=\frac{1}{C_{i,j}R_{i-1,j}}\,,\quad K_{i,j-1}=\frac{1}{C_{i,j}R_{i,j-1}} \qquad (2.7)$$

The coupling value is rendered dimensionless in accordance with the scaled equations for dynamics of the cell network (Equations (2.3a) and (2.3b)). As defined here, K is a rate constant. Dimensionless time t in the FitzHugh-Nagumo model is defined by $t=R_1\tau/D$, where D is the damping coefficient that captures the inertia of the system induced by the gating kinetics, as shown by FitzHugh (1961), dimensional time is represented by τ, and R_1 is the passive resistance of the non-linear current device of the circuit, represented as a tunnel diode by Nagumo *et al.* (1962). Dimensionless coupling is defined as $\kappa=DK/R_1$. The dimensionless equations governing the dynamics of the cell in the (i,j)-th position

are as follows:

$$\frac{d}{dt}v_{i,j}(t) = I_{i,j} + \frac{1}{\varepsilon}Bv_{i,j}(t)(1 - v_{i,j}(t))(v_{i,j}(t) - \alpha) - w_{i,j}(t) - w_0 + \kappa_{i-1,j}(v_{i-1,j}(t) - v_{i,j}(t)) + \kappa_{i+1,j}(v_{i+1,j}(t) - v_{i,j}(t)) + \kappa_{i,j-1}(v_{i,j-1}(t) - v_{i,j}(t)) + \kappa_{i,j+1}(v_{i,j+1}(t) - v_{i,j}(t)), \tag{2.8a}$$

$$\frac{d}{dt}w_{i,j}(t) = v_{i,j}(t) - \gamma w_{i,j} - v_0 \ . \tag{2.8b}$$

Here $I_{i,j}$ is the input current applied to cell (i, j). To render the remaining parameters dimensionless, define $\varepsilon = R_1^2 C_{i,j}/D$ where R_1 is the passive resistance of the nonlinear element, $C_{i,j}$ is the capacitance of cell (i, j) and D is the damping coefficient. The quantities R and D are incorporated into the excitable element depicted in Figure 2.2d. The other parameters were scaled in accordance with the derivation given by Keener and Sneyd (Keener & Sneyd, 2004), as detailed in Section 1.10.2.

2.3.2.4 Initial conditions and activation clusters

The initial conditions for each cell correspond to the resting membrane potential and are given by the real solution to the following simultaneous equations:

$$w_{i,j}(0) = Bv_{i,j}(0)(1 - v_{i,j}(0))(v_{i,j}(0) - \alpha) - w_0, \tag{2.9}$$

$$w_{i,j}(0) = (v_{i,j}(0) - v_0)/\gamma \ . \tag{2.10}$$

A perturbation Δv, representing a short-lasting influx of charge, is applied to the cell at the centre of the lattice, displacing it from its stationary point. The cells that become excited as a consequence of this initial perturbation constitute an activation cluster. The ratio of number of cells in the cluster to the total number of cells in the simulated lattice is used as a measure of the strength of activation.

2.3.2.5 Spatial structuring

Both homogeneously coupled and heterogeneously coupled cell networks are considered. In the spatially homogeneous case, all couplings are equal, i.e., $\kappa_{i,j} = \kappa \ \forall(i,j)$ whereas in the spatially heterogeneous case, the cell-cell couplings κ_{ij} are allowed to vary with i, j. Two further subcases can be distinguished: (i) symmetric coupling, i.e. $\kappa_{i,j} = \kappa_{j,i} \ \forall(i,j)$, and (ii) asymmetric coupling, where $\kappa_{i,j} \neq \kappa_{j,i}$.

Symmetrical coupling — the Bernoulli Lattice To simulate symmetrical coupling, the value $\kappa_{i,j} = \kappa_{j,i}$ is determined probabilistically by

$$\kappa_{i,j} = \begin{cases} \kappa & \text{with probability } p \\ 0 & \text{with probability } 1-p, \end{cases} \tag{2.11}$$

where the limiting case $p = 1$ represents spatial homogeneity. We refer to the lattice defined by Equation (2.11) as the Bernoulli Lattice. Heterogeneity in the Bernoulli Lattice is modulated by varying the amount of connectivity in the lattice, expressed by the parameter p representing the probability of a connection existing between any two given cells.

Symmetrical coupling — Uniformly distributed A second type of symmetrical heterogeneity is introduced using a lattice with connections drawn from uniform distributions. In particular, the intercellular couplings are modelled as independent uniform variates on $[0.5, 10]$. Coupling strengths are within a range that are shown in Section 2.4.1 to promote network excitation.

Spatial correlation in the coupling structure Distance to the stimulated cell is expressed using the ℓ_1 ("city-block") measure; Figure 2.3 labels cells according to their ℓ_1-distance to the central cell on a 5×5 lattice. The correlation function C_r, where r is

the ℓ_1-distance, is defined as follows:

$$C_r = \langle \langle (\bar{\kappa_0} - \bar{\bar{\kappa}})(\bar{\kappa_i} - \bar{\bar{\kappa}}) \rangle_{\forall\, i \text{ at } r} \rangle_{\text{simulated networks}} \tag{2.12}$$

where $\bar{\bar{\kappa}}$ denotes the grand mean of coupling over the network and $\bar{\kappa_i}$ is the mean coupling of cell i.

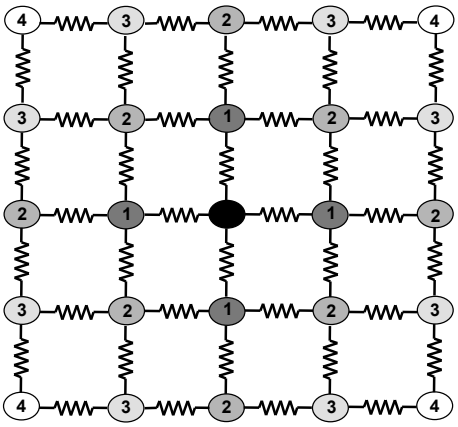

Figure 2.3: Schematic representation of the ℓ_1 distances in a 5×5 lattice, indicated by number and on a graded scale from dark to light. The stimulated cell is indicated in black.

Asymmetrical coupling — Cell capacitances Asymmetrical coupling is introduced by allowing variation in cell capacitances (with symmetrical gap junctional conductances). A larger cell has a larger capacitance, and as a result will be more weakly coupled to its neighbours since $K_{i,j} = (C_i R_{i,j})^{-1}$ will be smaller (Figure 2.2e). The model assumes that the cell capacitance values are independently log-normally distributed; calculation of realistic parameter values is detailed in Section 2.3.1.2. A resistance value is chosen from within a window of values that permit global excitability.

The value of the scaled parameter ε is proportional to the capacitance of the cell. Accordingly in stimulations using day 18 data, the value of ε is normalised by the modal point of the 18-day distribution. Similarly, ε is normalised by the modal point of the 15-day distribution in day 15 simulations.

Variability in resting membrane potential A normal distribution was fit to the normalised resting membrane potential data. The 18-day data serve as a reference point. The non-dimensional resting membrane potential for 18-day pregnant data is normally distributed with mean 1 and standard deviation 0.1615, whereas the non-dimensional resting membrane potential for 15-day pregnant data is normally distributed with mean 1.046 and standard deviation 0.08737.

Equations (2.9) and (2.10) can be solved simultaneously to find an expression for the value of v in the steady state. Retaining only linear terms we find that the scaled resting membrane potential $\bar{v}$ is proportional to $v_0 - \gamma w_0$.

A value $v_{i,j}$ is sampled from the resting membrane potential distribution for each cell (i, j) in the network. The dependent parameters γ and w_0 are then multiplied by $v_{i,j}$ to introduce variability into the model. Introducing variability through the parameter v_0 produces non-sensical results.

Multiplying γ and w_0 by $v_{i,j}$ alters the phase portrait for each cell. We therefore examine the effect of the variability in resting membrane potential (and so gestation period) on the minimum perturbation required to excite an isolated cell. Simulations were run with the only asymmetry being the variation in resting membrane potential, and also with an asymmetry in the cell capacitances. Relative cluster sizes were recorded for a range of coupling strengths and initial perturbations with varying connectivity p.

An increase in variability in resting membrane potential is seen as pregnancy progresses. Therefore, by assuming a linear relationship between day 15 and day 18 data, we extrapolate resting membrane potential variability for time points outside this range to examine the trend of excitability throughout pregnancy.

Pacemaker cells Activity waves can be initiated by external stimuli (for example, oxytocin) or by intrinsic activity of spontaneously active cells. Such cells can be obtained by

adjusting the parameters to shift the position of its null isoclines. The pacemaker cell parameter values are given in Table 2.3. The straight line null isocline passes directly through the local minimum of the cubic null isocline to create an unstable fixed point at the rest state of the cell, as indicated in Figure 2.1d. In effect, the cell continually re-excites itself. The cells are connected symmetrically with a constant coupling value.

Table 2.3: Parameter values used for pacemaker cells.

Parameter	B	α	γ	w_0	v_0	ε
Value	3	3	0.1	0.4	0.7	0.2

The models used in this study are summarised in Table 2.6.

2.4 Results

To investigate how the spatial heterogeneity affects the global excitability of the network, the spatially homogeneous case is studied first, followed by the heterogeneous coupling case.

2.4.1 Fully connected square lattice

Simulations of a spatially homogeneous square lattice indicate that for each perturbation there is a window of coupling strengths in which global excitation of the lattice is possible. For instance, a dimensionless initial perturbation of $\Delta v = 1$ in a fully connected lattice of size 25×25, produces global excitation for coupling strengths (κ) between 0.76 and 5.12. Below 0.76, the excitation does not spread beyond the cell to which the stimulus was applied. Above 5.12, no cell is able to become excited, including the perturbed cell. The surrounding cells act as a current sink; when the coupling is too strong, this effect prevents excitation. The symbols $\kappa_{\min}$ and $\kappa_{\max}$ denote the boundaries of the window of excitation; for the standard dimensionless perturbation $\Delta v = 1$ these values are 0.76 and

5.12.

The ranges of perturbation and coupling values that permitted global excitation are shown in Figure 2.4 for a 25×25 lattice. Simulations run for smaller and larger lattices produce qualitatively similar excitation curves.

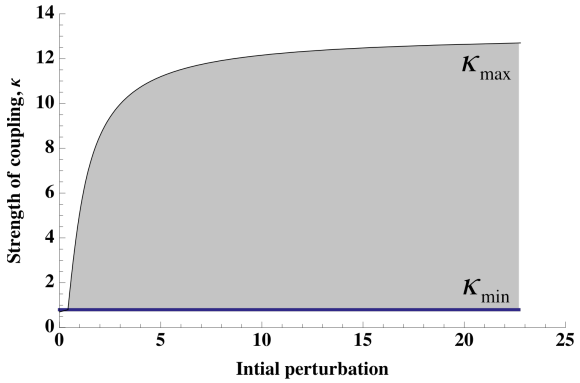

Figure 2.4: The range of parameters that allow global excitation (shaded region) in a 25×25 lattice. The strength of coupling and initial perturbation are non-dimensionalised. The horizontal line corresponds to $\kappa_{\min}$ below which global excitation is impossible; $\kappa_{\max}$ defines the maximum coupling value for each perturbation and corresponds to the curve bounding the shaded region from above.

2.4.2 Symmetric coupling in the Bernoulli Lattice

Simulations were run with a lattice of 25×25 cells and the coupling strengths were chosen in the range from 1 to 2.5 (i.e. within the window of global excitation for an initial perturbation of 1). Initial perturbations took the following values: 1, 1.5, 2, and 2.5. As the connectivity of the lattice (p) increases, the number of cells that become excited (the relative cluster size) increases in a sigmoidal fashion, as shown in Figure 2.5. The response curve does not substantially vary with lattice size, coupling value, or initial perturbation (Figures 2.5 and 2.6), which suggests that connectivity is the dominant factor governing the excitability of the system.

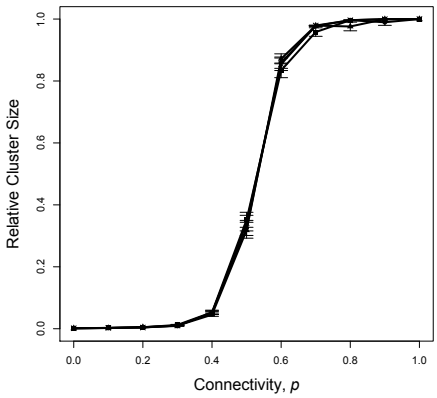

Figure 2.5: Relative cluster size versus connectivity for symmetrical coupling in the Bernoulli lattice. Points show mean ± SEM of 100 simulations for a 25×25 lattice. In all simulations, a coupling strength of $\kappa = 1$ was chosen. The four lines represent initial perturbations of 1, 1.5, 2 and 2.5, shown in the same colour due to the proximity of the curves.

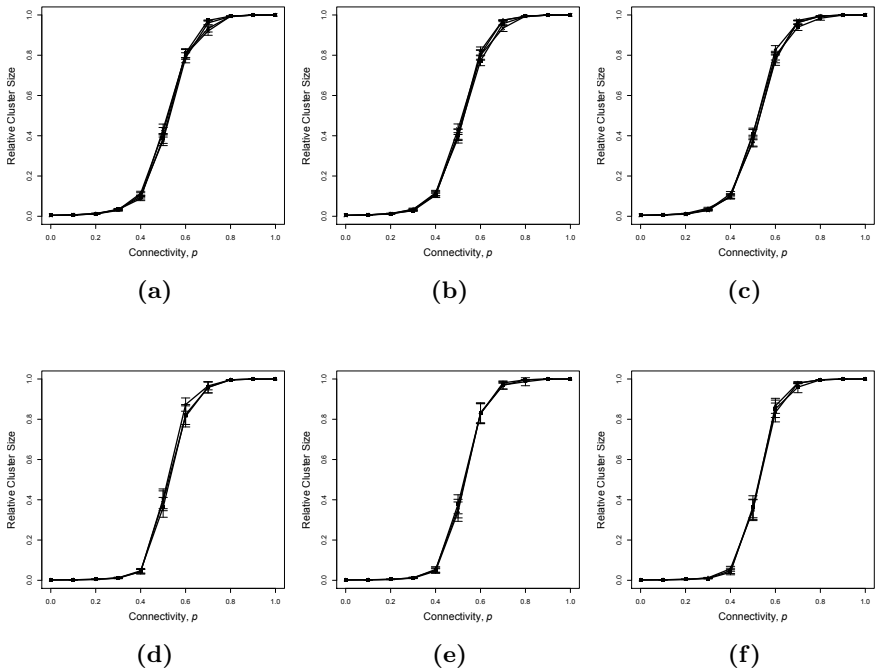

Figure 2.6: Relative cluster size versus connectivity. Points show mean ± SEM of 100 simulations. The four lines represent initial perturbations of 1, 1.5, 2 and 2.5, all shown at the same shade due to their close proximity. (a)-(c) are for a 15×15 lattice, (d)-(f) for a 25×25 lattice. (a) & (d): $\kappa = 1.5$. (b) & (e): $\kappa = 2.0$. (c) & (f): $\kappa = 2.5$.

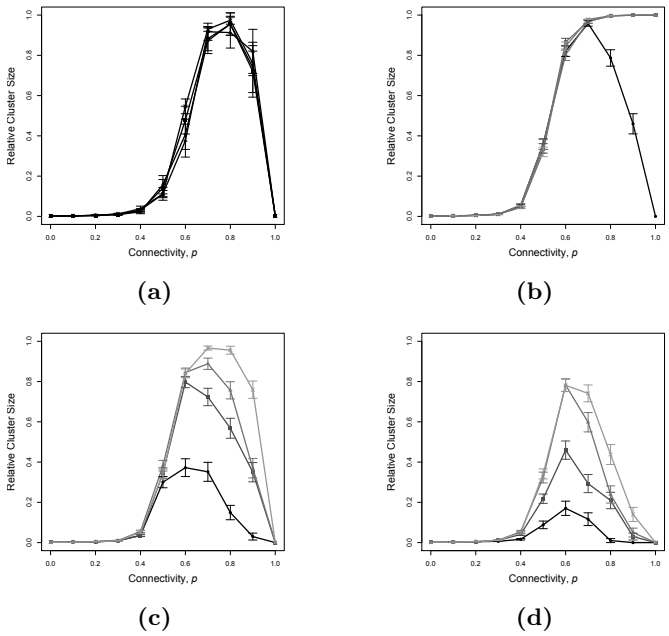

Figure 2.7: Relative cluster size versus connectivity for K values outside the window of excitability in the symmetrical Bernoulli lattice. Points show mean ± SEM of 100 simulations for a lattice size of 25×25. (a) $\kappa = 0.76$ ($\kappa_{\min}$), the four lines represent initial perturbations of 1, 1.5, 2 and 2.5 and are shown in the same colour due to the proximity of the curves; (b) $\kappa = 5.2$ ($\kappa_{\max}$), the four lines represent initial perturbations of 1, 1.5, 2 and 2.5. The dark curve represents an initial perturbation of 1, perturbations of 1.5, 2 and 2.5 are shown in the same (lighter) colour due to the proximity of the curves; (c) $\kappa = 10$, the four lines represent initial perturbations of 1, 1.5, 2 and 2.5 on a graded scale from dark to light; (d) $\kappa = 15$, the four lines represent initial perturbations of 1, 1.5, 2 and 2.5 on a graded scale from dark to light.

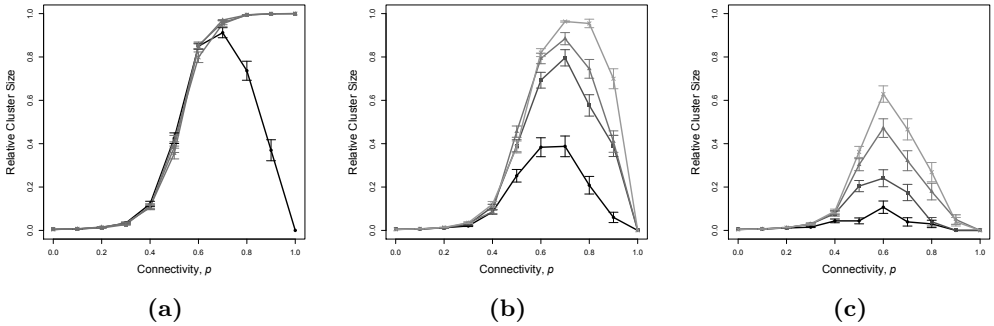

Figure 2.8: Relative cluster size versus connectivity for large κ. Points show mean ± SEM of 100 simulations. All simulations were for a lattice size of 15×15. The four lines represent initial perturbations of 1, 1.5, 2 and 2.5 on a graded scale from dark to light. (a) $\kappa_{\max} = 5.2$, perturbations of 1.5, 2 and 2.5 are shown at the same shade due to their close proximity. (b) $\kappa = 10$. (c) $\kappa = 20$.

Coupling values were chosen from outside the window of global excitation, and the effect of spatial heterogeneity in coupling was investigated by varying lattice connectivity as before. The behaviour for coupling values greater than or equal to the maximum coupling value $\kappa_{\max}$ is shown in Figures 2.7b – 2.7d for initial perturbations Δv of 1, 1.5, 2, and 2.5. The behaviour for the minimum coupling value $\kappa_{\min}$ is shown in Figure 2.7a. In both cases, the sigmoidal curve was replaced by a negatively skewed bell curve, indicating that even when global excitation is precluded in the fully connected lattice, it can be attained in a partially connected system. Connectivity attains an optimum in the range $p = 0.6 - 0.8$. At these probabilities, either more than 90 % of the cells or fewer than 10 % of cells become excited. The averaging of the cluster sizes over 100 replicates underlies the decline in cluster size seen in the bell-shaped curve. At $p = 1$, this all-or-nothing behaviour is absent. Lattice size had no effect on this result (Figure 2.8).

2.4.3 Global transitions

Simulations around boundary points $\kappa_{\min}$ and $\kappa_{\max}$ were performed to elucidate the transition from quiescence to global excitation, at varying levels of connectivity, *viz.* $p = 1$, $p = 0.7$, $p = 0.5$ and $p = 0.3$. Initially, simulations were run at $\kappa_{\max}$ with perturbations from 0.5 to 1.5 at probabilities of 1, 0.7, 0.5, and 0.3 (Figure 2.9a). In the fully connected lattice ($p = 1$) no excitation occurs for $\Delta v < 1$, whereas global excitation is attained for $\Delta v > 1$. At reduced connectivity, the lattice exhibits global excitation even at perturbations $\Delta v < 1$. The reduced connectivity allows a more gradual increase in cluster size with increased perturbation. This effect was especially pronounced at $p = 0.7$, an almost exactly optimal level of connectivity.

A similar phenomenon occurs near the lower bound (Figure 2.9b). The fully connected lattice is unexcitable when the coupling is below $\kappa_{\min}$ whereas global excitation can occur at couplings above this value. At reduced levels of connectivity, coupling values below

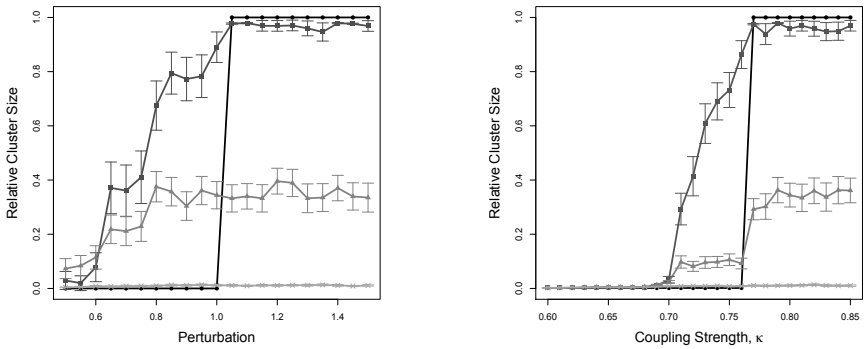

(a) **(b)**

Figure 2.9: Relative cluster size versus small changes in parameters. Points show mean ± SEM of 100 simulations, for a lattice size of 25×25. The four lines represent probabilities of connections between cells of 1, 0.7, 0.5, and 0.3 on a graded scale from dark to light. Anomalous cluster sizes are too few to affect the average. (a) Fixed coupling value $\kappa_{\max} = 5.12$ with varying perturbation; (b) Fixed initial perturbation $\Delta v = 1.0$ with varying coupling values around $\kappa_{\min} = 0.76$.

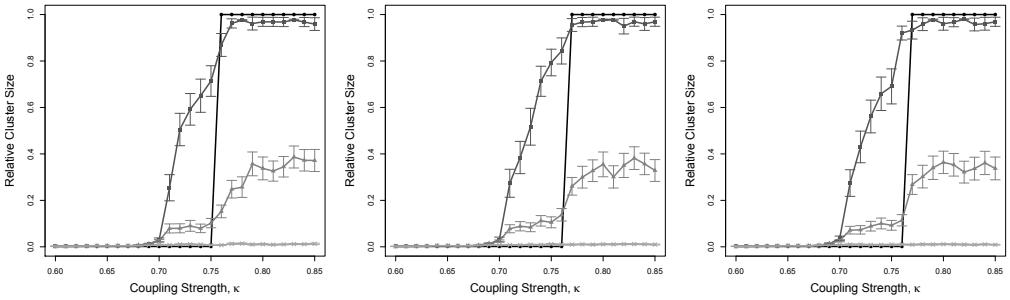

(a) **(b)** **(c)**

Figure 2.10: Relative cluster size per coupling value κ close to $\kappa_{\min}$ for varying initial perturbations. Points show mean ± SEM of 100 simulations, all for a square lattice of size 25×25. The four lines represent probabilities of connections between cells of 1.0, 0.7, 0.5, and 0.3 on a graded scale from dark to light. (a) Perturbation $\Delta v = 1.5$; (b) Perturbation $\Delta v = 2.0$; (c) Perturbation $\Delta v = 2.5$.

the lower bound are associated with activation clusters of increasing size. The strength of the perturbation, however, has little effect on the cluster size (Figure 2.10), indicating that connectivity *per se* is the dominant factor governing the transition to global excitability.

2.4.4 Uniformly varying coupling strengths

The sum and standard deviation of the coupling strengths of the four cells surrounding the excited cell were examined for the fully connected lattice with couplings sampled from a uniform distribution between 0.5 and 10. For a combined coupling value over the four neighbouring cells (κ_{T}) less than 21.0, the cluster always exhibits global excitation, with every cell becoming excited. For κ_{T} greater than 22.2, the couplings around the perturbed cell do not allow any neighbouring cell to become excited. This points to a threshold for global excitation in a fully connected system with coupling sizes sampled from a uniform distribution. For κ_{T} between these two values, an increase in the standard deviation between the coupling strengths is correlated with a reduced global threshold for excitation (Table 2.4). The ability to achieve global excitation does not depend on the combined strength of the couplings to the neighbouring cells. The relationship between standard deviation and global excitation around the upper bound of coupling strengths (Section 2.4.1) for $\Delta v = 1$ is shown in Table 2.5. The standard deviation has a more pronounced effect on the cluster size than κ_{T}. At constant κ_{T}, there is a standard deviation threshold beyond which the system cannot achieve global excitation.

Table 2.4: Total K and standard deviation of K around excited cell, for a fully connected 25×25 square lattice with couplings drawn from a uniform distribution. $K_h \in [0.5, 5]$, $K_v \in [5, 10]$. Data shown for a total coupling K between 21 and 22.2, and arranged in increasing standard deviation.

Total K	St. Dev. K	Relative Cluster Size	Total K	St. Dev. K	Relative Cluster Size
21.7154	1.0451	0	21.3824	2.8636	1
21.1468	1.1987	0	21.4167	2.9621	1
21.0597	1.3439	0	21.4531	3.0879	1
21.5622	1.4293	0	21.7490	3.1979	0
21.0219	1.8396	0	22.0847	3.2100	0
21.6085	1.9802	0	21.8734	3.2423	0
21.4277	2.0487	0	21.8849	3.2522	0
21.3947	2.0704	0	21.7770	3.3834	1
22.1547	2.0914	0	22.0845	3.4102	0
21.2315	2.1224	0	21.5571	3.4309	1
22.1620	2.1281	0	21.1673	3.5437	1
21.3721	2.1308	0	21.5300	3.5484	1
21.3219	2.1786	0	21.6417	3.5931	1
21.0063	2.3078	1	21.0154	3.5979	1
22.0352	2.3201	0	21.7100	3.6670	1
21.5215	2.4436	0	21.1944	3.7901	1
21.5689	2.4796	0	21.6877	3.7981	1
21.1142	2.5038	1	21.7880	3.8116	1
21.7203	2.5616	0	21.5994	4.1018	1
21.7749	2.6418	0	21.2375	4.1204	1
21.8832	2.7984	0	21.3395	4.1600	1
21.6974	2.7986	0	21.8725	4.2026	1

Table 2.5: Standard deviation of coupling values around the central cell affects global excitation in a fully connected 25×25 square lattice, with an initial perturbation of 1.0. Total coupling is kept constant around the perturbed cell to allow for standard deviation comparisons only.

Horizontal K	Vertical K	St. Dev. K	Relative Cluster Size	Horizontal K	Vertical K	St. Dev. K	Relative Cluster Size
5.2	5.2	0.0	0	7.9	2.5	3.1177	1
5.3	5.1	0.1155	0	8.0	2.4	3.2332	1
5.4	5.0	0.2309	0	8.1	2.3	3.3486	1
5.5	4.9	0.3464	0	8.2	2.2	3.4641	1
5.6	4.8	0.4619	0	8.3	2.1	3.5796	1
5.7	4.7	0.5774	0	8.4	2.0	3.6950	1
5.8	4.6	0.6928	0	8.5	1.9	3.8105	1
5.9	4.5	0.8083	0	8.6	1.8	3.9260	1
6.0	4.4	0.9238	0	8.7	1.7	4.0415	1
6.1	4.3	1.0392	0	8.8	1.6	4.1569	1
6.2	4.2	1.1547	0	8.9	1.5	4.2724	1
6.3	4.1	1.2702	0	9.0	1.4	4.3879	1
6.4	4.0	1.3856	0	9.1	1.3	4.5033	1
6.5	3.9	1.5011	0	9.2	1.2	4.6188	1
6.6	3.8	1.6166	0	9.3	1.1	4.7343	1
6.7	3.7	1.7321	1	9.4	1.0	4.8497	1
6.8	3.6	1.8475	1	9.5	0.9	4.9652	1
6.9	3.5	1.9630	1	9.6	0.8	5.0807	1
7.0	3.4	2.0785	1	9.7	0.7	5.1962	1
7.1	3.3	2.1939	1	9.8	0.6	5.3116	0.04
7.2	3.2	2.3094	1	9.9	0.5	5.4271	0.04
7.3	3.1	2.4249	1	10.0	0.4	5.5426	0.04
7.4	3.0	2.5403	1	10.1	0.3	5.6580	0.04
7.5	2.9	2.6558	1	10.2	0.2	5.7735	0.04
7.6	2.8	2.7713	1	10.3	0.1	5.8890	0.04
7.7	2.7	2.8868	1	10.4	0.0	6.0044	0.04
7.8	2.6	3.0022	1				

2.4.5 Uniformly varying coupling strengths — Bernoulli Lattice

The two sources of heterogeneity were combined to give a lattice with coupling values drawn from a mixed distribution with a finite probability at the value zero and a uniform distribution over non-zero values. The isotropic lattice was studied for various values of the initial perturbation (Figure 2.11a). The negatively skewed bell-shaped curve was observed with a fixed coupling value for the smallest perturbation. Compared with the Bernoulli lattice, larger clusters are observed, at higher connectivity values. Again, the declining slope of the bell-shaped curve for a perturbation of 1 is associated with all-or-nothing behaviour. The transition from quiescence to global excitability as a function of p, at fixed Δv, is gradual, in contrast to the Bernoulli lattice (Figure 2.11b).

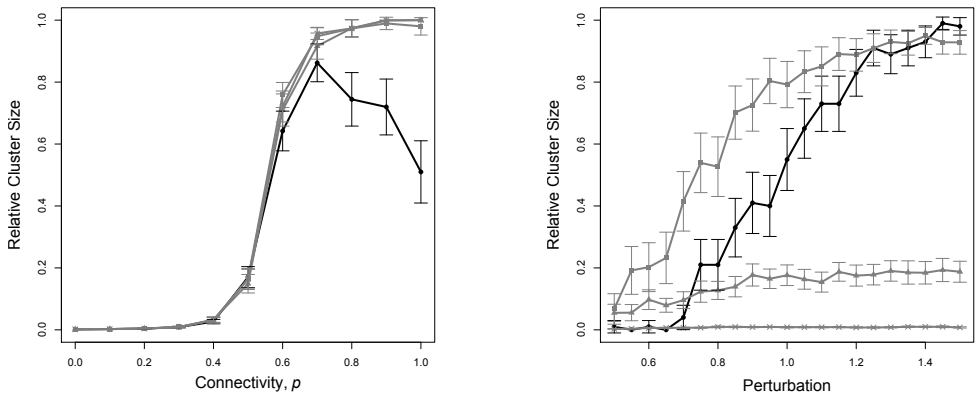

(a) **(b)**

Figure 2.11: (a) Relative cluster size versus connectivity, for random coupling values. All points show mean ± SEM of 100 simulations, for an isotropic lattice of size 25×25. The four lines represent initial perturbations of 1, 1.5, 2, and 2.5. A perturbation of 1 is shown in the darkest shade. Lighter colours represent perturbations of 1.5, 2, and 2.5 due to their close proximity. All $\kappa \in [0.5, 10]$. (b) Relative cluster size versus perturbation, for an isotropic square lattice of size 25×25. All $\kappa \in [0.5, 10]$. Points show mean ± SEM of 100 simulations. The four lines represent probabilities of connections between cells of 1.0, 0.7, 0.5, and 0.3 on a graded scale from dark to light. Anomalous cluster sizes are too few to affect the average.

2.4.5.1 Role of spatial correlation in the coupling structure

The spatial correlation function exhibits a striking difference between networks in which more than 90 % of the cells become excited, and those in which fewer than 10 % of the cells become excited. The latter are characterised by a strong correlation between the stimulated cell and the $r = 1$ neighbouring cells. The strong local coupling strengths act as a sink, preventing the current from dissipating throughout the network (as illustrated in Figure 2.12a where couplings are strong between the central cell and its $r = 1$ neighbours). In contrast, a low degree of spatial correlation between the stimulated cell and its $r = 1$ neighbour is associated with networks in which 90 % of cells become excited. An example of such a network is given in Figure 2.12b. As the heterogeneity decreases from $p = 0.6$ to $p = 0.9$ (Figures 2.13a – 2.13d) this effect becomes less pronounced. At a connectivity of $p = 1$, this difference in correlation is not observed (Figure 2.13e).

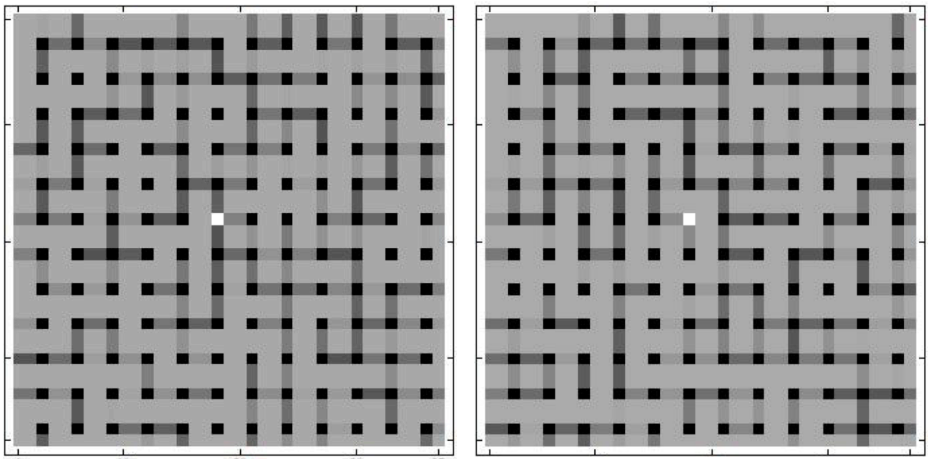

(a) **(b)**

Figure 2.12: The topology of the central 12 × 12 cells of a network (truncated from the 25 × 25 cell network for clarity) where the connections are drawn from a uniform distribution between 5 and 10. The stimulated cell is illustrated in white, all other cells are shown in black. The connections between cells are shown on a graded scale from light to dark grey with increasing connection. The probability of connection is 0.6, and the initial perturbation is 1. (a) A network which is not able to achieve full excitation. There is a high correlation between the stimulated cell and its $r = 1$ neighbours. (b) A network which is able to achieve full excitation. There is a low correlation between the stimulated cell and its $r = 1$ neighbours.

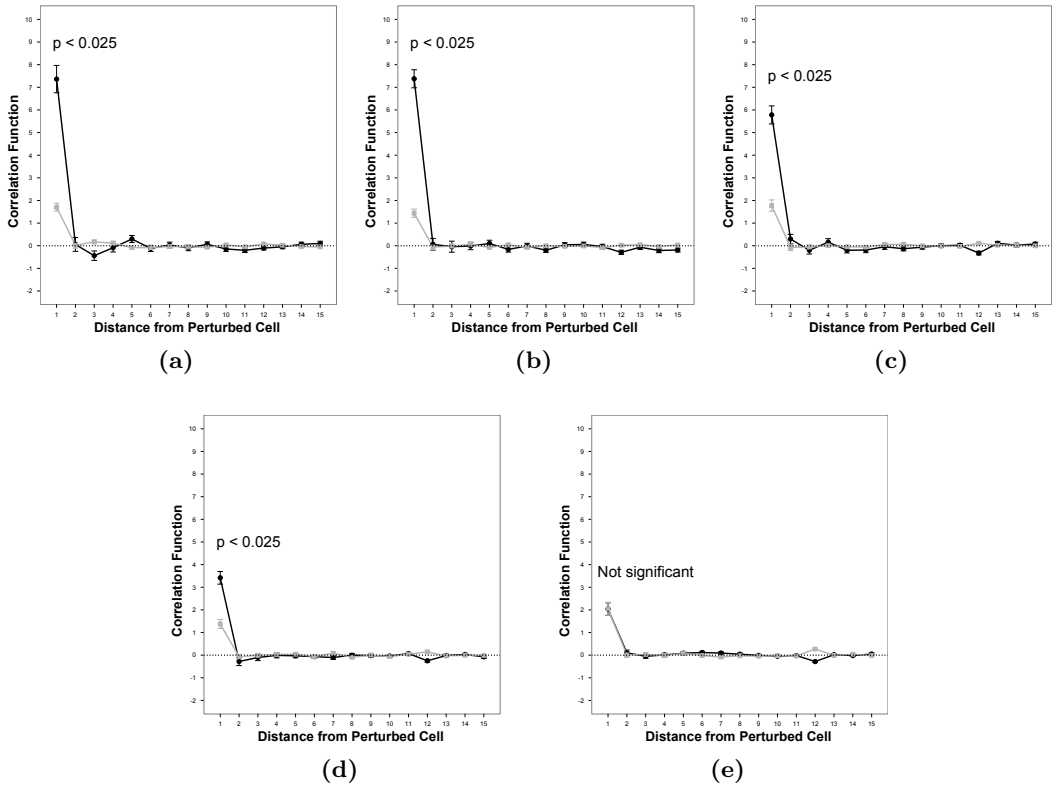

Figure 2.13: Correlation function versus increasing distance from the stimulated cell. Points show mean ± SEM of 100 simulations. The darker lines correspond to networks with fewer than 10 % of cells becoming excited. The paler lines correspond to networks with more than 90 % of cells becoming excited. The initial perturbation is kept constant at 1. Each graph represents a different probability of connections existing between any two given cells. (a) Probability = 0.6; (b) Probability = 0.7; (c) Probability = 0.8; (d) Probability = 0.9; (e) Probability = 1.

2.4.6 Asymmetrical coupling — cell capacitance

The couplings between cells can be adjusted to represent differences in cell size as explained in Section 2.3.2.5. Realistic distributions were derived from data obtained in 15-day pregnant and 18-day pregnant mice, shown in Figure 2.14. Figure 2.15 shows a model with scaled ε values, a constant gap-junctional resistance, and log-normally distributed capacitance values. At perturbations of 1.5, 2.0, and 2.5 a sigmoidal curve is observed, with an increased probability of cell-to-cell coupling corresponding to a larger cluster size. For $\Delta v = 1$, a bell-shaped curve is observed, with slightly reduced connectivity resulting in a

larger relative cluster size. The graph shown is for the day-18 simulations. There was no discernible difference between day-15 and day-18 simulations. It appears that this variation between gestation days is not sufficient to remove the cells from the excitable range displayed in Figure 2.4. In contrast to the symmetrically coupled case discussed earlier (Figure 2.5) the curve is not sigmoidal for an initial perturbation of 1, suggesting that an asymmetrically coupled system requires a larger initial perturbation before full excitation can be achieved at full connectivity.

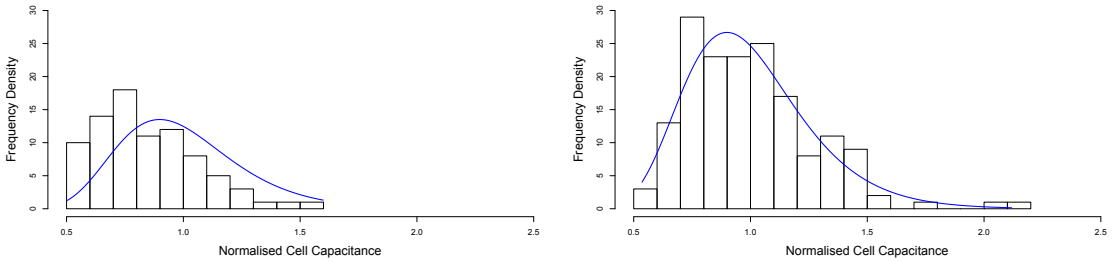

(a) **(b)**

Figure 2.14: Histograms and maximum-likelihood fitted log-normal distributions representing capacitance values for (a) 15-day pregnant mice; (b) 18-day pregnant mice.

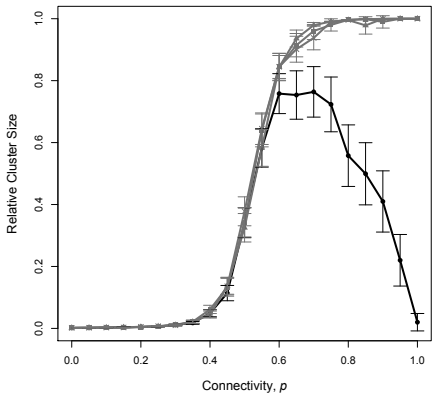

Figure 2.15: Relative cluster size versus connectivity, for a selection of initial perturbations. All points show mean ± SEM of 100 simulations, for an asymmetrically coupled lattice of size 25×25. The four lines represent initial perturbations of 1, 1.5, 2 and 2.5. Perturbations of 1 are shown in the darkest shade, and the remaining perturbations are shown lighter due to their close proximity. Capacitance values are sampled from 18-day distribution. There is no discernible difference in the model using capacitance values sampled from 15-day distribution.

2.4.7 Variation in resting membrane potential

If the resting membrane potential is allowed to vary between cells, the pattern of spatial heterogeneity enhancing excitability persists. Figure 2.16a indicates the value of Δv required to excite the cell for a given resting membrane potential mean and standard deviation. The means and standard deviations for other gestation days were determined by interpolation and extrapolation, assuming a linear relationship between the 15-day and 18-day data. With the change in resting membrane potential, the cells' phase portraits change over time, resulting in a smaller Δv-value required for excitation of an individual cell as the system approaches parturition.

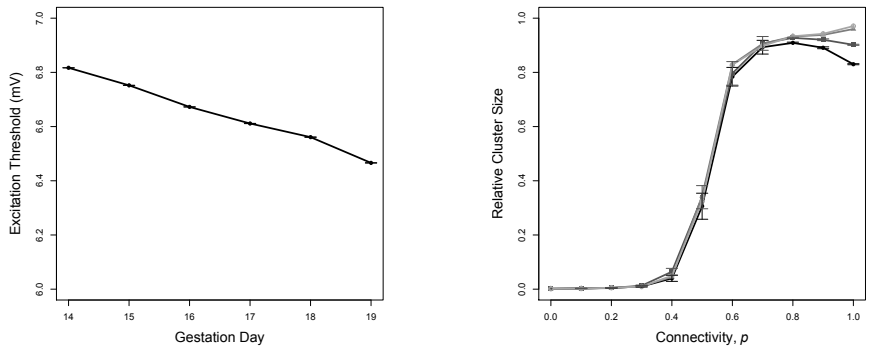

(a) **(b)**

Figure 2.16: (a) Excitation threshold a cell needs to overcome versus the gestation day. The points from day 15 and day 18 gestations are determined by experimental data. Other points are generated by interpolation and extrapolation based on a linear relationship between day 15 and day 18 data. All points show mean ± SEM of 100 simulations. (b) Relative cluster size versus connectivity, for an initial perturbation of 1. All points show mean ± SEM of 100 simulations, for a lattice size of 25×25. There is no asymmetry due to cell capacitance variation: $\kappa = 1$. Lines represent simulations incorporating pre day 15 variation, day 15 variation, day 18 variation, and post day 18 variation on a graded scale from dark to light.

Figure 2.16b illustrates the relationship between relative cluster size and connectivity for systems with pre day 15, day 15, day 18, and post day 18 resting membrane potential variation. We see that a system with resting membrane potential variation only, at a constant coupling strength ($\kappa = 1$), fails to achieve full excitation. However, increased

gestational age correlates with increased excitability.

Figure 2.17 displays the results of variation in resting membrane potential and cell capacitance, for all four gestation time point combinations. Capacitance variation endows some cells with a greater ability to excite the network, since larger cells can accommodate the current sink effect exerted by its neighbours and act as a buffer, enabling all cells to become excited. It appears that excitability is optimal with larger perturbations in the case combining capacitance and resting membrane potential variability sampled from the 18-day distribution. In contrast to the symmetrically coupled case (Figure 2.5), an asymmetrically coupled system requires a larger initial perturbation before full excitation can be achieved at full excitability.

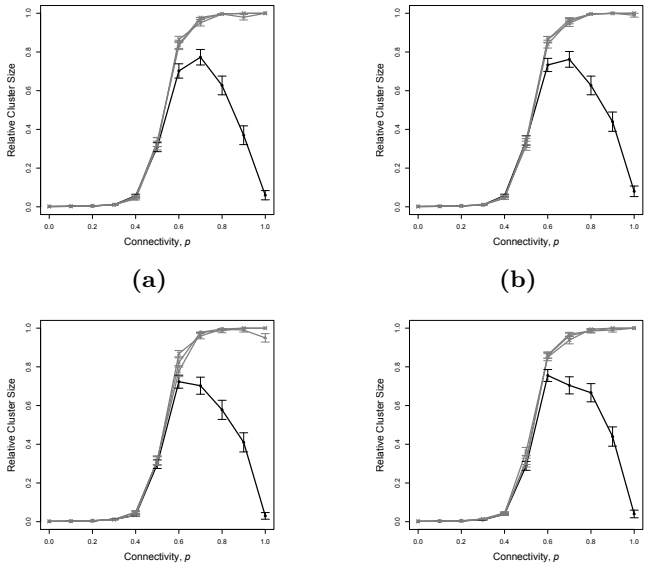

Figure 2.17: Relative cluster size versus connectivity, for a selection of initial perturbations. All points show mean ± SEM of 100 simulations, for a lattice size of 25×25. The four lines represent initial perturbations of 1, 1.5, 2 and 2.5 on a graded scale from dark to light. Perturbations of 1.5, 2 and 2.5 are shown at the same shade due to their close proximity. (a) Resting membrane potentials and capacitances sampled from day 15 distribution; (b) Resting membrane potentials sampled from day 15 distribution, cell capacitances sampled from day 18 distribution; (c) Resting membrane potentials sampled from day 18 distribution, cell capacitances sampled from day 15 distribution; (d) Resting membrane potentials and capacitances sampled from day 18 distribution.

2.4.8 Pacemaker cells

In networks with a pacemaker cell, the frequency of oscillations of the pacemaker is affected by connectivity. The current sink represented by neighbouring cells can reduce the frequency of the pacemaker cell's free-running oscillation or even cause the cell to cease cycling altogether. The probability of such a complete cessation of cycling increases with connectivity (Figure 2.18a). With the exception of very small coupling values κ, at full connectivity the pacemaker cell is not able to maintain its excitability and subsequently none of the surrounding cells are able to become excited. At small values of κ the pacemaker maintains its excitability and pacemaker frequency is hardly affected by increased probability of connection. Heterogeneity of the spatial coupling structure thus appears to be an important modulator of excitability.

The relationship between connectivity and the frequency of oscillations of the pacemaker cell is shown in Figure 2.18b, calculated as an average of simulations in which the pacemaker continues to cycle at a finite frequency. As the connectivity p increases from 0 to 1, the frequency of oscillations of the pacemaker cell decreases, due to the drain of current to the surrounding connections. At high coupling strength values of $\kappa = 5$ and $\kappa = 10$, connectivity has no effect on frequency since the only way for a pacemaker to retain a finite frequency at these coupling strengths is to be essentially isolated in the network. This is illustrated in Figure 2.19 which shows the topology of a sample pacemaker network with finite frequency, and the topology of a sample network where the pacemaker's frequency decays.

The key results presented in this paper are summarised in Table 2.6.

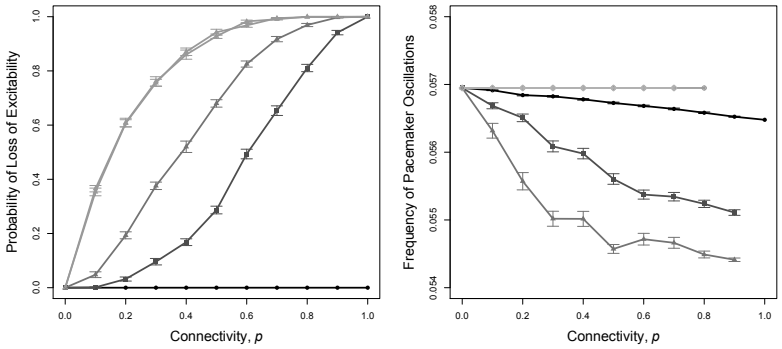

(a) **(b)**

Figure 2.18: (a) Probability that the pacemaker cell becomes inactivated versus connectivity, for a selection of coupling strengths. All points show the number of times excitation was not maintained in 50 simulations as mean ± SEM of 15 repetitions. Lattice size is 25×25. Lines represent coupling strengths of 0.1, 0.5, 1, 5 and 10 on a graded scale from dark to light. Coupling strengths of 5 and 10 are shown in the same shade due to their close proximity. (b) Frequency of oscillations of the pacemaker cell versus connectivity, for a selection of coupling strengths. All points show mean ± SEM of 100 simulations where excitability of the pacemaker cell was maintained, for a lattice size of 25×25. Lines represent coupling strengths of 0.1, 0.5, 1, 5 and 10 on a graded scale from dark to light. The gaps in the individual lines illustrate where the pacemaker cannot maintain excitability.

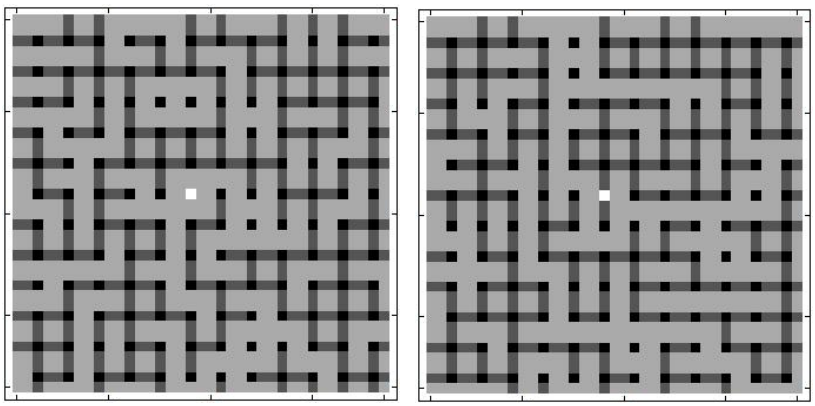

(a) **(b)**

Figure 2.19: The topology of the central 12×12 cells of pacemaker cell networks (truncated from the 25×25 network for clarity). The pacemaker cell is illustrated in white, all other cells are shown in black. The connections between cells are shown on a graded scale from light to dark grey with increasing connection. The coupling strength $\kappa = 5$ and the probability of connection is 0.6. (a) A sample network that results in the pacemaker cell having a finite frequency. The pacemaker cell is isolated in the network. (b) A sample network in which the frequency of the pacemaker cell decays. The pacemaker cell is well-connected to its neighbours.

Table 2.6: Summary of the models used.

Type of Network	Coupling	Method of Generation	Key Results
Homogeneous lattice	Symmetrical	Fixed coupling κ	Minimum and maximum coupling for each perturbation in which global excitation is possible.
Bernoulli lattice	Symmetrical	Fixed coupling κ with varying probability p.	Even when global excitation cannot occur in the fully connected lattice, it can be attained in a partially connected system.
Uniformly distributed	Symmetrical	Couplings drawn from a uniform distribution on $[0.5, 10]$ with varying probability p.	Total coupling between neighbouring cells has a minimum and maximum threshold for global excitation. Between these values (and with constant total coupling), the ability to achieve global excitation is dependent on the standard deviation of coupling values.
Cell capacitance	Asymmetrical	Coupling $\kappa = RC^{-1}$. C is drawn from distribution of cell capacitance taken from experimental data. R is fixed. Probability p is varied.	The presence of spatial heterogeneity is essential for global excitation at comparable perturbation values to the Bernoulli lattice. A larger perturbation is needed for full excitation and full connectivity. There is no discernible difference between day 15 and day 18 gestation.
Resting membrane potential	Symmetrical	Fixed coupling κ. Each cell has its own parameters and so its own resting membrane potential.	Increase in gestational age results in a smaller excitation threshold for each cell to overcome. Systems with resting membrane potential variation only fail to achieve global excitation.
Cell capacitance and resting membrane potential combined	Asymmetrical	Each cell has its own resting membrane potential. C is drawn from distribution of cell capacitance. R is fixed.	Both forms of variation allows global excitation in heterogeneous systems. A larger perturbation is needed than in the Bernouill lattice to achieve global excitation at full connectivity.
Pacemaker cells	Symmetrical	Central cell is a pacemaker. All other cells as before. Fixed coupling κ with varying probability p.	Highly connected systems have a greater probability of the pacemaker cell ceasing to be active. The frequency of oscillation of the pacemaker cell decreases with increasing connectivity. At high coupling strength values, connectivity has no effect on the frequency — the only way for a pacemaker to retain a finite frequency is to be isolated.

2.5 Discussion

It is well known that an increase in the number of gap junctions in myometrial tissue is indicative of the onset of labour (Garfield *et al.*, 1977). While the number of connections increases, little is known about the strength and local structure of these connections. The main finding of this study is that heterogeneity of the coupling structure of a network of excitable elements allows the system to respond in a graded manner to a wide range of stimuli. For instance, reduced connectivity results in a gradual increase in cluster size in response to stimulation, resulting in a smooth transition between an unexcited and globally excited state, which enhances the scope for precise regulation. Physiological evidence suggests that the transition from quiescence to excitation is gradual (Garfield & Maner, 2007); this may be explained in part by the results presented here.

Relatively little is known about the effect of heterogeneity in myocyte connections on the excitability of the network as pregnancy progresses. Our analysis of the pregnant mouse data confirms the importance of heterogeneity and demonstrates that the network evolves towards global excitability as labour approaches.

A homogeneous lattice (fully connected with identical couplings) cannot achieve global excitation when the coupling is too strong: neighbouring cells can too readily absorb the membrane charge associated with the stimulus. When heterogeneity is introduced, whether by removing selected couplings at random or by varying the coupling values at random, the ability to achieve global excitation is restored. An intuitive explanation is that heterogeneity creates local "pockets" of excitability where the initially stimulated cell is less hampered by the charge drain imposed by its neighbours. Moreover, heterogeneity smoothes out the sudden transition between an unexcited network and a globally excited one (Section 2.4.3). This is consistent with the finding that in the days and hours leading up to labour, contractions spread further throughout the uterus (Miller *et al.*, 1989).

Finally, spatial heterogeneity regulates the ability of pacemaker cells to drive the network, again in a graded fashion.

Simulations on a fully connected square lattice (Section 2.4.1) indicate that there exist minimum and maximum coupling values between which global excitation of the network is possible. These thresholds were found to be dependent on the initial perturbation. Whereas the homogenous lattice cannot exhibit global excitation, the heterogeneous lattice formed by removing couplings is able to exhibit excitation. In the heterogeneous system, the wave of excitation generated by the central cell has to overcome a lower threshold to excite neighbouring cells. Therefore, the system can achieve global excitation even with a smaller inciting stimulus.

Investigation of the variability of the couplings surrounding the excited cell in a lattice with couplings drawn from a uniform distribution indicates that global excitation is affected by the variance of the coupling strengths to neighbouring cells, and is not solely dependent upon total coupling. The effect of coupling variance displayed a lower and upper threshold for global excitation of the network. Therefore a variance within these bounds is optimal for network excitation. Outside this region, excitability does not spread across the whole network. It appears that when the variance of connections is too high, a fragmented network results, which does not allow for propagation of excitability. Overall, it appears that variation of coupling allows for a larger cluster size at high connectivity. This result was supported by similar simulations run for an anisotropic lattice (Table 2.4) where the horizontal and vertical coupling strengths were drawn from distinct uniform distributions.

The importance of heterogeneity was demonstrated by the correlation between cells at increasing distance from the central cell, and the central cell itself. At full connectivity, there was no discernible difference in correlation. For networks with a lower probability of connection, a much larger correlation was observed in networks with fewer than 10 %

of cells becoming excited when compared with networks with more than 90 % of cells becoming excited. This effect was more pronounced in lower connectivities, reaffirming the importance of heterogeneity. This supports the notion of excitation pockets, where a cluster of cells that are too well-connected act as a current sink and prevent the excitation from spreading further through the network. The main determinant of global excitation is the local spatial correlation around the excited cell.

Data for resting membrane potential in mice at 15-day and 18-day gestational age indicate an increase in depolarisation of the cell membrane with increased gestation length, confirming the findings of Lodge & Sproat (1981). The statistical variation in resting membrane potential among cells also increases with gestational age. With resting membrane potential as the only form of variability in the model, full excitation could not be reached. However, when resting membrane potential variability is combined with capacitance variation, the optimum excitability at intermediate connectivity is restored.

Results were consistent over a range of lattice sizes; from 9×9 to 25×25. Larger lattices were not investigated due to computational restrictions. Simulations were also run for hexagonal lattices to investigate effects of network structure on excitability. Similar qualitative results were obtained. However, the hexagonal lattice displayed a wider window of global excitability as compared to a square lattice with the same number of nodes. An increase in spatial heterogeneity enables the system to achieve global excitation more easily. Networks with stochastically varying node degrees will be investigated in future research.

The resting membrane potential values were taken from recordings of isolated myometrial cells. However, a system of connected cells settles into a different resting states. To verify that the experimental data were representative of networked cells, simulations were run in which the cells where allowed to equilibrate, and differences were found to be negligible.

Preliminary observational data (shown in Appendix 2.7 and Figure 2.20) suggest that an increase in heterogeneity increases the frequency of the oscillations of the pacemaker. This was confirmed by our simulations in which the pacemaker cell's ability to drive the system is modulated by connectivity. With increased heterogeneity, the drain of current to surrounding cells has a smaller effect, causing the frequency of oscillations to increase. In addition, a well connected system makes it more likely that the pacemaker is not able to remain active, and its oscillations stop altogether. Maximal excitability is associated with a moderate degree of spatial heterogeneity. This would suggest that a way in which a cell can develop pacemaker activity is to down-regulate its gap junctions to partially isolate itself in the network. The suggestion of cell isolation is supported by preliminary experimental data (not shown) in which individual cells can oscillate but still participate in a global action potential.

Propagation waves in excitable media have been examined extensively using cellular automata (Markus & Hess, 1990; Gerhardt *et al.*, 1990a,b,c, 1991). This approach was then extended to show how the cellular automata models could be matched to systems such as the FitzHugh-Nagumo set of equations (Weimar *et al.*, 1992a,b). A cellular automata model also exists which describes the uterine network using Hodgkin-Huxley physiology (Barclay *et al.*, 2010). Here we have opted to use the FitzHugh-Nagumo model to represent the excitation and recovery of a myometrial cell. Since the primary aim of the present study was to explore the consequences of spatial heterogeneity *per se*, we have used a two-dimensional minimal model to represent the excitable element without being too computationally expensive. This FitzHugh-Nagumo model captures the qualitative dynamics of propagation through excitable systems. It does, however, still have its limitations. The model considers only one activation variable and one recovery variable. The minimal model can be replaced by models that take into account individual currents and the intracellular calcium stores (Rihana *et al.*, 2008; Laforet *et al.*, 2011; Rosa *et al.*, 2012). Future work will focus on these more detailed models to more accurately represent the

calcium influx resulting in a contraction. In addition, a three-dimensional system will be considered to model the uterine network more closely.

Miyoshi *et al.* (1996) demonstrated that gap junctional conductance between coupled cells is dependent on the trans-junctional voltage, which adds a non-linear effect that may play an important role in the transition from the globally quiescent state to the globally excitable state. This effect has not been taken into account in the present study and will be the subject of future research.

In summary, the mathematical model used here indicates that spatial heterogeneity may serve as an important modulator of excitability in uterine muscle. Spatial heterogeneity of cell-to-cell connections promotes an increase in the excitability of the network, and the ability of a network to become fully excited is governed predominantly by the local connection structure. In addition, heterogeneity in both cell capacitance and resting membrane potential also play a role. Similarly, heterogeneity allows a pacemaker cell to drive the system.

Shifts in this heterogeneity may be a significant factor in the regulation of myometrial excitability as pregnancy progresses from conception to parturition. Preterm labour may be associated with a premature development of spatial heterogeneity. Mapping of spatial heterogeneity may prove to be a diagnostic tool to monitor the development of excitability throughout pregnancy.

2.6 Acknowledgements

RES gratefully acknowledges funding for a studentship from the Engineering and Physical Sciences Research Council through the MOAC Doctoral Training Centre at the University of Warwick.

2.7 Appendix: Preliminary observational data — an increase in heterogeneity increases the frequency of the oscillations of the pacemaker

2.7.1 Methods

2.7.1.1 Slice Preparation

Myometrial biopsies were taken from patients (gestation 38 – 40 weeks, not in labour) undergoing caesarean section due to presumed fœtal distress. Informed written consent and approval from the Local Ethics Committee (REC-05/Q2802/107) were obtained prior to sample collection. Macroscopic myometrial samples were dissected under a light microscope using a scalpel blade into a piece of approximately $1\times0.5\times0.3\,\mathrm{cm}$ displaying well-defined layers running along the longitudinal axis of the strip. The strip was then ligatured with braided suture at each extremity before being stretched and fixed to the base of a metallic tissue holder using cyanoacrylate glue. Slices $200\,\mu\mathrm{m}$ thick were cut using a vibroslicer (Integraslice 7550 PSDS, Campden Instruments, UK) in oxygenated (4 °C) KREBS TES solution (in mM: NaCl, 133; KCl, 4.7; $MgSO_4$, 1.2; KH_2PO_4, 1.2; glucose, 11.1; TES, 10; $CaCl_2$, 2.5; pH:7.4). Slicing was performed with a razor blade, cut to a convenient size, at an oscillating speed of 86 Hz with lateral amplitude of 1 mm and an advance speed of $0.10\,\mathrm{mm\,s^{-1}}$ – $0.20\,\mathrm{mm\,s^{-1}}$. First cuts and the glued base of the strip were discarded. Each slice was then separated by cutting the extremity of the slice using fine dissecting scissors before incubation for 1 hour at room temperature in KREBS TES solution for equilibration and recovery. Slices were then used immediately.

2.7.1.2 Confocal Imaging of $[Ca^{2+}]_i$

Myometrial slices were incubated for 30 minutes at 37 °C in Krebs solution containing 13 μM Fluo-4/AM (Invitrogen, UK). Dye loading was aided by inclusion of non-ionic detergent Pluronic F127 (0.025 %, w/v). Loaded slices were placed in a glass-bottomed Petri dish and weighted down with a 250 mg slice grid (HSG-5, ALA Scientific, USA). The dish was secured on the stage of an inverted microscope (Aiovert 200M) equipped with an LSM 510 META confocal scanner (Carl Zeiss, UK). The strips were superfused with pre-warmed (35 °C) Krebs solution at a flow rate of 2 ml min^{-1} for 30 – 40 minutes until stable spontaneous contractions developed. If a slice did not develop spontaneous activity in this time, it was discarded.

The slices were scanned with a 488 nm wavelength laser beam focused into a diffraction-limited spot via a Flua 5x/0.24NA objective lens. Fluorescence was recorded through a band-pass filter (505 – 530 nm) using a photomultiplier tube with a pinhole in the light path. The pinhole diameter was 2 Airy units in order to reject most out-of-focus fluorescence and to maximise the throughput of light originating from the focal plane. The excitation and emission beams were separated by a dichromatic mirror centred at 495 nm. Images were taken for a frame size of 512×256 pixels at a frame rate of 2 frames per second in unidirectional scan and 4 frames per second in bidirectional scan. Image acquisition was controlled by Zeiss LSM v4.0 software. Time series of up to 8000 frames were acquired.

2.7.2 Results

In the presence of the gap junction inhibitor carbenoxolone the frequency of activity increases and the duration of an individual action potential decreases, as indicated in Figure 2.20.

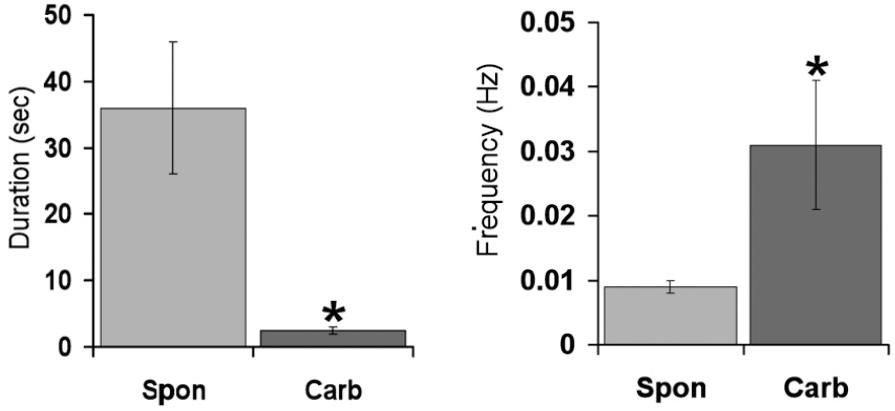

Figure 2.20: Effect of carbenoxolone on $[Ca^{2+}]_i$ transients in bundles. Event duration and frequency in the absence (Spon) and presence (Carb) of carbenoxolone. Values represent mean ± SEM; an asterisk ($*$) indicates significance at the $p = 0.05$ level (Student's t-test); $n = 8$.

Chapter 3

Alterations in gap junction connexin-43/connexin-45 ratio mediate a transition from quiescence to excitation in a mathematical model of the myometrium

In this chapter, the mathematical model of the myometrium developed in Chapter 2 is extended to take into account the voltage dependence of gap junctions observed by Miyoshi *et al.* (1996). The two, distinct gap-junctional conductance relationships observed corresponded to systems with predominantly connexin-43 (Cx43) and connexin-45 (Cx45) proteins composing the gap junctions. In our models, we stochastically allocate a Cx43 or Cx45 gap junction with a particular probability to each inter-cell connection. The ratio of Cx43/Cx45 proteins is then altered in order to examine the effect of different proportions of the two connexins. We observe that a higher proportion of Cx43 to Cx45 is needed in

order to excite the network effectively. Combining these findings with RNA data from rat and human tissue, we propose that the role of Cx45 in the uterus is to halt contractions until the time is right to deliver the baby.

I was responsible for devising the mathematical models, running the simulations, and writing the manuscript. Chipo Mashayamombe performed the RNA-seq experiments on rat myometrium samples provided by Dr Shi and Prof. Robert E. Garfield from St. Joseph's Hospital and Medical Center in Phoenix, Arizona.

Alterations in gap junction connexin-43/connexin-45 ratio mediate a transition from quiescence to excitation in a mathematical model of the myometrium

Rachel E. Sheldon[1,3], Chipo Mashayamombe[2,3], Shao-Qing Shi[4], Robert E. Garfield[4], Anatoly Shmygol[3], Andrew M. Blanks[3], and Hugo A. van den Berg[1]

[1] MOAC Doctoral Training Centre, University of Warwick

[2] Systems Biology Doctoral Training Centre, University of Warwick

[3] Division of Reproductive Health, Warwick Medical School

[4] Department of Obstetrics & Gynecology, St. Joseph's Hospital & Medical Center, Phoenix, AZ

J. R. Soc. Interface, 2014

3.1 Abstract

The smooth muscle cells of the uterus contract in unison during delivery. These cells achieve coordinated activity via electrical connections called gap junctions, which consist of aggregated connexin proteins such as connexin-43 and connexin-45. The density of gap junctions governs the excitability of the myometrium (among other factors). An increase in gap junction density occurs immediately prior to parturition. We extend a mathematical model of the myometrium by incorporating the voltage-dependence of gap junctions that has been demonstrated in the experimental literature. Two functional subtypes exist, corresponding to systems with predominantly connexin-43 and predominantly connexin-45, respectively. Our simulation results indicate that the gap junction protein connexin-45 acts as a negative modulator of uterine excitability, and hence, activity. A network with a higher proportion of connexin-45 relative to connexin-43 is unable to excite every cell. Connexin-45 has much more rapid gating kinetics than connexin-43 which we show limits

the maximum duration of a local burst of activity. We propose that this effect regulates the degree of synchronous excitation attained during a contraction. Our results support the hypothesis that as labour approaches, connexin-45 is down-regulated to allow action potentials to spread more readily through the myometrium.

3.2 Introduction

The myometrium, which makes up the bulk of the uterine wall in all species (Putz & Pabst, 1989) (Figures 3.1a and 3.1b), is composed of interconnected smooth muscle cells, which form an excitable medium (Garfield *et al.*, 1977), *i.e.* a medium that is capable of propagating signals over relatively long distances with virtually no damping. In the myometrium, these propagating signals take the form of action potentials which trigger phasic contractions during labour (Parkington *et al.*, 1999b). These involve the rhythmic contraction and relaxation of the smooth muscle cells, giving rise to synchronised travelling waves throughout the uterus (Singh *et al.*, 2012). In humans the phasic contractions typically last for around a minute (Maeda, 2013), whereas in rats they last for approximately 68 seconds at term (Buhimschi *et al.*, 1998).

Throughout most of pregnancy, the myometrium remains quiescent, allowing the fœtus to develop undisturbed (Challis *et al.*, 2000). The myometrium undergoes major changes in the days leading up to labour (Challis *et al.*, 2000). In particular, as parturition approaches, the uterus becomes more excitable through an activation phase which involves molecular changes that lead to a decrease in time between subsequent contractions (Parkington *et al.*, 1999a). In humans, this interval decreases from approximately 30 minutes to approximately 2 minutes as pregnancy progresses (Parkington *et al.*, 1999a; Maeda, 2013), whereas in rats contractions occur at 2.3-minute intervals at gestational day 19 and at 46-second intervals in active labour (Buhimschi *et al.*, 1998).

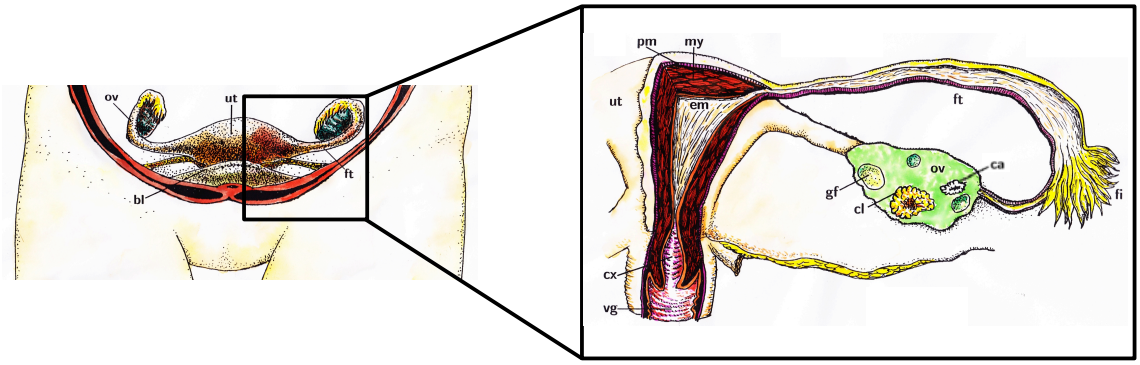

(a)

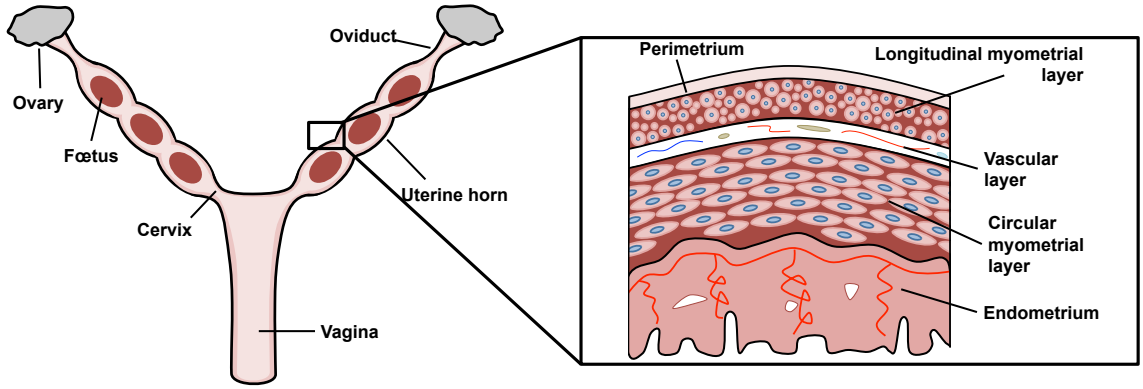

(b)

Figure 3.1: (a) Anatomy of the human female reproductive system. Left: location in the lower abdomen; Right: partially dissected uterus showing the layers of the uterine wall and the Fallopian tube. The following structures are indicated: **ut**: uterus; **ov**: ovary; **ft**: Fallopian tube; **bl**: bladder; **pm**: perimetrium; **my**: myometrium; **em**: endometrium; **gf**: Graafian follicle; **cl**: corpus luteum; **ca**: corpus albicans; **cx**: cervix; **vg**: vagina; (b) Anatomy of the rat reproductive system. Left: The rat uterus is divided into two horns. Fœtuses implant in the wall of each horn. Right: Cross-section of the uterine wall showing the outer perimetrium; the external, longitudinal myometrial layer; the vascular layer; the inner, circular myometrial layer; and the endometrium.

A key condition for the transition to excitability at the whole-organ level is a change in connectivity between the myometrial smooth muscle cells (Garfield *et al.*, 1977). The smooth muscle cells in the myometrium are connected through a series of intercellular channels that allow the passage of ions and small molecules from one cell to another, each channel being made up of two components, one contributed by each cell (Kumar & Gilula, 1996).

As pregnancy progresses, the density of gap junctions on the cell-to-cell contact surfaces increases, which is thought to be one of many factors which instigate labour (Garfield *et al.*, 1977). In the non-pregnant uterus of both rats and humans, gap junctions are either absent or present at low density (Garfield *et al.*, 1977, 1978; Risek *et al.*, 1990). At the time of delivery, gap junctions are present at a density of approximately 1000 per cell in human tissue (Garfield *et al.*, 1988).

The ability of a myometrial network to achieve global excitation is strongly dependent on spatial heterogeneity of cell-to-cell connectivity (Sheldon *et al.*, 2013). Using a mathematical model of the myometrium based on FitzHugh-Nagumo dynamics (FitzHugh, 1961; Nagumo *et al.*, 1962), we previously showed that a moderate degree of spatial heterogeneity allows excitation to spread throughout a network even if the same network would be quiescent when fully and uniformly connected. However, the coupling between cells was represented as a passive resistor, whereas in reality voltage-dependent gating is a well-established property of vertebrate gap junction channels (Spray *et al.*, 1979, 1981; Harris *et al.*, 1981; Wang *et al.*, 1992). This transjunctional voltage-dependence is directly related to the connexin composition of the channel. Individual connexins exhibit different responses as a function of the potential difference between neighbouring cells; for example, connexin-43 (Cx43) is relatively insensitive to the voltage difference, displaying only modest changes in conductance as the transjunctional voltage is altered (Veenstra *et al.*, 1992). By contrast, connexin-45 (Cx45) and connexin-40 are highly sensitive to transjunctional voltage differences (Veenstra *et al.*, 1992, 1994; Beblo *et al.*, 1995). The differences

in connexin protein response to transjunctional voltage are thought to be underpinned by different localisations of charged residues along the inner lining of the ion-conducting pore as well as different phosphorylation states (Verselis *et al.*, 1994; Moreno *et al.*, 1992).

Miyoshi *et al.* (1996) recorded gap-junctional currents between isolated pairs of rat myometrial cells, using the double-whole-cell voltage-clamp configuration (Figure 3.2). The cell pairs were found to exhibit one of two distinct relationships between conductance and voltage-dependence which occurred in equal proportions (Figure 3.4a). The so-called 'Type I' channels displayed a gradual increase from a normalised conductance of 0.35 to 1 with decreasing voltage difference. At small transjunctional voltages, there was very little change in conductance. By contrast, the 'Type II' channels showed a much sharper increase in conductance with decreasing voltage difference. A notable voltage-dependent change in conductance was observed even at small transjunctional voltages. The authors observed that the Type I voltage-dependence relationship fit with the pattern expected

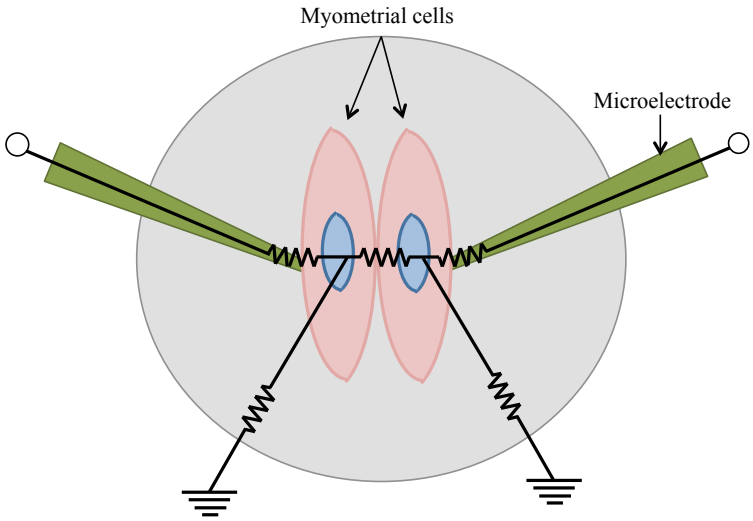

Figure 3.2: The two-microelectrode double patch-clamp set-up used by Miyoshi *et al.* (1996) to measure the conductance across a gap junction. Two electrotonically coupled cells have been isolated and each has been patched by a microelectrode. The equivalent circuit is indicated: the resistor between the cells represents the gap junction, the resistors between the microelectrodes and cells are the electrode resistances, and the remaining resistors are the membrane (leak) conductances.

for a tissue with predominantly Cx43 junction proteins. In addition, the Type II junction voltage-dependence appeared to be noticeably distinct from the connexin patterns observed before. The dependence of conductance on the transjunctional voltage difference for Type II is more consistent with a Cx45 junction protein, a hypothesis that was further supported by the findings by Moreno *et al.* (1995).

Here we investigate how the spread of excitation through a network is affected by incorporating voltage-dependent cell-to-cell couplings in the mathematical model. We adapt the voltage-dependent conductance relationships for both gap junction types identified by Miyoshi *et al.* (1996). The main qualitative effect is that conductance increases as the potential difference between the cells decreases. To isolate this "cut-off" effect, we initially model the voltage-dependence relationship as a simple step function. We subsequently compare our findings with more realistic voltage-conductance relationships in order to verify that the dominant qualitative effect is the "cut-off" point of activity.

Finally, we incorporate gating kinetics. We propose that the Type II gap junctions are not able to excite the network by themselves; a substantial proportion of Type I gap junctions is needed to spread activity effectively. The gating kinetics is much more rapid for Type II gap junctions in comparison with Type I junctions. The faster kinetics prevents the longer depolarisation propagating throughout the network, and so limits the excitability of the network. Accordingly, we suggest that relative proportion of Type I and Type II gap junctions is crucial for the modulation of activity in the excitable myometrial network.

Analysis of gene expression in rat models suggest that the expression of Cx45 is down-regulated in labour. We do not observe a change in the expression of Cx43 in the transition from pregnancy to labour. We therefore hypothesise that the relative proportion of Cx43 and Cx45 is crucial; Cx45 acts as a brake on activity in the uterus, and its down-regulation may be an important step in the initiation of labour.

3.3 Methods

3.3.1 Mathematical modelling

We further develop a mathematical model of the myometrial smooth muscle network (Sheldon *et al.*, 2013). The network is constructed as a square lattice in which each node is connected to four others. Each simulated cell obeys FitzHugh-Nagumo dynamics. The FitzHugh-Nagumo model is a two-variable system which describes the excitation and relaxation of an excitable cell (Keener & Sneyd, 2004). The model is an example of an excitation-relaxation oscillator due to its threshold properties in which a sufficiently large input of current is required for the cell to exhibit an excursion corresponding to excitation and relaxation. However, parameters can be chosen such that cells are autorhythmic (Sheldon *et al.*, 2013), that is, the cells continually oscillate through the excitation-relaxation cycle without any external stimulus. FitzHugh-Nagumo is a simplification of the Hodgkin-Huxley model for spiking neurons (Hodgkin *et al.*, 1952; Hodgkin & Huxley, 1952d) and, as such, is often used in modelling excitable systems such as contractions of cardiac myocytes (Zhang & Holden, 1995; Aliev & Panfilov, 1996; Benson *et al.*, 2006).

Each node in the network is considered to be excitation-relaxation oscillator with a fast ("excitation") state variable v that corresponds to the transmembrane potential and a slow ("recovery") variable w that corresponds to gating kinetics which repolarise the excited cell. The following dimensionless ordinary differential equations describe this two-variable model:

$$\frac{d}{dt}v(t) = \frac{1}{\epsilon}(Bv(t)\,(1-v(t))(v(t)-\alpha) - w(t) - w_0) + I\ , \tag{3.1a}$$

$$\frac{d}{dt}w(t) = v(t) - \gamma w(t) - v_0\ , \tag{3.1b}$$

where I is the input current and B, α, γ, w_0, v_0, and ϵ are positive parameters. The

values shown in Table 3.1 are used in all simulations to generate a network of cells which require a suprathreshold current input to undergo an oscillation.

Table 3.1: Parameter values used in Equations 3.1a and 3.1b in all simulations.

Parameter	B	α	γ	w_0	v_0	ϵ
Value	3	3	0.05	0.4	0.4	0.2

The equations were solved using an LSODE (Livermore Solver for Ordinary Differential Equations) approach through the NDSolve function in *Mathematica*. Results were numerically stable under variation in step size.

Each simulated cell is coupled to its four neighbours through resistors representing gap junctions (Figure 3.3a). A coupling constant K is assigned to each gap junction and defined as $K_{ij} = (C_i R_{ij})^{-1}$, where i and j are two neighbouring cells, C_i is the capacitance of cell i, and R_{ij} is the resistance between the two cells. The coupling K is therefore a rate constant, and is rendered dimensionless as follows. The FitzHugh-Nagumo model defines dimensionless time, t, as $t = R_1\tau/D$, where D is a damping coefficient that captures the inertia of the system due to the gating kinetics, as shown by FitzHugh (1961), τ is dimensional time, and R_1 is the passive resistance of the nonlinear current device, represented as a tunnel diode by Nagumo *et al.* (1962). Accordingly, dimensionless coupling is defined as DK/R_1 and denoted κ. The scaling of the remaining parameters is detailed in Section 1.10.2 and follows the derivation given by Keener & Sneyd (2004).

Miyoshi *et al.* (1996) identified two distinct relationships between the conductance of smooth muscle gap junctions and the voltage difference between two neighbouring myocytes (Figure 3.4a). We adapt these relationships to represent voltage-dependent gap junctions in terms of the coupling strength κ. Spatial heterogeneity is added to the system by introducing a probability p of a connection existing between any two adjacent cells, as previously described (Sheldon *et al.*, 2013). This parameter is referred to as the 'connectivity' of the network. The relative cluster size serves as a measure of the proportion of cells in the network that become excited: if all cells are excited, the relative cluster size

equals 1, whereas if no cells become excited, it is 0.

3.3.1.1 Step function model

The simplest way to represent the voltage-dependence is by means of a step function (Figure 3.4b). For cells with a small voltage difference, the normalised gap-junctional conductance is set to be 1 whereas for cells with a large voltage difference, the normalised gap-junctional conductance is 0.2 (the base value determined by Miyoshi *et al.* (1996)). We use the term *gap-junctional conductance bandwidth* to mean the range of voltage differences for which the gap-junctional conductance equals 1. The voltage differences are scaled from unit-bearing values to the dimensionless FitzHugh-Nagumo model values. To facilitate numerical analysis, the step function is smoothed, as follows (Figures 3.5a

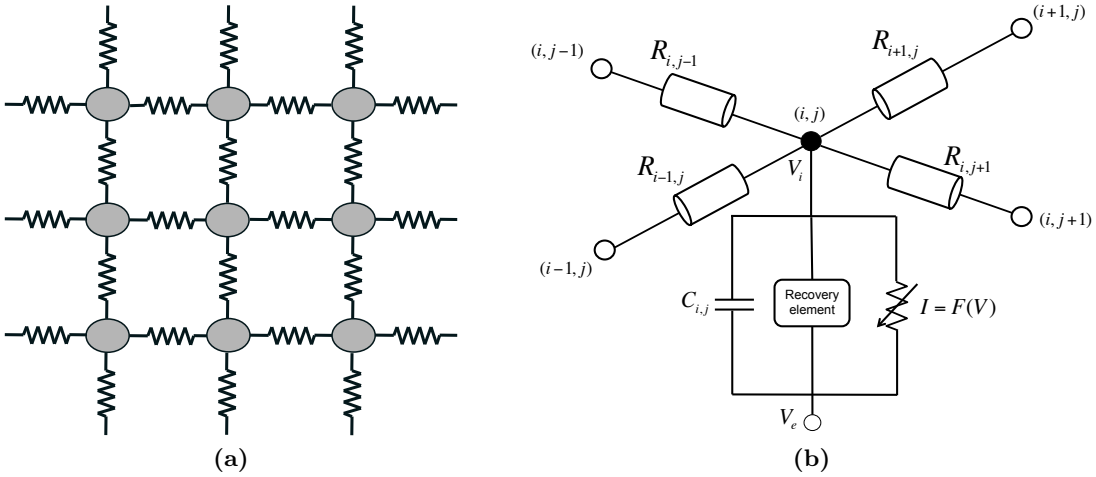

Figure 3.3: (a) Diagram of the model network. Each cell is represented by a circular node, and is connected to its four neighbours through resistors representing the gap junctions; (b) Electrical circuit diagram representing the current flow between connected cells. Cell (i, j) is the cell of interest, coupled to four surrounding cells; R represents the resistances in gap junctions. The circuit at cell (i, j) represents a basic model of an excitable system (Keener & Sneyd, 2004). V_e represents the external potential; V_i represents the internal potential; $C_{i,j}$ is the cell capacitance; the recovery element represents the recovery current; and the non-linear current-voltage device (I) represents the fast current.

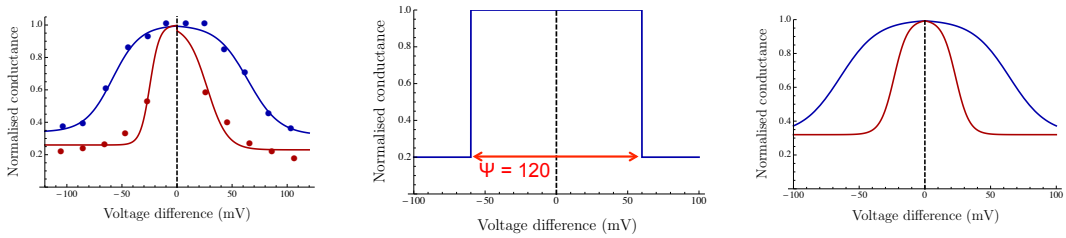

Figure 3.4: (a) Relationship between conductance and voltage difference between neighbouring cells as published by (Miyoshi *et al.*, 1996). The blue line shows the Type I gap junction relationship identified; the red line shows the Type II gap junction relationship identified. Points show experimental conductances determined by Miyoshi *et al.* (1996). The lines represent Boltzmann curve fits to the data (Equation 3.3); (b) Step function describing the relationship between voltage difference and gap-junctional conductance. A value $\psi = 120$ corresponds to a conductance of 1 over a voltage difference of $\pm 60\,\text{mV}$; (c) Symmetrical curves for the Type I relationship (blue) and the Type II relationship (red) identified by Miyoshi *et al.* (1996). Type II is determined from Type I by a change in the parameter ψ in Equation (3.4).

and 3.5b):

$$\text{Relative conductance} = 0.6 + \frac{0.4 \times (\psi/2 - |((v_i(t) - v_j(t)) \times \lambda)|)}{\sqrt{1 + (\psi/2 - |((v_i(t) - v_j(t)) \times \lambda)|)^2}}, \tag{3.2}$$

where the indices i and j represent adjacent cells, λ is the scaling required to convert between physiological values and the FitzHugh-Nagumo model values, and ψ is the gap-junctional conductance bandwidth. The relative conductance is multiplied by the coupling strength κ. In the majority of simulations, $\kappa = 1$; however, we also present some results with $\kappa = 0.76$ to facilitate comparison with previous results in which we demonstrated the importance of heterogeneity (Sheldon *et al.*, 2013).

Scaling is based on a typical rat myometrial cell in accordance with Miyoshi *et al.* (1996). The membrane potential of a rat myometrial cell increases from $-45\,\text{mV}$ to $+10\,\text{mV}$ during the upstroke of a full action potential, corresponding to an excursion of $55\,\text{mV}$. In the non-dimensionalised model, the size of the excursion is 3.52278. Accordingly, λ is taken to be 55/3.52278. To vary the width of the gap-junctional conductance band ψ is selected from

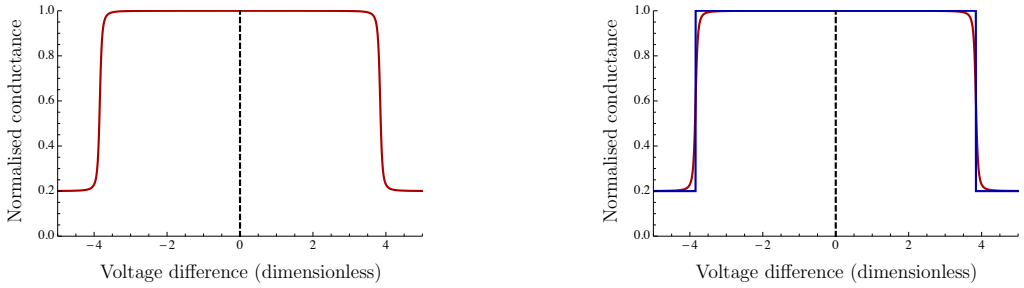

(a) **(b)**

Figure 3.5: (a) Step function describing the relationship between voltage difference and gap-junctional conductance approximated by the sigmoidal equation given in Equation 3.2; (b) Step function (blue) overlayed with the approximated sigmoidal function (red).

the range 40 mV to 200 mV (twice the difference to zero, which lies at the midpoint). The value of ψ then dictates the voltage difference values over which the conductance of the gap junction equals 1. For example, $\psi = 120\,\text{mV}$ sets the conductance to 1 over a voltage difference of $\pm 60\,\text{mV}$, as illustrated in Figure 3.4b.

To check the model against our previous findings, the bandwidth is set to a sufficiently high value such that the relative conductance remains 1 over the entire voltage range of the action potential. The proportion of cells that become excited as a function of connectivity p reproduce our previous results; see Figure 3.6a for more details. With a coupling strength $\kappa = 0.76$, we replicate our previous scenarios in which spatial heterogeneity proved to be crucial in exciting the network (Figure 3.6b).

3.3.1.2 Symmetrical Miyoshi model

Miyoshi *et al.* (1996) proposed the following empirical equation for the conductance-voltage relationship:

$$g(V_j) = \frac{(1 - G_{\min})}{1 + \exp\{-A(V_j - V_h)\}} + G_{\min}, \tag{3.3}$$

where g is the normalised conductance of the gap junction, V_j is the voltage difference

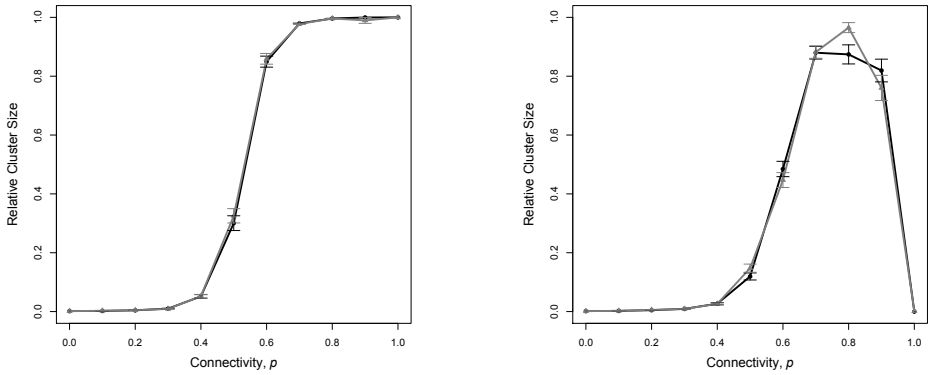

(a) **(b)**

Figure 3.6: Comparison of the infinite width step function model with the uniformly coupled Bernoulli model. Infinite width step function model is shown in black, whereas the uniformly coupled Bernoulli model previously published (Sheldon *et al.*, 2013) with (a) $\kappa = 1$ and; (b) $\kappa = 0.76$ is shown in grey. Points show mean ± SEM of 100 simulations for a 25 × 25 lattice, with an initial perturbation of 1.

across the gap junction, $G_{\min}$ is the minimum value of the conductance, V_h is the half inactivation voltage (mV) at which the conductance is reduced by $(1 - G_{\min})/2$, and A is a slope factor ($(\text{mV})^{-1}$). The authors identified two distinct types of voltage-dependent gap junctions with the parameters given in Table 3.2. The relationship between the voltage gradient and gap-junctional conductance is shown for both types in Figure 3.4a.

Table 3.2: Parameter values for Equation 3.3.

	Negative V_j			Positive V_j		
	$G^-_{\min}$	V^-_h (mV)	A^- (mV^{-1})	$G^+_{\min}$	V^+_h (mV)	A^+ (mV^{-1})
Type I	0.34	-58.5	0.08	0.32	64.4	-0.07
Type II	0.26	-24.6	0.23	0.23	27.3	-0.11

To investigate the effect of the width of the gap-junctional conductance band, we model the Type I relationship by means of the bandwidth parameter ψ that allows us to scale the Type I relationship to resemble the Type II relationship. We employ a symmetrical version by taking the absolute value of the voltage and using the positive values that Miyoshi *et al.*

(1996) obtained for the Boltzmann fit, as shown in the following equation:

$$g(V_j) = \frac{(1 - G^+_{\min})}{1 + \exp\left\{-A^+(|V_j \times \lambda \times 110/\psi| - V^+_h)\right\}} + G^+_{\min}, \tag{3.4}$$

where λ is the scaling required to convert between physiological values and FitzHugh-Nagumo values; and ψ is the required width of the gap-junctional conductance band. For instance, $\psi = 110\,\text{mV}$ will give Type I, and $\psi = 40\,\text{mV}$ will give Type II. The scaling parameter $\lambda = 55/3.52278$, as before. A pictorial representation of the symmetrical Miyoshi *et al.* (1996) model is shown in Figure 3.4c.

We checked the model against our previous results by setting the bandwidth to a high value in order to attain a relative conductance of 1 over the action potential voltage range (Figure 3.7).

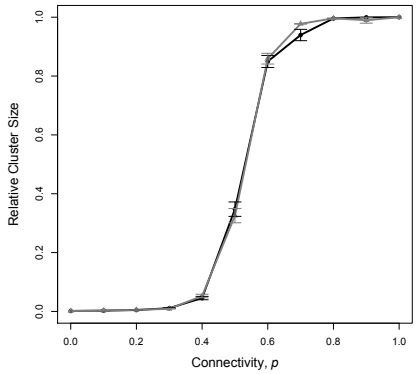

Figure 3.7: Relative cluster size versus connectivity p, comparing the infinite width symmetrical Miyoshi *et al.* (1996) model (shown in black) with the uniformly coupled Bernoulli model previously published (Sheldon *et al.*, 2013) (shown in grey). Points show mean ± SEM of 100 simulations for a 25 × 25 lattice, with an initial perturbation of 1.

3.3.1.3 Symmetrical Miyoshi model with gating kinetics

The dependence of conductance on trans-gap-junctional voltage as described in the previous section is non-dynamic, *i.e.* the gating kinetics is sufficiently rapid to justify a quasi-

instantaneous model. We now turn to more realistic gating kinetics. In the first instance, voltage-dependence of the time constant is ignored, giving rise to the following ordinary differential equation:

$$\frac{d}{dt}g = \frac{1}{\tau_g}(\bar{g}(V_j) - g)\ , \tag{3.5}$$

where g is the conductance of an individual gap junction, τ_g is the gap-junctional time constant, and $\bar{g}$ is the steady-state conductance dependent on the transjunctional voltage V_j as considered in Sections 3.3.1.1 and 3.3.1.2. A complete excitation-relaxation cycle in the FitzHugh-Nagumo model lasts for 18.6849 dimensionless units (the time at which the cell is able to become re-excited) and we assume an action potential burst in the rat lasts for around 30 seconds. Therefore to convert from dimensionless time to seconds, we multiply the dimensionless time by 30/18.6849.

We next consider a model in which the time constant τ_g is dependent on the potential difference between neighbouring cells. The voltage-dependence relationship for the time constants is derived from Miyoshi *et al.* (1996) by considering the gap-junctional current response after 5-second step pulses of voltages in the range ±90 mV (Figures 3.8a and 3.8b, respectively). The Type I and Type II gap junctions exhibit distinct relationships, given in Figure 3.8. An exponential equation is fitted using the least-squares criterion to each current response in order to determine the time constant for each voltage difference. A Gaussian is then fitted using the least-squares criterion to the time constants giving voltage-dependent time constant relationships as follows:

$$\text{Time constant} = a \times e^{-(V_j^2/2b^2)} + c, \tag{3.6}$$

where V_j is the transjunctional voltage, $a = 9.39726$, $b = 23.9757$, and $c = 0.60274$ for Type I, and $a = 9.41999$, $b = 16.799$, and $c = 0.580013$ for Type II (Figure 3.9). We are not able to obtain good estimates of the rate of decay near 0 mV since the time constant here substantially exceeds the duration of the experiment.

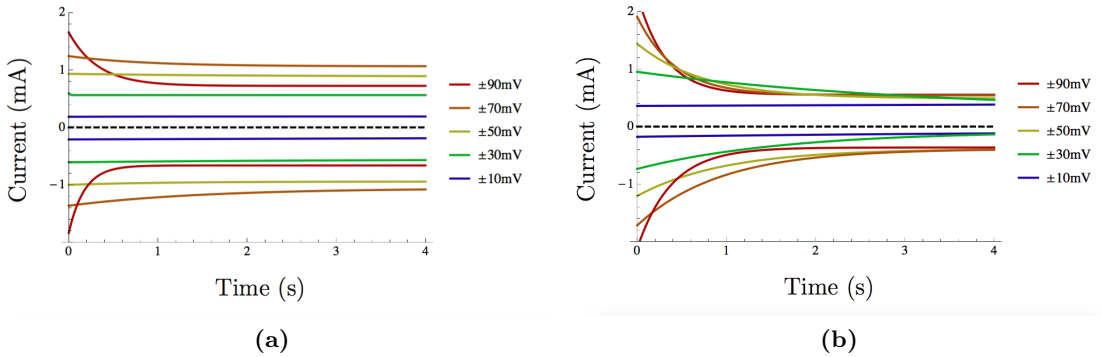

Figure 3.8: Gap junction current responses over time following step pulses of voltages between ± 90 mV. Pulses of ±90 mV are shown in red, ±70 mV in orange, ±50 mV in yellow, ±30 mV in green, and ±10 mV in blue. Lines shown are curve fits to experimental data published by Miyoshi *et al.* (1996). (a) The Type I response; (b) The Type II response.

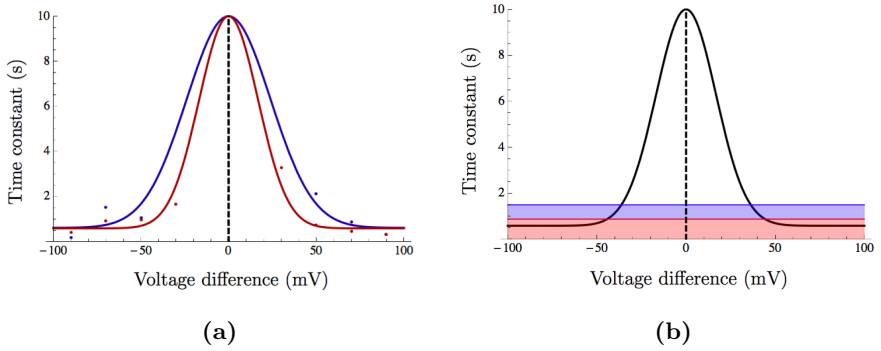

Figure 3.9: (a) The relationships between voltage difference between neighbouring cells and the time constant of the gap junctions. The Type I relationship is shown in red, and the Type II relationship is shown in blue; (b) Comparison of voltage difference between neighbouring cells and the time constant of the gap junction for Type II junctions (as in Figure 3.9). The red shaded region indicates time constants for the Type II junctions in which no excitation is possible. The blue shaded region indicates time constants for the Type II junctions in which spatial heterogeneity is necessary for excitation to take place.

3.3.2 Experimental methods

We employed rat models in order to verify the changes in gene expression as pregnancy progresses. Our main objective was to ascertain whether the expression of Cx43 and Cx45 is consistent with the findings by Miyoshi *et al.* (1996).

3.3.2.1 Rat models

Twelve Sprague-Dawley rats (Harlan Laboratories) were used. Three animals were killed on gestational days $19\,\frac{1}{4}$, 20, and 22, respectively. In the latter case, a further distinction was drawn between animals that had begun labour (and had already delivered one pup) and those that were yet to enter it. Whole-uterine samples consisting of pups, uterine horns, and cervixes were flash frozen in liquid nitrogen stored at $-80\,^{\circ}\mathrm{C}$.

3.3.2.2 Tissue Sectioning

Sections of $8\,\mu$m in thickness were cut on a cryostat ($-30\,^{\circ}\mathrm{C}$) and each section was adhered to a membrane slide (Molecular Machines & Industries).

3.3.2.3 Tissue staining

Staining was performed using the Life Technologies Laser-Capture Microdissection (LCM) Staining kit using a 7:3 ratio mix of ethanolic solutions of Cresyl Violet (CV) nuclear stain and Eosin Yellow (EY) cytoplasmic stain (Sigma Aldrich), respectively. Slides were subsequently dehydrated through graded alcohols and transferred into a chamber containing xylene for 5 minutes. The slides were then desiccated for 5 minutes.

3.3.2.4 Laser-capture microdissection

LCM was performed using the mmiCellCut® laser-capture microdissection system (Molecular Machines & Industries). Inner circular and outer longitudinal myometrial tissues were obtained separately, where care was taken to avoid blood vessels and glands. Microdissected tissue sections were collected using 500 μL mmi Isolation® tubes with adhesive lid and diffuser. Acquisition time was kept below 30 minutes.

3.3.2.5 RNA isolation from LCM tissue sections

Total ribonucleic acid (RNA) was extracted from the LCM tissues using the Life Technologies RNAqueous®-Micro kit according to manufacturer instruction.

3.3.2.6 RNA quantity and quality check

RNA was quantitated using the Thermo Scientific NanoDrop® 1000 Spectrophotometer and checked for quality by an Agilent 2100 Bioanalyzer and the Agilent RNA 6000 Pico kit according to manufacturer instruction.

3.3.2.7 Library preparation and sequencing

RNA of acceptable quality, RIN (RNA Integrity Number) ≥ 6, was used to create complementary deoxyribonucleic acid (cDNA). The cDNA was amplified using the Nugen Ovation RNA-Seq System V2 according to the manufacturer's instructions. The Nugen Ovation Ultralow DR Multiplex System (1–8) was used for library preparation according to manufacturer's instructions. Libraries were validated using a DNA 1000 chip on an Agilent 2100 Bioanalyzer according to manufacturer's instructions. Libraries were sequenced on the Illumina HiSeq 2500 platform (Illumina, San Diego, CA, USA) using a 51 bp paired-end indexed run.

3.3.2.8 Data quality assessment and analysis

The 51 bp paired-end sequencing reads were inspected for low quality scores, adapter sequence contamination, and other overrepresented sequences, using FASTQC (Andrews, 2012). TopHat 2.0.9 (Kim *et al.*, 2013) was used to align reads of acceptable quality against the UCSC *Rattus norvegicus* (rn5) reference transcriptome from Illumina iGenomes (Gibbs *et al.*, 2004). The mapped reads were sorted and indexed using SAMtools-0.1.19 (Li *et al.*, 2009), to prepare data for the Integrative Genomics Viewer (IGV) (Thorvaldsdóttir *et al.*, 2012).

Sailfish-0.6.2 (Patro *et al.*, 2013) was used to used to estimate transcript abundance in the form of transcripts per million (TPM) (Wagner *et al.*, 2012), using the following equation:

$$\mathrm{TPM} = \frac{\mathrm{r_g} \times \mathrm{rl} \times 10^6}{\mathrm{fl_g} \times \mathrm{T}}, \tag{3.7}$$

where $\mathrm{r_g}$ represents the number of reads mapping to feature g, rl represents the mean feature length, $\mathrm{fl_g}$ represents the length of feature g, and T is the total number of mappable reads.

In order to detect the change in gene expression in the transition from pregnancy to labour, comparisons were made between the mean TPMs for connexin-43 (Cx43) and connexin-45 (Cx45) at gestational days 19.25 and 22 (in labour). The inner and outer myometrial layers were considered separately.

3.4 Results

The effect of varying the gap-junctional conductance band width is studied first. We then examine cases in which the conductance relaxes to a steady state over a certain period of time. In more sophisticated simulations, the time constant is dependent on the voltage difference between neighbouring cells.

3.4.1 Minimal gap-junctional conductance bandwidth

Numerical simulations with the step function model indicate that there is a critical minimal gap-junctional conductance band below which global excitation cannot be achieved (Figure 3.10a). For conductance bandwidths of 100 mV, 80 mV, 60 mV, and 40 mV, full activity is observed with a fully connected lattice. However, once the conductance bandwidth drops below 40 mV, all activity disappears, and only the perturbed cell is capable of being excited. The transition from excitation to quiescence is quite steep and takes place over a very small range of bandwidth values: between 40 mV and 39 mV (Figure 3.10b). Simulations with several lattice sizes indicate that this transition has the character of a discontinuous phase transition in the limit of infinite lattice size (see Figures 3.11 and 3.12 for further details).

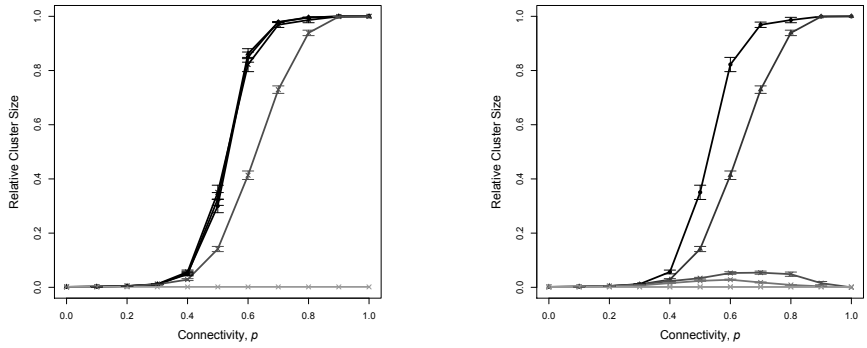

(a) **(b)**

Figure 3.10: Relative cluster size versus connectivity p for a lattice with gap-junctional conductance related to voltage-dependence with a step function. Points show mean ± SEM of 100 simulations for a 25 × 25 lattice. In all simulations, an initial perturbation of 1 was used. Lines represent the different widths of the gap-junctional conductance band in the step function model. (a) Widths of 100 mV, 80 mV, and 60 mV are shown in black, and widths of 40 mV and 20 mV are shown on a graded scale from dark to light; (b) Lines show widths of 60 mV, 40 mV, 39 mV, 38 mV, 30 mV, and 20 mV on a graded scale from dark to light. Activity is lost between widths of 40 mV and 39 mV.

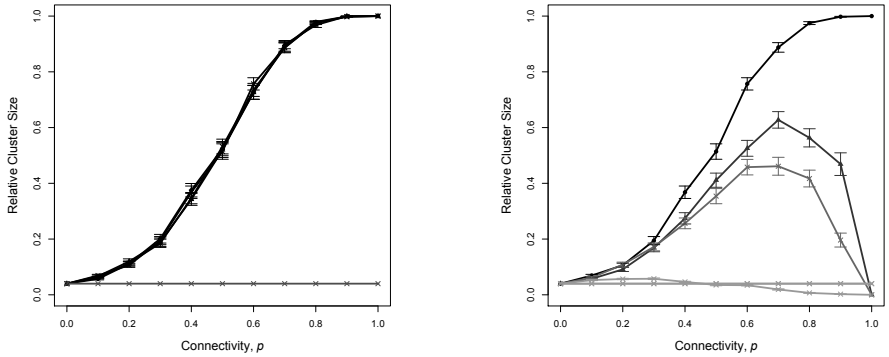

(a) **(b)**

Figure 3.11: Relative cluster size versus connectivity for a lattice with gap-junctional conductance related to voltage-dependence with a step function. Points show mean ± SEM of 100 simulations for a 5 × 5 lattice. In all simulations, an initial perturbation of 1 was used. Lines represent the different widths of the gap-junctional conductance band in the step function model. (a) Widths of 100 mV, 80 mV, 60 mV, and 40 mV are shown in black, and a width of 20 mV is shown in grey; (b) Lines show widths of 40 mV, 39 mV, 38 mV, 35 mV, 30 mV, and 20 mV on a graded scale from dark to light.

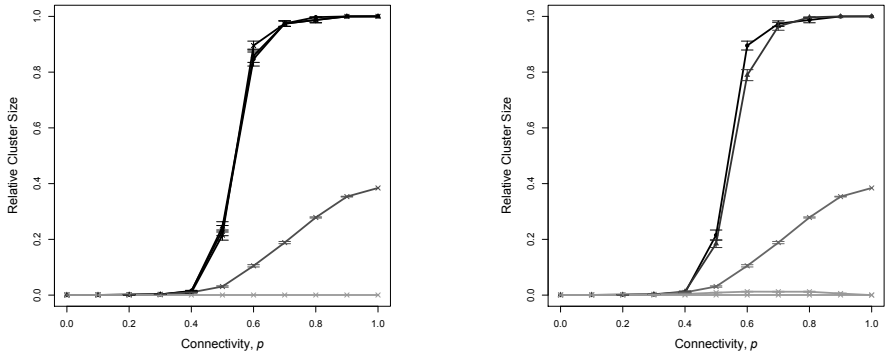

(a) **(b)**

Figure 3.12: Relative cluster size versus connectivity for a lattice with gap-junctional conductance related to voltage-dependence with a step function. Points show mean ± SEM of 100 simulations for a 50 × 50 lattice. In all simulations, an initial perturbation of 1 was used. Lines represent the different widths of the gap-junctional conductance band in the step function model. (a) Widths of 100 mV, 80 mV, and 60 mV are shown in black, and widths of 40 mV and 20 mV are shown in shades of grey from dark to light; (b) Widths of 60 mV, 41 mV, 40 mV, 39 mV, and 20 mV are shown on a graded scale from dark to light.

The critical value of the bandwidth is located between the apparent bandwidth values of Type I and Type II gap junctions as described by Miyoshi *et al.* (1996); (Figure 3.13a). This strongly suggests that physiological significance can be attached to the qualitative difference between bandwidths for which no global excitation is achieved, and those bandwidths that permit global excitation.

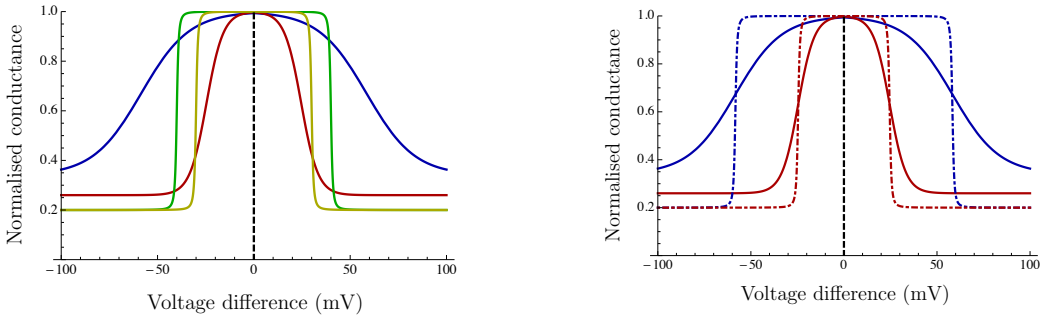

Figure 3.13: The relationship between conductance and voltage difference for a selection of models. The solid blue and solid red lines represent the Miyoshi *et al.* (1996) Type I and II models, respectively. (a) The green and yellow lines represent step function widths at the extremes of the critical range of values for total loss of excitability; (b) The blue and red dot-dashed lines represent widths outside of the critical range, chosen to coincide with the mid-points of conductances of the Type I and Type II models, respectively.

To assess the hypothesis that the threshold bandwidth value is significant, we ran simulations in which cell-to-cell couplings were randomly assigned the bandwidth corresponding to Type I or Type II (Figure 3.13b), using probabilities of inter-cell connections of 0.4, 0.6, 0.8, and 1. The relative cluster size increases with the proportion of Type I gap junctions (Figure 3.14), with a steep increase between ratios of Type II to Type I gap junctions of 0.4 and 0.6. This qualitative result is also found with lower connection probabilities. As the connectivity of the lattice is decreased, the transition values shift in favour of a larger proportion of Type I gap junctions.

The qualitative results obtained with the step function model were repeated in a model which more closely represented the shape of the Type I and Type II Miyoshi *et al.* (1996)

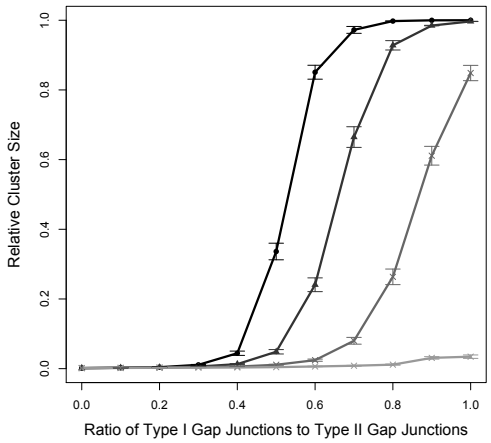

Figure 3.14: The relationship between the proportion of cells that become excited, and the ratio of Type I gap junctions (*i.e.* excitation possible) to Type II gap junctions (*i.e.* excitation impossible), for a smoothed step function model. Lines show probabilities of connections existing between any two cells of 1, 0.8, 0.6, and 0.4 on a graded scale from dark to light. Points show mean ± SEM of 100 simulations for a 25 × 25 lattice, all with an initial perturbation of 1.

fits (see Section 3.3.1.2). There is a minimum gap-junctional conductance bandwidth beyond which no excitation can take place, and a clear transition between excited and quiescent states. The results of this simulation are detailed in Figures 3.15 and 3.16.

Network activity depends on the connectivity p and the ratio of Type II to Type I gap junctions. Figure 3.17 suggest that there is a defined set of conditions that promote network excitation. The majority of parameter combinations result in no activity. However, a network with high connectivity and a higher proportion of Type I gap junctions relative to Type II gap junctions maximises the likelihood of near full activity.

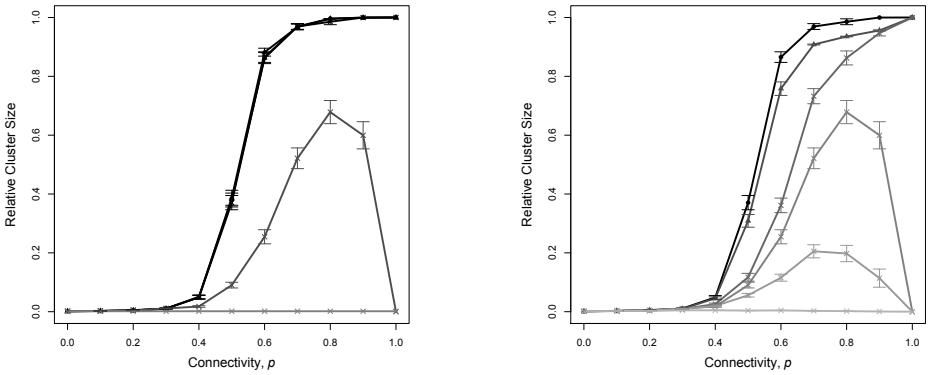

(a) **(b)**

Figure 3.15: Relative cluster size versus connectivity p for a lattice with gap-junctional conductance related to voltage-dependence using a symmetrical Miyoshi *et al.* (1996) relationship. Points show mean ± SEM of 100 simulations for a 25 × 25 lattice. In all simulations, an initial perturbation of 1 was used. Lines represent the different widths of the gap-junctional conductance band in the step function model. (a) Widths of 100 mV and 80 mV are shown in black, and widths of 60 mV, 40 mV, and 20 mV are shown in grey; (b) Lines show widths of 60 mV, 45 mV, 42 mV, 40 mV, 38 mV, and 35 mV on a graded scale from dark to light.

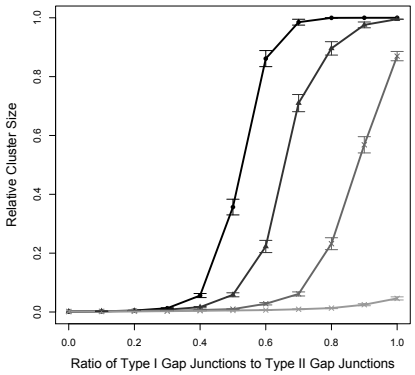

Figure 3.16: The relationship between the proportion of cells that become excited, and the ratio of Type I gap junctions (*i.e.* excitation possible) to Type II gap junctions (*i.e.* excitation impossible), for a symmetrical Miyoshi *et al.* (1996) model. Lines show probabilities of connections existing between any two cells of 1, 0.8, 0.6, and 0.4 on a graded scale from dark to light. Points show mean ± SEM of 100 simulations for a 25 × 25 lattice, all with an initial perturbation of 1.

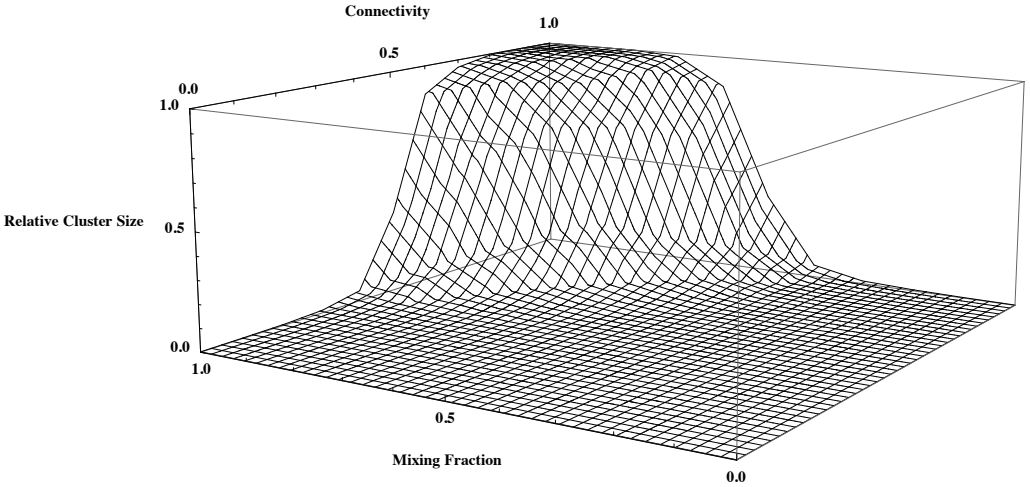

Figure 3.17: Three-dimensional illustration of the network activity (relative cluster size) with varying connectivity p and proportion of Type I and Type II gap junctions. Each point in the mesh represents the mean of 100 simulations for a 25×25 lattice with an initial perturbation of 1. The density of the grid lines indicates that a larger proportion of cells are able to become excited with higher connectivity, and a greater proportion of Type I gap junctions than Type II gap junctions.

3.4.2 The effect of gating kinetics

Here we examine the symmetrical Miyoshi model with voltage-gated gap junctions using a fixed time constant. The excitability of a network with exclusively Type I gap junctions is unaffected by the value of the time constant — there is always full activity at full connectivity (Figure 3.18a). By contrast, the time constant is a key parameter in a network with Type II gap junctions. With a small time constant, Type II gap junctions are unable to propagate any activity, as before. However, as the time constant is increased, the relationship between connectivity and relative cluster size assumes one of two distinct forms (Figure 3.18b). For time constants between 0.87 and 1.49 seconds (0.54 and 0.93 in dimensionless units) the relationship follows a bell-shaped curve, indicative of the importance of spatial heterogeneity in exciting the network. For time constants larger than 1.51 seconds (0.94 in model values) the relationship follows a sigmoidal curve in which full connectivity corresponds to full excitation. These results are summarised in Table 3.3.

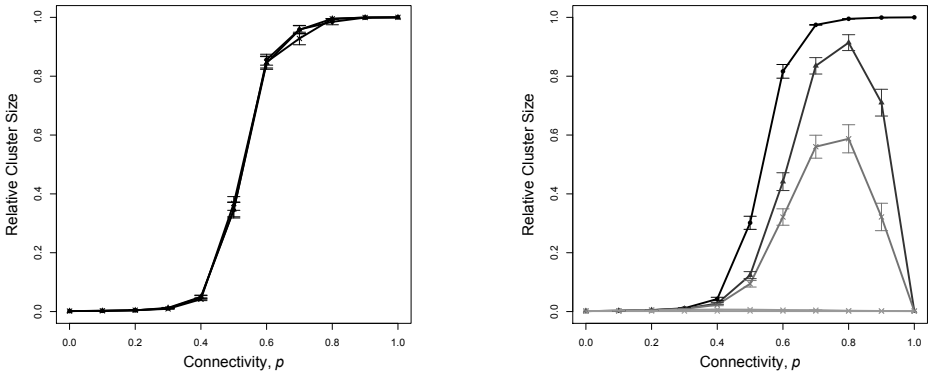

(a) **(b)**

Figure 3.18: Relative cluster size versus connectivity p for a dynamic coupled lattice which relaxes back to the steady state in a fixed time period represented by different lines. Points show mean ± SEM of 100 simulations for a 25 × 25 lattice. In all simulations, an initial perturbation of 1 was used. The lines represent different time constant values. (a) Type I gap junctions. Lines represent time constants of 1 s, 0.5 s, and 0.1 s all shown in black due to their close proximity; (b) Type II gap junctions. Lines represent time constants of 1 s, 0.9 s, 0.7 s, 0.5 s, and 0.1 s on a graded scale from dark to light.

Table 3.3: Summary of the excitation threshold time constants for Type II gap junctions.

Time constant (model units)	**Time constant (seconds)**	**Result**
$t \geqslant 1$	$\tau \geqslant 1.162$	Sigmoidal shape
$0.1 \leqslant t \leqslant 0.9$	$0.116 \leqslant \tau \leqslant 1.046$	Bell shape
$t < 0.1$	$\tau < 0.116$	No activity

Comparisons are drawn between the time constant thresholds identified above, and the time constant relationship with voltage difference for Type II gap junctions (Figure 3.9b). For a voltage difference greater than ±50 mV, excitation in the network is not possible. For voltage differences smaller than ±35 mV, excitation is always possible. When the voltage difference is between ±35 mV and ±50 mV, spatial heterogeneity in connections is essential to obtain excitation in the network.

Finally, we examine a network with varying proportions of Type I and Type II gap junctions. As before, cell-to-cell couplings were randomly assigned the bandwidth corresponding to Type I or Type II. In addition, the voltage-dependent time constants corresponding

to the chosen bandwidth are incorporated into the model using the Gaussian fit detailed in Equation (3.6). Type II gap junctions remain unable to produce full network excitation even at full connectivity (Figure 3.19). A small influence of spatial heterogeneity is apparent for networks with exclusively Type II gap junctions. Around 20 % of cells are able to become excited with connectivities in the range 0.6 – 0.8. Type I gap junctions are unaffected by the switch to voltage-dependent time constants. The cells in the network are still able to exhibit full activity with full connectivity. As the connectivity is reduced, so is the excitation.

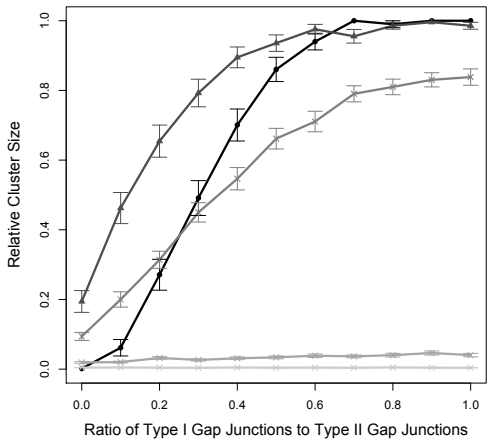

Figure 3.19: The relationship between the proportion of cells that become excited, and the ratio of Type I gap junctions to Type II gap junctions, for a model with dynamic gap-junctional conductances. Lines show probabilities of connections existing between any two cells of 1, 0.8, 0.6, 0.4, and 0.2 on a graded scale from dark to light. Points show mean ± SEM of 100 simulations for a 25 × 25 lattice, with an initial perturbation of 1.

3.4.3 Experimental results

Transcriptomics data suggest that expression of connexin-45 (Cx45) in the inner myometrium is substantially lower on gestation day 22 (in labour) as compared to gestation day 19.25 (Figure 3.20a). On the other hand, there does not appear to be a difference in connexin-43 (Cx43) expression between these two points in time in either the inner or

outer myometrium (Figure 3.20b). Taken together, these data would suggest an increase of the Cx43:Cx45 ratio, *i.e.* a relative enrichment of Cx43.

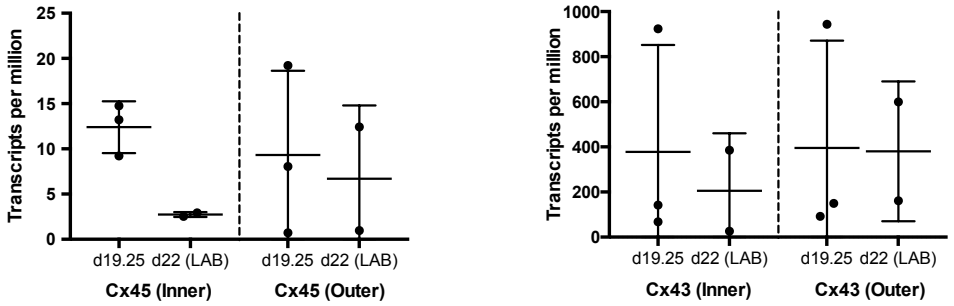

Figure 3.20: Gene expression of (a) connexin-45 (Cx45) in the inner and outer myometrium; (b) connexin-43 (Cx43) in the inner and outer myometrium at rat gestation days of 19.25 and 22 (in labour, LAB). Lines show the mean gene expression ± SD with $n = 3$ for gestation day 19.25 and $n = 2$ for gestation day 22 (LAB).

3.5 Discussion

Our findings suggest that the relative proportions of connexin-43 (Cx43) and connexin-45 (Cx45) are vital in initiating contractions in the myometrium during parturition. We build on the results obtained by Miyoshi *et al.* (1996) to show that global excitation can be attained in a model network relying solely on Cx43 proteins, whereas this is not the case for a system using only Cx45. In addition, we develop a model in which the conductance of a gap junction is dynamic and has a voltage-dependent time constant, Cx45 having faster gating kinetics than Cx43. We demonstrated that this time constant is a key factor in determining whether global excitation can be achieved. At shorter time constants, heterogeneity in the density of gap junction connections plays a more prominent role in deciding whether activity can spread.

In rodents (as in most mammals, but not humans (Weiss *et al.*, 2006)), the myometrium can be divided into two distinct layers of smooth muscle: the inner circular layer and

the outer longitudinal layer (Brody & Cunha, 1989b). Our experimental data indicate down-regulation of Cx45 expression in the rat as labour approaches, in contrast to Cx43 expression where no change at the end of pregnancy appears to be evident. Chan *et al.* (2014) found similar results in human myometrium, analysing the RNA of myometrial samples from pregnant women (5 from women in labour, and 5 from women at full term, but not in labour). These authors showed that Cx43 expression remains unchanged between the two sample groups, whereas Cx45 expression is significantly down-regulated in the "in labour" group in comparison with the "not-in-labour" group (Figure 3.21). These results are in accordance with our data, which furthermore suggest that the significant changes found by Chan *et al.* (2014) were owing to changes in expression taking place in the inner myometrium as opposed to the outer myometrium. Our model simulations show that an elevated proportion of Cx43 proteins is a key factor in modulating conductance. This accords well with results obtained by Döring *et al.* (2006) and Tong *et al.* (2009), who found that in a Cx43 knock-out mouse, the lack of intracellular myometrial coupling results in weaker contractions and delayed labour. These various lines of evidence strongly suggest that the Cx43:Cx45 ratio is instrumental in controlling the global excitability of

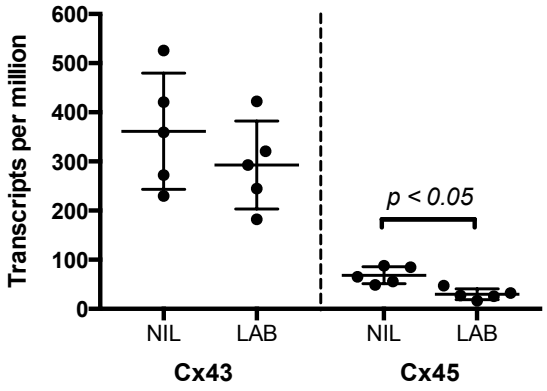

Figure 3.21: The gene expression of connexin-45 and connexin-43 in "in labour" human myometrial samples (LAB) compared with "not-in-labour" human myometrial samples taken at term (NIL). Lines show the mean gene expression ± SD of 5 samples. There is no significant change in connexin-43 between the non-labour and labour samples. There is a significant decrease in connexin-45 expression in labour when compared with non-labour ($p = 0.0030$). Graph created from data published by Chan *et al.* (2014).

the myometriocyte network.

The connexin protein Cx45 plays an important role in cardiac myocytes; it is found in the atrioventricular (AV) node and the adjoining His bundles (Gourdie & Lo, 1999; Frank *et al.*, 2012). While Cx45 is not essential for continued survival in the adult mouse (Frank *et al.*, 2012), Cx45 knock-out mice die from heart failure *in utero* (Kumai *et al.*, 2000; Krüger *et al.*, 2000). Without Cx45, contractions initiated in the AV node are not coordinated with the contractions in the ventricles; Cx45 may play a similar role in the myometrium, *i.e.* to inhibit contractions until the development of the fœtus has advanced sufficiently for delivery. The inviability of Cx45 knock-out mouse embryos (Kumai *et al.*, 2000; Krüger *et al.*, 2000) precludes a test of this hypothesis *in vivo*. However, Cx45 knock-out *in vitro* studies could be used to demonstrate the development of global network events.

Voltage-dependent gap junctions have previously been considered in mathematical models (Vogel & Weingart, 1998; Chen-Izu *et al.*, 2001). Baigent *et al.* (1997); Baigent (2003) and Donnell *et al.* (2009) considered a two-cell model coupled by a dynamic gap junction which resides in one of three states, giving insights into cell connections on a local scale, emphasising channel kinetics and ionic flows in great detail. By contrast, the present model focuses on overall excitability of the network as a function of spatial heterogeneity of the functional properties of the gap junctions, rather than on the propagation of activity wave fronts and the spatial patterning of such fronts; these aspects have been considered elsewhere (Singh *et al.*, 2012; Benson *et al.*, 2006; Barkley, 1991; Bub *et al.*, 2002). Whereas we considered the global activation threshold in a electrotonically coupled smooth muscle syncytium, a general argument regarding the all-or-none character of synaptically coupled networks, such as the central nervous system, was advanced by Ashby *et al.* (1962).

The present work has not considered heteromeric gap junction channels with both Cx45 and Cx43 proteins. We assumed that the relationships given by Miyoshi *et al.* (1996) correspond to homomeric gap junction channels. Martinez *et al.* (2002) demonstrated

that these two gap junction proteins are coexpressed in cardiac cells, and that homomeric channels of either Cx45 or Cx43 have different unitary conductances. A heteromeric gap junction channel might exhibit non-symmetrical behaviour; this will require further experimental studies in order to inform our model.

We do not report an increase in Cx43 expression in the rat between day $19\frac{1}{4}$ and day 22. This finding is in keeping with the literature in that the rise in Cx43 occurs prior to parturition (4 days before term in the rat). Cx43 proteins are stored in vesicles and only trafficked to the membrane gap junctions when labour commences, so causing a increase in functional expression in labour, but not an increase in gene expression in the tissue (Garfield & Hayashi, 1981; Risek *et al.*, 1990; Winterhager *et al.*, 1991; Hendrix *et al.*, 1992; Tabb *et al.*, 1992). Studies using immunohistochemistry and western blot analysis have demonstrated the functional increase in Cx43 expression at term, as well as a decrease in Cx45 (Albrecht *et al.*, 1996; Kilarski *et al.*, 1998). Albrecht *et al.* (1996) suggested that the ratio of Cx43 to Cx45 might be crucial for increased network connectivity associated with the initiation of labour, which is in agreement with our finding that relative numbers of Cx43 and Cx45 are a key permissive factor — Cx45 effectively acting as a brake on contractile activity in the uterus. As parturition approaches, Cx45 becomes down-regulated, allowing contractions to increase in strength and frequency.

3.6 Acknowledgements

RES is grateful to EPSRC for a PhD studentship through the MOAC Doctoral Training Centre at the University of Warwick: grant number EP/F500378/1.

CM gratefully acknowledges funding for a PhD studentship from the BBSRC through the Systems Biology Doctoral Training Centre at the University of Warwick: grant number BB/G530233/1.

Chapter 4

Conclusions and future work

4.1 Conclusions

Understanding the role that gap junction proteins play in the transition of the myometrium from a quiescent to an active state is of vital clinical importance in diagnosing and treating preterm labour, and in managing full term deliveries. In this thesis, a mathematical model has been constructed to examine the hypotheses that spatial heterogeneity enhances myometrial activity and that the connexin structure is regulated in order to preserve quiescence during gestation and activity in labour. The model follows FitzHugh-Nagumo dynamics and incorporates cell capacitance and resting membrane potential data, as well as voltage difference/conductance relationships from human, mouse, and rat experimental results. The mathematical model was used to address the original aims, as shall be detailed in the following two sections.

4.1.1 Spatial heterogeneity

Model analysis defined the parameter ranges required for a fully connected network that permitted global activity, which was a function of the inciting stimulus. With the introduction of spatial heterogeneity in the presence and strength of inter-cell couplings, it was found that even a modest degree of heterogeneity was sufficient to allow global activ-

ity with parameter values from outside the prescribed range. Heterogeneity in coupling structures allows the network to respond in a graded manner to a wider range of stimuli. The transition from quiescence to excitation can therefore be modulated by physiological control mechanisms. It is proposed that heterogeneity alleviates the 'current sink' effect: local pockets of excitability are created where the stimulated cell is less affected by the charge drain imposed by its neighbours.

The correlation between activity in the stimulated cell and in cells located at increasing distance from the stimulated cell was also studied as a function of the proportion of excited cells. It was demonstrated that for networks with fewer connections between cells, a much larger correlation was observed when fewer then 10 % of cells were excited when compared with networks with more than 90 % of cells excited. This effect was more pronounced with a probability of connections existing of 0.6 when compared with a fully connected network. This result supports the notion of excitation pockets: a cluster of cells that are relatively isolated in the network are better able to propagate activity.

Networks driven by pacemaker cells were also found to be modulated by heterogeneity. A fully connected network displays a reduction in the frequency of pacemaker oscillations, and activity may be inhibited altogether. Maximal excitability is associated with a moderate degree of spatial heterogeneity. This theoretical result was supported by preliminary experimental data in which an increase in heterogeneity increases the frequency of action potential signals. These findings suggest that individual cells are able to regulate their pacemaker activity by partially isolating themselves within the network.

It has already been established in the literature that gap junction expression correlates with the shift from uterine quiescence to global activity (see Chapter 1 for a detailed account and references). It is suggested here that a shift in spatial heterogeneity may play a significant role in the regulation of myometrial excitability. Preterm labour may result from a premature development of spatial heterogeneity. Detailed non-invasive mapping

of heterogeneity may in future prove to be an essential diagnostic tool to monitor the development of excitability throughout pregnancy.

4.1.2 Voltage-dependent gap junctions

The voltage-dependent model showed that the relative proportions of connexin-43 and connexin-45 proteins are essential in initiating contractions in labour. Models with coupling strengths drawn exclusively from the "Type I Miyoshi" distribution (exclusively connexin-43) reliably achieve global activity. In contrast, models with coupling strengths drawn exclusively from the Type II distribution (exclusively connexin-45) are invariably unable to achieve global activity. Models with dynamic conductances have also been developed, with connexin-45 having faster gating kinetics than connexin-43. It was found that the time constant is a key factor in determining global activity: at shorter time constants heterogeneity in gap junction connection density plays a prominent role in determining whether activity can spread.

The mathematical modelling results are supported by experimental evidence. Data are presented from rat myometrial samples in which connexin-45 is shown to decrease in the inner myometrium at term, whereas no changes are observed in connexin-43 expression. These results are supported by the findings of Chan *et al.* (2014) in which a down-regulation of connexin-45 is demonstrated in human myometrial samples at term, and no change in connexin-43 is observed.

It is proposed that connexin-45 acts as a master brake, blocking activity in the uterus throughout the majority of gestation. As labour approaches, connexin-45 is down-regulated to allow connexin-43 to become the dominant connexin in gap junction hexamers. With a smaller proportion of connexin-45, contractions are permitted to increase in strength and frequency in order to deliver the baby. The clinical identification of this connexin ratio may prove a useful diagnostic tool for the prediction of preterm labour.

4.2 Future work

In this thesis FitzHugh-Nagumo dynamics have been used to model the excitation and recovery of a myometrial cell. The primary aim of the study was to study in a qualitative manner the activity of the cell using a computationally efficient method, and a two-dimensional FitzHugh-Nagumo model was deemed to be appropriate for this purpose. A natural extension of this work would be to replace the model with one which takes into account individual ion channels and the intracellular calcium stores such as the models suggested by Morris & Lecar (1981), Rihana *et al.* (2008), Laforet *et al.* (2011), Rosa *et al.* (2012) and McCloskey *et al.* (2014).

The spatial structure of the network is another point of departure for further investigations. In this thesis, we consider a two-dimensional structure in which each cell is connected to four others. Models in which each cell is connected to six others (the hexagonal lattice) were investigated and discussed in Section 2.5, but do not display marked qualitative differences in activity patterns. The next step would be fully realised three-dimensional structures. With a working cylindrical model, the number of cells in the model (both in length and diameter) can be adjusted in order to investigate the limiting number of cells in a muscle fibre. Beyond the critical number it is expected that activity will be unable to propagate fully throughout the fibre.

In this thesis, we only consider stochasticity through the connection structure of the network. Stochasticity may also be introduced through the cell parameters which would change the point of intersection of the two nullclines. Since the intersection point dictates the point of equilibrium, some cells would remain stable at their equilibrium point whereas others would become unstable, and so be pacemaker cells. By introducing heterogeneity through equilibrium points, a network of randomly dispersed oscillators would be generated. The ability of the oscillators to drive the network would then be studied.

The work presented in Chapter 3 only considers gap junction channels consisting of one type of connexin protein (Figure 4.1a). Heteromeric gap junction channels are not considered. It has been demonstrated that connexin-45 and connexin-43 hemichannels can co-exist (Figure 4.1b), and it is proposed that such a channel would display asymmetrical conductance behaviour (Martinez *et al.*, 2002). However, additional experimental studies of asymmetrical channel conductance would be required to construct a model displaying these properties.

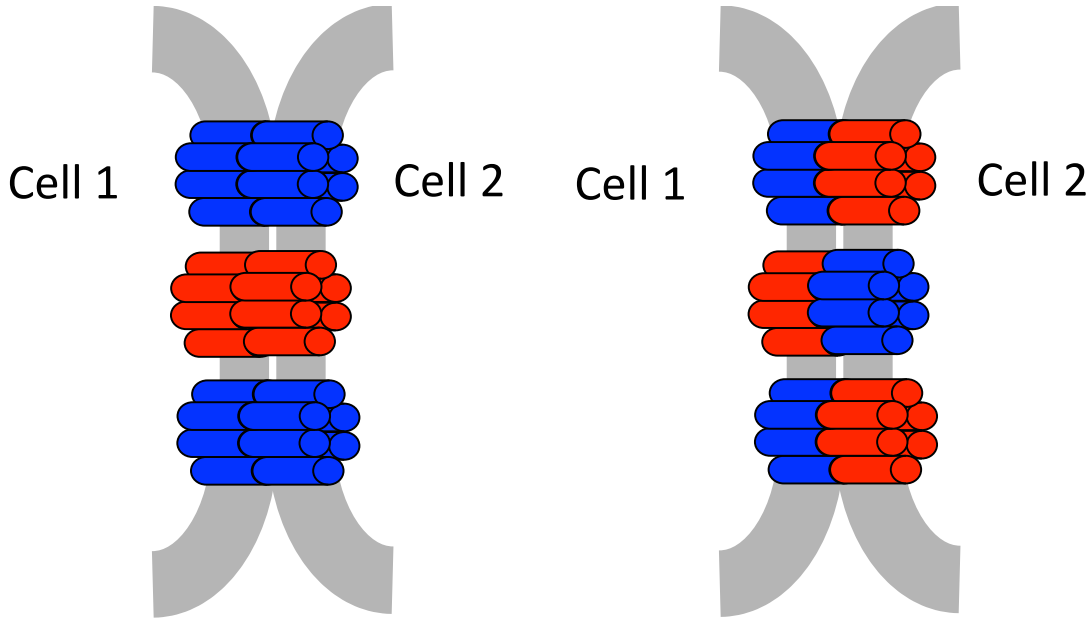

Figure 4.1: Homomeric and heteromeric gap junctions. Connexin-43 is shown in red; connexin-45 is shown in blue. (a) Each channel consists of one connexin protein only; (b) Each hemichannel consists of one connexin protein but can co-exist with a hemichannel made up of a different connexin protein.

The goal of mathematical studies of the myometrium is to construct a model which closely tracks the contraction and relaxation of the uterus, and monitors the biophysical and structural changes throughout the course of pregnancy. The primary limitation to this goal is computational efficiency; the more detailed the model becomes, the fewer cells can be feasibly studied without increasing the computational power significantly. The FHN model used throughout this thesis provides a good balance between computational efficiency and

realistic modelling of electrical activity of the myometrium *in vivo*. Experimental work which supports the conclusions drawn from the simulations suggests that the FHN model is sufficient to make qualitative statements about the changes in the myometrium as labour approaches. Our results demonstrated that a change in the spatial structure and connexin composition of gap junctions occurs immediately prior to parturition; these findings may be used in the future as targets to provide clinical diagnosis and treatment of both preterm labour and postpartum hæmorrhage.

Bibliography

Afting, E.-G. and Schenk, E. A. 1978. DNA in the rat uterus myometrium during pregnancy and postpartum involution. *Analytical Biochemistry*, **86**, 90–99.

Aguilar, H. N. and Mitchell, B. F. 2010. Physiological pathways and molecular mechanisms regulating uterine contractility. *Human Reproduction Update*, **16**, 725–744.

Alberts, B., Johnson, A., Lewis, J., Raff, M., Roberts, K., and Walter, P. 2008a. *Molecular Biology of the Cell*. 5th edn. Garland Science. 11. Membrane Transport of Small Molecules and the Electrical Properties of Membranes, pp. 651–694.

Alberts, B., Johnson, A., Lewis, J., Raff, M., Roberts, K., and Walter, P. 2008b. *Molecular Biology of the Cell*. 5th edn. Garland Science. 12. Intracellular Compartments and Protein Sorting, pp. 695–748.

Alberts, B., Johnson, A., Lewis, J., Raff, M., Roberts, K., and Walter, P. 2008c. *Molecular Biology of the Cell*. 5th edn. Garland Science. 19. Cell Junctions, Cell Adhesion, and the Extracellular Matrix, pp. 1131–1204.

Alberts, B., Johnson, A., Lewis, J., Raff, M., Roberts, K., and Walter, P. 2008d. *Molecular Biology of the Cell*. 5th edn. Garland Science. 15. Mechanisms of Cell Communication, pp. 879–964.

Albrecht, J. L., Atal, N. S., Tadros, P. N., Orsino, A., Lye, S. J., Sadovsky, Y., and Beyer, E. C. 1996. Rat uterine myometrium contains the gap junction protein connexin45, which has a differing temporal expression pattern from connexin43. *American Journal of Obstetrics & Gynecology*, **175**, 853–858.

Alexandrova, M. and Soloff, M. S. 1980. Oxytocin receptors and parturition. I. Control of oxytocin receptor concentration in the rat myometrium at term. *Endocrinology*, **106**, 730–735.

Aliev, R. R. and Panfilov, A. V. 1996. A simple two-variable model of cardiac excitation. *Chaos, Solitons & Fractals*, **7**(3), 292–301.

Anderson, G. F., Kawarabayashi, T., and Marshall, J. M. 1981. Effect of indomethacin and aspirin on uterine activity in pregnant rats: comparison of circular and longitudinal muscle. *Biology of Reproduction*, **24**, 359–372.

Anderson, N. C. 1978. Physiological basis of myometrial function. *Seminars in Perinatology*, **2**, 211–222.

Andrews, S. 2012. *FastQC A Quality Control tool for High Throughput Sequence Data.*

Ashby, W. R., von Foerster, H., and Walker, C. C. 1962. Instability of pulse activity in a net with threshold. *Nature*, **196**, 561–562.

Babu, Y. S., Sack, J. S., Greenhough, T. J., Bugg, C. E., Means, A. R., and Cook, W. J. 1985. Three-dimensional structure of calmodulin. *Nature*, **315**, 37–40.

Baigent, S. 2003. Cells coupled by voltage-dependent gap junctions: the asymptotic dynamical limit. *Biosystems*, **68**(2–3), 213–222.

Baigent, S., Stark, J., and Warner, A. 1997. Modelling the effect of gap junction nonlinearities in systems of coupled cells. *Journal of Theoretical Biology*, **186**(2), 223–229.

Bais, J. M., Eskes, M., Pel, M., Bonsel, G. J., and Bleker, O. P. 2004. Postpartum haemorrhage in nulliparous women: incidence and risk factors in low and high risk women. *European Journal of Obstetrics & Gynecology and Reproductive Biology*, **115**(2), 166–172.

Barclay, M., Andersen, H., and Simon, C. 2010. Emergent behaviours in a deterministic model of the human uterus. *Reproductive Sciences*, **17**(10), 948–954.

Barkley, D. 1991. A model for fast computer simulation of waves in excitable media. *Physica D*, **49**, 61–70.

Batra, S. 1985. Effect of oxytocin on calcium movements in uterine smooth muscle. *Regulatory Peptides. Supplement*, **4**, 78–81.

Beblo, D. A., Wang, H-Z., Beyer, E. C., Westphale, E. M., and Veenstra, R. D. 1995. Unique conductance, gating, and selective permeability properties of gap junction channels formed by connexin40. *Circulation Research*, **77**(4), 813–822.

Bengtsson, B., Chow, E. M. H., and Marshall, J. M. 1984. Activity of circular muscle of rat uterus at different times in pregnancy. *American Journal of Physiology*, **246**, C216–C223.

Benham, C. D. and Tsien, R. W. 1987. A novel receptor-operated Ca^{2+}-permeable channel activated by ATP in smooth muscle. *Nature*, **328**, 275–278.

Benson, A. P., Clayton, R. H., Holden, A. V., Kharche, S., and Tony, W. C. 2006. Endogenous driving and synchronization in cardiac and uterine virtual tissues: bifurcations and local coupling. *Philosophical Transactions of the Royal Society A*, **364**(1842), 1313–1327.

Berridge, M. J. 1993. Inositol trisphosphate and calcium signalling. *Nature*, **361**, 315–325.

Berridge, M. J. 2014 (Last retrieved: 6 November 2014). *Cell Signalling Biology*. `www.cellsignallingbiology.org`.

Berthoud, V. M., Minogue, P. J., Laint, J. G., and Beyer, E. C. 2004. Pathways for degradation of connexins and gap junctions. *Cardiovascular Research*, **62**(2), 256–267.

Blackburn, S. T. 2007. *Maternal, Fetal, & Neonatal Physiology: A clinical perspective*. 3rd edn. Missouri, USA: Saunders, Elsevier.

Blanks, A. M., Zhao, Z-H., Shmygol, A., Bru-Mercier, G., Astle, S., and Thornton, S. 2007. Characterization of the molecular and electrophysiological properties of the T-type calcium channel in human myometrium. *The Journal of Physiology*, **581**, 915–926.

Blaustein, M. P. and Lederer, W. J. 1999. Sodium/Calcium exchange: its physiological implications. *Physiological Reviews*, **79**(3), 763–854.

Blencowe, H., Cousens, S., Oestergaard, M. Z., Chou, D., Moller, A. B., Narwal, R., Adler, A., Garcia, C. Vera, Rohde, S., Say, L., *et al.* 2012. National, regional, and worldwide estimates of preterm birth rates in the year 2010 with time trends since 1990 for selected countries: A systematic analysis and implications. *The Lancet*, **379**, 2162–2172.

Brody, J. R. and Cunha, G. R. 1989a. Histologic, morphometric, and immunocytochemical analysis of myometrial development in rats and mice: I. Normal development. *American Journal of Anatomy*, **186**, 1–20.

Brody, J. R. and Cunha, G. R. 1989b. Histologic, morphometric, and immunocytochemical analysis of myometrial development in rats and mice: II. Effects of DES on development. *American Journal of Anatomy*, **186**, 21–42.

Brosens, J. J. and Gellersen, B. 2006. Death or survival—progesterone-dependent cell fat decisions in the human endometrial stroma. *Journal of Molecular Endocrinology*, **36**, 389–398.

Brosens, J. J., Hayashi, N., and White, J. O. 1999. Progesterone receptor regulates decidual prolactin expression in differentiating human endometrial stromal cells. *Endocrinology*, **140**, 4809–4820.

Brosens, J. J., Wilson, M. S., and Lam, E. W. 2009. FOXO transcription factors: from cell fate decisions to regulation of human female reproduction. *Advances in Experimental Medicine and Biology*, **665**, 227–241.

Brun, J. L., Galant, C., Delvaux, D., Lemoine, P., Henriet, P., Courtoy, P. J., and Marbaix, E. 2009. Menstrual activity of matrix metalloproteinases is decreased in endometrium regenerating after thermal ablation. *Human Reproduction*, **24**, 333–340.

Bruzzone, R., Haefliger, J. A., Gimlich, R. L., and Paul, D. L. 1993. Connexin40, a component of gap junctions in vascular endothelium is restricted in its ability to interact with other connexins. *Molecular Biology of the Cell*, **4**(1), 7–20.

Bub, G., Shrier, A., and Glass, L. 2002. Spiral wave generation in heterogeneous excitable media. *Physical Review Letters*, **88**(5), 058101.

Buhimschi, C., Boyle, M. B., and Garfield, R. E. 1997. Electrical activity of the human uterus during pregnancy as recorded from the abdominal surface. *Obstetrics & Gynecology*, **90**, 102–111.

Buhimschi, C., Boyle, M. B., Saade, G. R., and Garfield, R. E. 1998. Uterine activity during pregnancy and labor assessed by simultaneous recordings from the myometrium and abdominal surface in the rat. *American Journal of Obstetrics & Gynecology*, **178**, 811–822.

Bulletti, C., de Ziegler, D., Polli, V., Diotallevi, L., Del Ferro, E., and Flamigni, C. 2000. Uterine contractility during the menstrual cycle. *Human Reproduction*, **15**, 81–89.

Burdyga, T. and Wray, S. 2005. Action potential refractory period in ureter smooth muscle is set by Ca sparks and BK channels. *Nature*, **436**(7050), 559–562.

Bursztyn, L., Eytan, O., Jaffa, A. J., and Elad, D. 2007. Modeling myometrial smooth muscle contraction. *Annals of the New York Academy of Sciences*, **1101**, 110–138.

Calder, A. and Embrey, M. P. 1973. Letter: Prostaglandins and the unfavourable cervix. *The Lancet*, **2**, 1322–1323.

Campbell, O. M., Graham, W. J., and Lancet Maternal Survival Series steering group. 2006. Strategies for reducing maternal mortality: getting on with what works. *The Lancet*, **368**(9543), 1284–1299.

Carsten, M. E. 1969. Role of calcium binding by sarcoplasmic reticulum in the contraction and relaxation of uterine smooth muscle. *The Journal of General Physiology*, **53**(4), 414–426.

Casey, M. L. and MacDonald, P. C. 1997. The endocrinology of human parturition. *Annals of the New York Academy of Sciences*, **828**, 273–284.

Challis, J. R. G., Matthews, S. G., Gibb, W., and Lye, S. J. 2000. Endocrine and paracrine regulation of birth at term and preterm. *Endocrine Reviews*, **21**(5), 514–550.

Chamley, W. A. and Parkington, H. C. 1984. Relaxin inhibits the plateau component of the action potential in the circular myometrium of the rat. *Journal of Physiology*, **353**, 51–65.

Chan, W. Y. 1983. Uterine and lacental prostaglandins and their modulation of oxytocin sensitivity and contractility in the parturient uterus. *Biology of Reproduction*, **29**, 680–688.

Chan, Y-W., van den Berg, H. A., Moore, J. D., Quenby, S., and Blanks, A. M. 2014. Assessment of myometrial transcriptome changes associated with spontaneous human labour by high throughput RNA-seq. *Experimental Physiology*, **99**(3), 510–524.

Chang, D. C. 1983. Dependence of cellular potential on ionic concentrations. Data supporting a modification of the constant field equation. *Biophysical Journal*, **43**(2), 149–156.

Chen-Izu, Y., Moreno, A. P., and Spangler, R. A. 2001. Opposing gates model for voltage gating of gap junction channels. *American Journal of Physiology – Cell Physiology*, **281**(5), C1604–C1613.

Chiazze Jr, L., Brayer, F. T., Macisco, J. J., Parker, M. P., and Duffy, B. J. 1968. The length and variability of the human menstrual cycle. *The Journal of the American Medical Association*, **203**(6), 377–380.

Chow, E. H. M. and Marshall, J. M. 1981. Effects of catecholamines on circular and longitudinal uterine muscle of the rat. *European Journal of Pharmacology*, **76**, 157–165.

Chwalisz, K. 1994. The use of progesterone antagonists for cervical ripening and as an adjunct to labour and delivery. *Human Reproduction*, **9**, 131–161.

Chwalisz, K., Benson, M., Scholz, P., Daum, J., Beier, H. M., and Hegele-Hartung, C. 1994. Cervical ripening with the cytokines interleukin 8, interleukin 1 beta and tumor necrosis factor alpha in guinea-pigs. *Human Reproduction*, **9**, 2173–2181.

Cole, W. C. and Garfield, R. E. 1985. Alterations in coupling in uterine smooth muscle. PP. 215–230 of: Spray, D.C. and Bennett, M.V.L. (eds), *Gap Junctions*. Cold Spring Harbor, NY: Cold Spring Harbor Laboratory Press.

Cole, W. C. and Garfield, R. E. 1986. Evidence for physiological regulation of myometrial gap junction permeability. *American Journal of Physiology – Cell Physiology*, **251**, C411–C420.

Combs, C. A., Murphy, E. L., and Jr., R. K. Laros. 1991. Factors associated with postpartum hemorrhage with vaginal birth. *Obstetrics & Gynecology*, **77**(1), 69–76.

Conti, M. A. and Adelstein, R. S. 1981. The relationship between calmodulin binding and phosphorylation of smooth muscle myosin kinase by the catalytic subunit of 3′:5′ cAMP-dependent protein kinase. *The Journal of Biological Chemistry*, **256**, 3178–3181.

Coward, K. and Wells, D. (eds). 2013. *Textbook of Clinical Embryology.* Cambridge, UK: Cambridge University Press.

Crane, L. H. and Martin, L. 1992. Effects of the progesterone antagonist RU486 on myometrial activity in vivo in early pregnant and pseudopregnant rats. *Reproduction, Fertility and Development*, **4**, 161–166.

Csapo, A. I. 1956. Progesterone "block". *American Journal of Anatomy*, **98**, 273–291.

Csapo, A. I. 1975. The "seesaw" theory of the regulatory mechanism of pregnancy. *American Journal of Obstetrics & Gynecology*, **121**, 578–581.

Cunha, G.R. 1975. The dual origin of vaginal epithelium. *American Journal of Anatomy*, **143**, 387–392.

Del Valle, M. E., Cobo, T., Cobo, J. L., and Vega, J. A. 2012. Mechanosensory neurons, cutaneous mechanoreceptors, and putative mechanoproteins. *Microscopy Research and Technique*, **75**, 1033–1043.

Dey, S. K., Lim, H., Das, S. K., Reese, J., Paria, B. C., Daikoku, T., and Wang, H. 2004. Molecular cues to implantaion. *Endocrine Reviews*, **25**, 341–373.

Donnell, P., Baigent, S., and Banaji, M. 2009. Monotone dynamics of two cells dynamically coupled by a voltage-dependent gap junction. *Journal of Theoretical Biology*, **261**(1), 120–125.

Döring, B., Shynlova, O., Tsui, P., Eckardt, D., Janssen-Bienhold, U., Hofmann, F., Feil, S., Feil, R., Lye, S. J., and Willecke, K. 2006. Ablation of connexin43 in uterine smooth muscle cells of the mouse causes delayed parturition. *Journal of Cell Science*, **119**(9), 1715–1722.

Downing, S. J. and Sherwood, O. D. 1985a. The physiological role of relaxin in the pregnant rat. I. The influence of relaxin on parturition. *Endocrinology*, **116**, 1200–1205.

Downing, S. J. and Sherwood, O. D. 1985b. The physiological role of relaxin in the pregnant rat. II. The influence of relaxin on uterine contractile activity. *Endocrinology*, **116**, 1206–1214.

Downing, S. J. and Sherwood, O. D. 1985c. The physiological role of relaxin in the pregnant rat. III. The influence of relaxin on cervical extensibility. *Endocrinology*, **116**, 1215–1220.

Dreizen, P., Herman, L., and Berger, J. E. 1984. Structural studies of glycerinated skeletal muscle. I. A-band length and cross-bridge period in ATP-contracted fibers. *Advances in Experimental Medicine and Biology*, **170**, 135–155.

Duquette, R. A., Shmygol, A., Vaillant, C., Mobasheri, A., Pope, M., Burdyga, T., and Wray, S. 2005. Vimentin-positive, c-kit-negative interstitial cells in human and rat uterus: a role in pacemaking? *Biology of Reproduction*, **72**, 276–283.

Eddinger, T. J. and Meer, D. P. 2001. Single rabbit stomach smooth muscle cell myosin heavy chain SMB expression and shortening velocity. *American Journal of Physiology – Cell Physiology*, **280**, C309–C316.

Elfgang, C., Eckert, R., Lichtenberg-Fraté, H., Butterweck, A., Traub, O., Klein, R. A., Hülser, D. F., and Willecke, K. 1995. Specific permeability and selective formation of gap junction channels in connexin-transfected HeLa cells. *The Journal of Cell Biology*, **129**(3), 805–817.

Exton, J. H. 1996. Regulation of phosphoinositide phospholipases by hormones, neurotransmitters, and other agonists linked to G proteins. *Annual Reviews of Pharmacology and Toxicology*, **36**, 481–509.

Fan, Z. and Makielski, J. C. 1997. Anionic phospholipids activate ATP-sensitive potassium channels. *The Journal of Biological Chemistry*, **272**, 5388–5395.

Fatt, P. and Ginsborg, B. L. 1958. The ionic requirements for the production of action potentials in crustacean muscle fibres. *Journal of Physiology*, **142**, 516–543.

Fatt, P. and Katz, B. 1953. The electrical properties of crustacean muscle fibres. *Journal of Physiology*, **120**(1–2), 171–204.

Feldhamer, G. A., Drickamer, L. C., Vessey, S. H., Merritt, J. F., and Krajewski, C. 2007. *Mammalogy: Adaptation, Diversity, and Ecology*. Maryland, USA: The Johns Hopkins University Press.

Fishman, M. C. and Spector, I. 1981. Potassium current suppression by quinidine reveals additional calcium currents in neuroblastoma cells. *Proceedings of the National Academy of Sciences USA*, **78**, 5245–5249.

FitzHugh, R. 1960. Thresholds and plateaus in the Hodgkin-Huxley nerve equations. *The Journal of General Physiology*, **43**, 867–896.

FitzHugh, R. 1961. Impulses and physiological states in theoretical models of nerve membrane. *Biophysical Journal*, **1**, 445–466.

Fox, A. P., Hirning, L. D., Mogul, D. J., Artalejo, C. R., Penington, N. J., Scroggs, R. S., and MIller, R. J. 1991. *Calcium channels: Their properties, functions, regulation, and clinical relevance*. Florida, USA: CRC Press. Modulation of calcium channels by neurotransmitters, hormones and second messengers.

Frank, M., Wirth, A., Andrié, R. P., Kreuzberg, M. M., Dobrowolski, R., Seifert, G., Offermans, S., Nickenig, F., Willecke, K., and Schrickel, J. W. 2012. Connexin45 provides optimal atrioventricular nodal conduction in the adult mouse heart. *Circulation Research*, **111**(12), 1528–1538.

Fuchs, A.-R. 1978. Hormonal control of myometrial function during pregnancy and parturition. *Acta Obstetricia et Gynecologica Scandinavica*, **221**, 1–70.

Fuchs, A-R. 1983. The role of oxytocin in parturition. *Current Topics in Experimental Endocrinology*, **4**, 231–265.

Fuchs, A.-R., Fuchs, F., Hurstein, P., Soloff, M. S., and Fernstrom, M. J. 1982. Oxytocin receptors and human parturition: a dual role for oxytocin in the initiation of labor. *Science*, **215**, 1396–1398.

Gadsby, D. C. 2009. Ion channels versus ion pumps: the principal differences. *Nature Reviews in Molecular Cell Biology*, **10**(5), 344–352.

Gaide Chevronnay, H. P., Galant, C., and Lemoine, P. 2009. Spatiotemporal coupling of focal extracellular matrix degradation and reconstruction in the menstrual human endometrium. *Endocrinology*, **150**, 5094–5105.

Garfield, R. E. 1980. Gap junction formation in myometrium: control by estrogens, progesterone, and prostaglandins. *American Journal of Physiology*, **238**, C81–C89.

Garfield, R. E. 1986. Structural studies of innervation on nonpregnant rat uterus. *American Journal of Physiology*, **252**, C41–C54.

Garfield, R. E. and Hayashi, R. H. 1981. Appearance of gap junctions in the myometrium of women during labor. *American Journal of Obstetrics & Gynecology*, **140**(3), 958–959.

Garfield, R. E. and Maner, W. L. 2007. Physiology and electrical activity of uterine contractions. *Seminars in Cell & Developmental Biology*, **18**(3), 289–294.

Garfield, R. E., Sims, S., and Daniel, E. E. 1977. Gap junctions: their presence and necessity in myometrium during parturition. *Science*, **198**, 958–960.

Garfield, R. E., Sims, S. M., Kannan, M. S., and Daniel, E. E. 1978. Possible role of gap junctions in activation of myometrium during parturition. *American Journal of Physiology*, **235**, C168–C179.

Garfield, R. E., Blennerhassett, M. G., and Miller, S. M. 1988. Control of myometrial contractility: role and regulation of gap junctions. *Oxford Reviews of Reproductive Biology*, **10**, 436–490.

Garfield, R. E., Saade, G., Buhimschi, C., Buhimschi, I., Shi, L., Shi, S-Q., and Chwalisz, K. 1998. Control and assessment of the uterus and cervix during pregnancy and labour. *Human Reproduction Update*, **4**, 673–695.

Gartner, L. P. and Hiatt, J. L. 2009. *Color Atlas of Histology*. 5th edn. Maryland, USA: Lippincott Williams & Wilkins.

Gellersen, B. and Brosens, J. J. 2003. Cyclic AMP and progesterone receptor cross-talk in human endometrium: a decidualizing affair. *Journal of Endocrinology*, **178**, 357–372.

Gellersen, B., Brosens, I. A., and Brosens, J. J. 2007. Decidualization of the human endometrium: mechanisms, functions, and clinical perspectives. *Seminars in Reproductive Medicine*, **25**, 445–453.

Gerhardt, M., Schuster, H., and Tyson, J. 1990a. A cellular automaton model of excitable media including curvature and dispersion. *Science*, **247**(4950), 1563–1566.

Gerhardt, M., Schuster, H., and Tyson, J. 1990b. A cellular automaton model of excitable media. II. Curvature, dispersion, rotation waves and meandering waves. *Physica D*, **46**(3), 392–415.

Gerhardt, M., Schuster, H., and Tyson, J. 1990c. A cellular automaton model of excitable media. III. Fitting the Belousov-Zhabotinskii reaction. *Physica D*, **46**(3), 416–426.

Gerhardt, M., Schuster, H., and Tyson, J. 1991. A cellular automaton model of excitable media. IV. Untwisted scroll rings. *Physica D*, **50**(2), 189–206.

Gibbs, R., Weinstock, G., Metzker, M., Muzny, D., Sodergren, E. J., Scherer, S., Scott, G., Steffen, D., Worley, K. C., Burch, P. E., *et al.* 2004. Genome sequence of the Brown Norway rat yields insights into mammalian evolution. *Nature*, **428**(6982), 493–521.

Gillespie, A., Brummer, H. C., and Chard, T. 1972. Oxytocin release by infused prostaglandin. *British Medical Journal*, **1**, 543–544.

Goerttler, K. 1968. Die Struktur der Wand des menschlichen Uterus. *Archiv für Gynäkologie*, **205**, 334–342.

Goldman, D. E. 1943. Potential, impedance, and rectification in membranes. *The Journal of General Physiology*, **27**(1), 37–60.

Gourdie, R. G. and Lo, C. W. 1999. Cx43 (α1) gap junctions in cardiac development and disease. *Current Topics in Membranes*, **49**, 581–602.

Grazzini, E., Guillon, G., Mouillac, B., and Zingg, H. H. 1998. Inhibition of oxytocin receptor function by direct binding of progesterone. *Nature*, **392**, 509–512.

Grosset, A. and Mironneau, J. 1977. An analysis of the actions of prostaglandin E_1 on membrane currents and contraction in uterine smooth muscle. *Journal of Physiology*, **270**, 765–784.

Gu, Z. F., Jensen, R. T., and Maton, P. N. 1992. A primary role for protein kinase A in smooth muscle relaxation induced by adrenergic agonists and neuropeptides. *American Journal of Physiology*, **263**, G360–G364.

Guharay, F. and Sachs, F. 1984. Stretch-activated single ion channel currents in tissue-cultured embryonic chick skeletal muscle. *Journal of Physiology*, **352**, 685–701.

Hagiwara, S., Ozawa, S., and Sand, O. 1975. Voltage clamp analysis of two inward current mechanisms in the egg cell membrane of a starfish. *The Journal of General Physiology*, **65**, 617–644.

Harris, A. L., Spray, D. C., and Bennett, M. V. L. 1981. Kinetic properties of a voltage-dependent junctional conductance. *Science*, **77**(1), 95–117.

Helguera, G., Olcese, R., Song, M., Toro, L., and Stefani, E. 2002. Tissue-specific regulation of Ca^{2+} channel protein expression by sex hormones. *Biochimica et Biophysica Acta*, **1569**, 59–66.

Hendrix, E. M., Mao, S. J. T., Everson, W., and Larsen, W. J. 1992. Myometrial connexin 43 trafficking and gap junction assembly at term and preterm labor. *Molecular Reproduction and Development*, **33**(1), 27–38.

Hilgemann, D. W. and Ball, R. 1996. Regulation of cardiac Na^+, Ca^{2+} exchange and K_{ATP} potassium channels by PIP_2. *Science*, **273**, 956–959.

Hille, B. 1992. *Ionic Channels of Excitable Membranes*. 2^{nd} edn. Sinauer Associates, Inc.

Hodgkin, A. L. and Huxley, A. F. 1952a. Currents carried by sodium and potassium ions through the membrane of the giant axon of *Loligo*. *Journal of Physiology*, **116**(4), 449–472.

Hodgkin, A. L. and Huxley, A. F. 1952b. The components of membrane conductance in the giant axon of *Loligo*. *Journal of Physiology*, **116**(4), 473–496.

Hodgkin, A. L. and Huxley, A. F. 1952c. The dual effect of membrane potential on sodium conductance in the giant axon of *Loligo*. *Journal of Physiology*, **116**(4), 497–506.

Hodgkin, A. L. and Huxley, A. F. 1952d. A quantitative description of membrane current and its application to conduction and excitation in nerve. *Journal of Physiology*, **177**(4), 500–544.

Hodgkin, A. L. and Katz, B. 1949. The effect of sodium ions on the electrical activity of the giant axon of the squid. *Journal of Physiology*, **108**(1), 37–77.

Hodgkin, A. L., Huxley, A. F., and Katz, B. 1952. Measurement of current-voltage relations in the membrane of the giant axon of *Loligo*. *Journal of Physiology*, **116**(4), 424–448.

Howland, R. B. 1916. On the effect of removal of the pronephros of the amphibian embryo. *Proceedings of the National Academy of Sciences USA*, **2**, 231–234.

Inoue, Y., Nakao, K., Okabe, K., Izumi, H., Kanda, S., Kitamura, K., and Kuriyama, H. 1990. Some electrical properties of human pregnant myometrium. *American Journal of Obstetrics & Gynecology*, **162**, 1090–1098.

Ito, A., Hiro, D., Sakyo, K., and Mori, Y. 1987. The role of leukocyte factors on uterine cervical ripening and dilation. *Biology of Reproduction*, **37**, 511–517.

Izumi, H. 1985. Changes in the mechanical properties of the longitudinal and circular muscle tissues of the rat myometrium during gestation. *British Journal of Pharmacology*, **86**, 247–257.

Izumi, H., Yallampalli, C., and Garfield, R. E. 1993. Gestational changes in L-arginine-induced relaxation of pregnant rat and human myometrial smooth muscle. *American Journal of Obstetrics & Gynecology*, **169**, 1327–1337.

Ji, G., Barsotti, R. J., Feldman, M. E., and Kotlikoff, M. I. 2002. Stretch-induced calcium release in smooth muscle. *The Journal of General Physiology*, **119**, 533–544.

Kalkhoven, E., Wissik, S., van der Saag, P. T., and van der Burg, B. 1996. Negative interaction between the RelA(p65) subunit of NF-kappaB and the progesterone receptor. *The Journal of Biological Chemistry*, **271**, 6217–6224.

Kao, C. Y. 1959. Long-term observations of spontaneous electrical activity of the uterine smooth muscle. *American Journal of Physiology*, **196**, 343–350.

Karalis, K., Goodwin, G., and Majzoub, J. A. 1996. Cortisol blockade of progesterone: a possible molecular mechanisms involved in the initiation of human labor. *Nature Medicine*, **2**, 556–560.

Kawarabayashi, T. and Marshall, J. M. 1981. Factors influencing circular muscle activity in the pregnant rat uterus. *Biology of Reproduction*, **24**, 373–379.

Kawarabayashi, T. and Osa, T. 1976. Comparative investigations of alpha- and beta-effects on the longitudinal and circular muscles of the pregnant rat myometrium. *The Japanese Journal of Physiology*, **26**, 403–416.

Keelan, J. A., Coleman, M., and Mitchell, M. D. 1997. The molecular mechanisms of term and preterm labor: recent progress and clinical implications. *Clinical Obstetrics and Gynecology*, **40**, 460–478.

Keener, J. and Sneyd, J. 2004. *Mathematical Physiology*. New York, USA: Springer.

Kelly, R. W. 1994. Pregnancy maintenance and parturition: the role of prostaglandin in manipulating the immune and inflammatory response. *Endocrine Reviews*, **15**, 684–706.

Kelly, R. W., Illingworth, P., Baldie, G., Leask, R., Brouwer, S., and Calder, A. A. 1993. Progesterone control of interleukin-8 production in endometrium and chorio-decidual cells underlies the role of the neutrophil in menstruation and parturition. *Human Reproduction*, **9**, 253–258.

Khan, K. S., Wojdyla, D., Say, L., Gülmezoglu, A. M., and Van Look, P. F. 2006. WHO analysis of causes of maternal death: A systematic review. *The Lancet*, **367**, 1066–1074.

Kieler, H., Axelsson, O., Nilsson, S., and Waldenström, U. 1995. The length of human pregnancy as calculated by ultrasonographic measurement of the fetal biparietal diameter. *Ultrasound in Obstetrics and Gynecology*, **6**(5), 353–357.

Kilarski, W. M., Semik, D., Roomans, G. M., Ulmsten, U., and Severs, N. J. 1998. Immunohistochemical analysis of connexins 26, 32 and 43 in rat uterus during late pregnancy: lack of connexin 26 in the myometrium. *The Histochemical Journal*, **30**, 307–316.

Kilarski, W. M., Rothery, S., Roomans, G. M., Ulmsten, U., Rezapour, M., Stevneson, S., Coppen, S. R., Dupont, E., and Severs, N. J. 2001. Multiple connexins localized to individual gap-junctional plaques in human myometrial smooth muscle. *Microscopy Research and Technique*, **54**(2), 114–122.

Kim, D., Pertea, G., Trapnell, C., Pimentel, H., Kelley, R., and Salzberg, S. L. 2013. TopHat2: accurate alignment of transcriptomes in the presence of insertions, deletions and gene fusions. *Genome Biology*, **14**(4), R36.

Kishikawa, T. 1981. Alterations in the properties of the rat myometrium during gestation and post partum. *The Japanese Journal of Physiology*, **31**, 515–536.

Kokorine, I., Marbaix, E., Henriet, P., Okada, Y., Donnez, J., Eeckhout, Y., and Courtoy, P. J. 1996. Focal cellular origin and regulation of interstitial collagenase (matrix metalloproteinase-1) are related to menstrual breakdown in the human endometrium. *Journal of Cell Science*, **109**, 2151–2160.

Krüger, O., Plum, A., Kim, J-S., Winterhager, E., Maxeiner, S., Hallas, S., Kirchhoff, S., Traub, O., Lamers, W. H., and Willecke, K. 2000. Defective vascular development in connexin 45-deficient mice. *Development*, **127**(19), 4179–4193.

Kumai, M., Nishii, K., Nakamura, J. I., Takeda, N., Suzuki, M., and Shibata, Y. 2000. Loss of connexin45 causes a cushion defect in early cardiogenesis. *Development*, **127**(16), 3501–3512.

Kumar, D. and Barnes, A. C. 1961. Studies in human myometrium during pregancy. II. Resting membrane potential and comparative electrolyte levels. *American Journal of Obstetrics & Gynecology*, **82**, 736–741.

Kumar, N. M. and Gilula, N. B. 1996. The gap junction communication channel. *Cell*, **84**(3), 381–388.

Kuriyama, H. and Suzuki, H. 1976. Changes in electrical properties of rat myometrium during gestation and following hormonal treatements. *Journal of Physiology*, **260**, 315–333.

Laforet, J., Rabotti, C., Terrien, J., Mischi, M., and Marque, C. 2011. Toward a multiscale model of the uterine electrical activity. *IEEE Transactions on Biomedical Engineering*, **58**(12), 3487–3490.

Laird, D. W. 2006. Life cycle of connexins in health and disease. *Biochemical Journal*, **15**(394 (Pt. 3)), 527–543.

Leppert, P. C. 1992. Cervical softening, effacement and dilation: a complex biochemical cascade. *Journal of Maternal-Fetal and Neonatal Medicine*, **1**, 213–223.

Leppert, P. C. 1995. Anatomy and physiology of cervical ripening. *Clinical Obstetrics and Gynecology*, **38**, 267–279.

Li, H., Handsaker, B., Wysoker, A., Fennell, R., Ruan, J., Homer, N., Marth, G., Abecasis, G, Burbin, R., and Subgroup, 1000 Genome Project Data Processing. 2009. The sequence alignment/map format and SAMtools. *Bioinformatics*, **25**, 2078–2079.

Li, L., Zhang, Y., and Zhou, C. 2012. Phosphorylation of h1 Calponin by PKC epsilon may contribute to facilitate the contraction of uterine myometrium during pregnancy and labor. *Reproductive Biology and Endocrinology*, **10**, 1–8.

Liu, Y., Gold, E. B., Lasley, B. L., and Johnson, W. O. 2004. Factors affecting menstrual cycle characteristics. *American Journal of Epidemiology*, **160**(2), 131–140.

Lodge, S. and Sproat, J. E. 1981. Resting membrane potentials of pacemaker and non pacemaker areas in rat uterus. *Life Sciences*, **28**, 2251–2256.

Logothetis, D. E., Jin, T., Lupyan, D., and Rosenhouse-Dantsker, A. 2007. Phosphoinositide-mediated gating of inwardly rectifying K^+ channels. *Pflügers Archiv – European Journal of Physiology*, **455**, 83–95.

Lüking Jayes, F. C., Britt, J. H., and Esbenshade, K. L. 1997. Role of gonadotropin-releasing hormone pulse frequency in differential regulation of gonadotropins in the gilt. *Biology of Reproduction*, **56**, 1012–1019.

Lye, S. J., Ou, C-W., Teoh, T-G., Erb, G., Stevens, Y., Casper, R., Patel, F. A., and Challis, J. R. G. 1998. The molecular basis of labour and tocolysis. *Fetal and Maternal Medicine Review*, **10**(3), 121–136.

Macdonald, S. and Magill-Cuerden, J. (eds). 2011. *Mayes' Midwifery.* 14$^{\text{th}}$ edn. Philadelphia: Baillière Tindall.

Maeda, K. 2013. Uterine contractions in normal labor developed by a positive feed-back and oscillation. *Journal of Health & Medical Informatics*, **4**(3), 130.

Magann, E. F., Evans, S., Chauhan, S. P., Lanneau, G., Fisk, A. D., and Morrison, J. C. 2005. The length of the third stage of labor and the risk of postpartum hemorrhage. *Obstetrics & Gynecology*, **105**(2), 290–293.

Marbaix, E., Kokorine, I., and Henriet, P. 1995. The expression of interstitial collagenase in human endometrium is controlled by progesterone and by oestradiol and is related to menstruation. *Biochemical Journal*, **305**, 1027–1030.

Marbaix, E., Kokorine, I., Moulin, P., Donnez, J., Eeckhout, Y., and Courtoy, P. J. 1996. Menstrual breakdown of human endometrium can be mimicked *in vitro* and is selectively and reversibly blocked by inhibitors of matrix metalloproteinases. *Proceedings of the National Academy of Sciences USA*, **93**, 9120–9125.

Markus, M. and Hess, B. 1990. Isotropic cellular automaton for modeling excitable media. *Nature*, **347**, 56–58.

Marshall, J. C., Dalkin, A. C, Haisenleder, D .J., Griffin, M. L., and Kelch, R. P. 1993. GnRH pulses—the regulators of human reproduction. *Transitions of the American Clinical and Climatological Association*, **104**, 31–46.

Marshall, J. M. 1962. Regulation of activity in uterine smooth muscle. *Physiological Reviews Supplement*, **5**, 213–227.

Marshall, J. M. 1981. Effects of ovarian steroids and pregnancy on adrenergic nerves of uterus and oviduct. *American Journal of Physiology*, **240**, C165–C174.

Marshall, J. M. and Kroeger, E. A. 1973. Adrenergic influences on uterine smooth muscle. *Philosophical Transactions of the Royal Society B*, **265**, 135–148.

Martinac, B. 2011. Bacterial mechanosensitive channels as a paradigm for mechanosensory transduction. *Cellular Physiology and Biochemistry*, **28**, 1051–1060.

Martinez, A. D., Hayrapetyan, V., Moreno, A. P., and Beyer, E. C. 2002. Connexin43 and connexin45 form heteromeric gap junction channels in which individual components determine permeability and regulation. *Circulation Research*, **90**(10), 1100–1107.

Matlib, M. A., Crankshaw, J., Garfield, R. E., Crankshaw, D. J., Kwan, C. Y., Branda, L., and Daniel, E. E. 1979. Characterization of membrane fractions and isolation of plasma membrane from rat myometrium. *The Journal of Biological Chemistry*, **254**, 1834–1840.

Matthew, A., Shmygol, A., and Wray, S. 2004. Ca^{2+} entry, efflux and release in smooth muscle. *Biological Research*, **37**(4), 617–624.

McCloskey, C., Rada, C., Bailey, E., McCavera, S., van den Berg, H. A., Atia, J., Rand, D. A., Shmygol, A., Chan, Y-W., Quenby, S., *et al.* 2014. The inwardly rectifying K^+ channels Kir7.1 controls uterine excitability throughout pregnancy. *EMBO Molecular Medicine*, **6**, 1161–1174.

McLaren, W. J., Young, I. R., and Rice, G. E. 1996. *Advances in Organ Biology: Pregnancy and Parturition*. Vol. 1. Elsevier. Late pregnancy and parturition in the sheep, pp. 1–29.

Means, A. R., Bagchi, I. C., VanBerkum, M. F., and Kemp, B. E. 1991. Regulation of smooth muscle myosin light chain kinase by calmodulin. *Advances in Experimental Medicine and Biology*, **304**, 11–24.

Mendelson, C. R. and Condon, J. C. 2005. New insights into the molecular endocrinology of parturition. *The Journal of Steroid Biochemistry and Molecular Biology*, **93**, 113–119.

Miller, S. M., Garfield, R. E., and Daniel, E. E. 1989. Improved propagation in myometrium associated with gap junctions during parturition. *American Journal of Physiology*, **256**, C130–C131.

Mironneau, J. 1976. Effects of oxytocin on ionic currents underlying rhythmic activity and contraction in uterine smooth muscle. *Pflügers Archiv – European Journal of Physiology*, **363**, 113–118.

Mitchell, B. S. and Peel, S. 2009. *Histology: an illustrated colour text*. London, U.K.: Churchill Livingstone, Elsevier.

Miyoshi, H., Boyle, M., MacKay, L., and Garfield, R. E. 1996. Voltage-clamp studies of gap junctions between uterine muscle cells during term and preterm labor. *Biophysical Journal*, **71**, 1324–1334.

Moreno, A. P., Fishman, G. I., and Spray, D. C. 1992. Phosphorylation shifts unitary conductance and modifies voltage-dependent kinetics of human connexin43 gap junction channels. *Biophysical Journal*, **62**(1), 51–53.

Moreno, A. P., Laing, J. G., Beyer, E. C., and Spray, D. C. 1995. Properties of gap junction channels formed of connexin 45 endogenously expressed in human hepatoma (SKHep1) cells. *American Journal of Physiology – Cell Physiology*, **268**(2), C366–C365.

Morgan, K. 1990. The role of calcium in the control of vascular tone as assessed by the Ca^{2+} indicator Aequorin. *Cardiovascular Drugs and Therapy*, **4**, 1355–1362.

Morris, C. and Lecar, H. 1981. Voltage oscillations in the barnacle giant muscle fiber. *Biophysical Journal*, **35**(1), 193–213.

Mueller, A., Maltaris, T., Siemer, J., Binder, H., Hoffmann, I., Beckmann, M. W., and Dittrich, R. 2006. Uterine contractility in response to different prostaglandins: results from extracorporeally perfused non-pregnant swine uteri. *Human Reproduction*, **21**, 2000–2005.

Muhammad, S. I., Ismail, M., Mahmud, R. B., Salisu, A. M., and Zakaria, Z. A. 2013. Germinated brown rice and its bioactives modulate the activity of uterine cells in oophorectomised rats as evidenced by gross cytohistological and immunohistochemical changes. *BMC Complementary and Alternative Medicine*, **13**, 1–9.

Nagumo, J., Arimoto, S., and Yoshizawa, S. 1962. An active pulse transmission line simulating nerve axon. *Proceedings of the IEEE*, **50**, 2061–2070.

Office for National Statistics. 2009 (Last retrieved: 20 August 2014). *Gestation-specific infant mortality in England and Wales – 2006*. `http://www.ons.gov.uk/ons/dcp171778_229489.pdf`.

O'Grady, J. P., Kohorn, E. I., Glass, R. H., Caldwell, B. V., Brock, W. A., and Speroff, L. 1972. Inhibition of progesterone synthesis *in vitro* by prostaglandin $F_{2\alpha}$. *Journal for the Society for Reproduction and Fertility*, **30**, 153–156.

Osa, T. and Watanabe, M. 1978. Effects of catecholamines on the circular muscle of rat myometria at term during pregnancy. *The Japanese Journal of Physiology*, **28**, 647–658.

Osmers, R., Rath, W., Adelmann-Grill, B. C., Fittkow, C., Kuloczik, M., Szeverényi, M., Tschesche, H., and Kuhn, W. 1992. Origin of cervical collagenase during parturition. *American Journal of Obstetrics & Gynecology*, **166**, 1455–1460.

Ottesen, B. 1981. Vasoactive intestinal polypeptide (VIP): effect on rabbit uterine smooth muscle *in vivo* and *in vitro*. *Acta Physiologica Scandinavica*, **113**, 193–199.

Ottesen, B., Larsen, J. J., Fahrenkrug, J., Stjernquist, M., and Sundler, F. 1981. Distribution and motor effect of VIP in female genital tract. *American Journal of Physiology*, **240**, E32–E36.

Ottesen, B., Ulrichsen, H., Fahrenkrug, J., Larsen, J. J., Wagner, G., Schierup, L., and Søndergaard, F. 1982. Vasoactive intestinal polypeptide and the female genital tract: relationship to reproductive phase and delivery. *American Journal of Obstetrics & Gynecology*, **143**, 414–420.

Ottesen, B., Gram, B. R., and Fahrenkrug, J. 1983. Neuropeptides in the female genital tract: effect on vascular and non-vascular smooth muscle. *Peptides*, **4**, 387–392.

Owman, C., Rosenbren, E., and Sjöberg, N. O. 1967. Adrenergic innervation of the human female reproductive organs: a histochemical and chemical investigation. *Obstetrics & Gynecology*, **30**, 763–773.

Pansky, B. 1982. *Review of Medical Embryology*. New York, USA: Macmillan.

Parkington, H. C., Tonta, M. A., Brennecke, S. P., and Coleman, H. A. 1999a. Contractile activity, membrane potential, and cytoplasmic calcium in human uterine smooth muscle in the third trimester of pregnancy and during labor. *American Journal of Obstetrics & Gynecology*, **181**(6), 1445–1451.

Parkington, H. C., Tonta, M. A., Davies, N. K., Brennecke, S. P., and Coleman, H. A. 1999b. Hyperpolarization and slowing of the rate of contraction in human uterus in pregnancy by prostaglandins E_2 and $F_{2\alpha}$: involvement of the Na^+ pump. *Journal of Physiology*, **514**(1), 229–243.

Patel, A., Sharif-Naeini, R., Folgering, J. R., Bichet, D., Duprat, F., and Honoré, E. 2010. Canonical TRP channels and mechanotransduction: from physiology to disease states. *Pflügers Archiv – European Journal of Physiology*, **460**, 571–581.

Patro, R., Mount, S. M., and Kingsford, C. 2013. Sailfish enables alignment-free isoform quantification from RNA-seq reads using lightweight algorithms. *Nature Biotechnology*, **32**, 462–464.

Petrocelli, T. and Lye, S. J. 1993. Regulation of transcripts encoding the myometrial gap junction protein, connexin-43, by estrogen and progesterone. *Endocrinology*, **133**, 283–290.

Plonsey, R. and Barr, R. C. 2007. *Bioelectricity: A Quantitative Approach*. 3rd edn. Berlin, Germany: Springer Science & Business Media.

Porter, D. G., Downing, S. J., and Bradshaw, J. M. 1979. Relaxin inhibits spontaneous and prostaglandin-driven myometrial activity in anaesthetized rats. *Journal of Endocrinology*, **83**, 183–192.

Pressman, E. K., Tucker, A. J., Anderson, N. C., and Young, R. C. 1988. Morphologic and electrophysiologic characterization of isolated pregnant human myometrial cells. *American Journal of Obstetrics & Gynecology*, **159**(5), 1273–1279.

Putz, R. and Pabst, R. 1989. *Sobotta - Atlas of Human Anatomy*. 14th edn. Munich: Elsevier.

Rae, J., Cooper, K., and Gates, P. 1991. Low access resistance perforated patch recordings using amphotericin B. *Journal of Neuroscience Methods*, **37**(1), 15–26.

Ramón, F., Anderson, N. C., Joyner, R. W., and Moore, J. W. 1976. A model for propagation of action potentials in smooth muscle. *Journal of Theoretical Biology*, **59**(2), 381–408.

Rechnerger, T., Abramson, S. R., and Woessner Jr., J. F. 1996. Onapristone and prostaglandin E2 induction of delivery in the rat in late pregnancy: a model for the analysis of cervical softening. *American Journal of Obstetrics & Gynecology*, **175**, 719–723.

Reimer, R. K., Goldfien, A. C., Goldfien, A., and Roberts, J. M. 1986. Rabbit uterine oxytocin receptors and *in vitro* contractile response: abrupt changes at term and the role of eicosanoids. *Endocrinology*, **119**, 699–709.

Reiner, O. and Marshall, J. M. 1976. Action of prostaglandin, $PGF_{2\alpha}$, on the uterus of the pregnant rat. *Naunyn-Schmiedeberg's Archives of Pharmacology*, **292**, 243–250.

Rihana, S., Terrien, J., Germain, G., and Marque, C. 2008. Mathematical modeling of electrical activity of uterine muscle cells. *Medical & Biological Engineering & Computing*, **47**(6), 665–675.

Ringer, S. 1882a. Concerning the influence exerted by each of the constituents of the blood on the contraction of the ventricle. *Journal of Physiology*, **3**(5–6), 380–393.

Ringer, S. 1882b. Regarding the action of hydrate of soda, hydrate of ammonia, and hydrate of potash on the ventricle of the frog's heart. *Journal of Physiology*, **3**(3–4), 195–202.

Ringer, S. 1883a. A further contribution regarding the influence of the different constituents of the blood on the contraction of the heart. *Journal of Physiology*, **4**(1), 29–42.

Ringer, S. 1883b. A third contribution regarding the influence of the inorganic constituents of the blood on the ventricular contraction. *Journal of Physiology*, **4**(2–3), 222–225.

Ringer, S. 1884. An investigation regarding the action of rubidium and cæsium salts compared with the action of potssium salts on the ventricle of the frog's heart. *Journal of Physiology*, **4**(6), 370–379.

Risek, B., Guthrie, S., Kumar, N., and Gilula, N. B. 1990. Modulation of gap junction transcript and protein expression during pregnancy in the rat. *The Journal of Cell Biology*, **110**(2), 269–282.

Rosa, P. S. La, Eswaran, H., Preissl, H., and Nehoraj, A. 2012. Multiscale forward electromagnetic model of uterine contractions during pregnancy. *BMC Medical Physics*, **12**(4), 1–16.

Sadler, T. W. 2012. *Langman's Medical Embryology*. 12$^{\text{th}}$ edn. Maryland, USA: Lippincott Williams & Wilkins.

Sakai, K., Yamaguchi, T., and Uchida, M. 1981. Oxytocin-induced Ca-free contraction of rat uterine smooth muscle: effects of divalent cations and drugs. *Achives Internationales de Pharmacodynamie et de Thérapie*, **250**, 40–54.

Sanborn, B. M., Kuo, H. S., Weisbrodt, N. W., and Sherwood, O. D. 1980. The interaction of relaxin with the rat uterus. I. Effect on cyclic nucleotide levels and spontaneous contractile activity. *Endocrinology*, **106**(4), 1210–1215.

Sanfillipo, J. S., Teichman, K., Melvin, T. R., Osyamkpe, J. L., and Wittliff, J. H. 1983. The influence of certain prostaglandin synthetase inhibitors on cytoplasmic estrogen receptors in the uterus. *American Journal of Obstetrics & Gynecology*, **145**, 100–104.

Schoenwolf, G. C., Bleyl, S. B., Brauer, P. R., and Francis-West, P. H. 2008. *Larsen's Human Embryology*. 4th edn. Amsterdam, Netherlands: Elsevier.

Sheldon, R. E., Baghdadi, M., McCloskey, C., Blanks, A. M., Shmygol, A., and van den Berg, H. A. 2013. Spatial heterogeneity enhances and modulates excitability in a mathematical model of the myometrium. *Journal of the Royal Society Interface*, **10**, 20130458.

Sheldon, R. E., Mashayamombe, C., Shi, S-Q., Garfield, R. E., Shmygol, A., Blanks, A. M., and van den Berg, H. A. 2014. Alterations in gap junction connexin43/connexin45 ratio mediate a transition from quiescence to excitation in a mathematical model of the myometrium. *Journal of the Royal Society Interface*, **11**, 20140726.

Sheldrick, E. L. and Flint, A. P. F. 1985. Endocrine control of uterine oxytocin receptors in the ewe. *Journal of Endocrinology*, **106**, 249–258.

Sherman, S. J., Greenspoon, J. S., Nelson, J. M., and Paul, R. H. 1992. Identifying the obstetric patient at high risk of multiple-unit blood transfusions. *The Journal of Reproductive Medicine*, **37**(7), 649–652.

Sherwood, O. D., Crnekovic, V. E., Gordon, W. L., and Rutherford, E. J. 1980. Radioimmunoassay of relaxin throughout pregnancy and during parturition in the rat. *Endocrinology*, **107**, 691–698.

Shynlova, O., Kwong, R., and Lye, S. J. 2010. Mechanical stretch regulates hypertrophic phenotype of the myometrium during pregnancy. *Reproduction*, **139**, 247–253.

Sims, S. M., Daniel, E. E., and Garfield, R. E. 1982. Improved electrical coupling in uterine smooth muscle is associated with increased gap junctions at parturition. *The Journal of General Physiology*, **80**, 353–375.

Singer, S. J. and Nicolson, G. L. 1972. The fluid mosaic model of the structure of cell membranes. *Science*, **175**, 720–731.

Singh, R., Xu, J., Garnier, N. G., Pumir, A., and Sinha, S. 2012. Self-organized transition to coherent activity in disordered media. *Physical Review Letters*, **108**(6), 068102.

Skou, J. C. 1957. The influence of some cations on an adenosine triphosphate from peripheral nerves. *Biochimica et Biophysica Acta*, **23**(2), 394–401.

Smrcka, A. V., Hepler, J. R., Brown, K. O., and Sternweis, P. C. 1991. Regulation of polyphosphoinositide-specific phospholipase C activity by purified Gq. *Science*, **251**, 804–807.

Soloff, M. S., Alexandrova, M., and Fernstrom, M. J. 1979. Oxytocin receptors: triggers for parturition and lactation? *Science*, **204**, 1313–1315.

Soloff, M. S., Jeng, Y-J., Izban, M. G., Sinha, M., Luxon, B. A., Stamnes, S. J., and England, S. K. 2011. Effects of progesterone treatment on expression of genes involved in uterine quiescence. *Reproductive Sciences*, **18**, 781–797.

Somlyo, A. P., Wu, X., Lalker, L. A., and Somlyo, A. V. 1999. Pharmacomechanical coupling: the role of calcium, G-proteins, kinases and phosphatases. *Reviews of Physiology, Biochemistry and Pharmacology*, **134**, 201–234.

Somlyo, A. V. 1980. *Handbook of Physiology: Cardiovascular System*. Vol. 2. Baltimore, USA: Waverly Press Inc. Ultrastructure of vascular smooth muscle, pp. 33–67.

Sosinsky, G. 1995. Mixing of connexins in gap junction membrane channels. *Proceedings of the National Academy of Sciences USA*, **92**(20), 9210–9214.

Spray, D. C., Harris, A. L., and Bennett, M. V. L. 1979. Voltage-dependence of junctional conductance in early amphibian embryos. *Science*, **204**(4391), 432–434.

Spray, D. C., Harris, A. L., and Bennett, M. V. L. 1981. Equilibrium properties of a voltage-dependent junctional conductance. *The Journal of General Physiology*, **77**(1), 77–93.

Steinberg, B. E., Glass, L., Shrier, A., and Bub, G. 2006. The role of heterogeneities and intercellular coupling in wave propagation in cardiac tissue. *Philosophical Transactions of the Royal Society A*, **364**(1842), 1299–1311.

Stjernquist, M., Emson, P., Owman, C., Sjöberg, N. O., Sundler, F., and Tatemoto, K. 1983. Neuropeptide Y in the female reproductive tract of the rat. Distribution of nerve fibres and motor effects. *Neuroscience Letters*, **39**, 279–284.

Stjernquist, M., Ekblad, E., Owman, C., and Sundler, F. 1986. Neuronal localization and motor effects of gastrin-releasing peptide (GRP) in rat uterus. *Regulatory Peptides*, **13**, 197–205.

Stones, R. W., Paterson, C. M., and Saunders, N. J. 1993. Risk factors for major obstetric haemorrhage. *European Journal of Obstetrics & Gynecology and Reproductive Biology*, **48**(1), 15–18.

Sun, X., Perc, M., Lu, Q., and Kurths, J. 2008. Spatial coherence resonance on diffusive and small-world networks of Hodgkin-Huxley neurons. *Chaos*, **18**(2), 023102.

Tabb, T., Thilander, G., Grover, A., Hertzberg, E., and Garfield, R. E. 1992. An immunochemical and immunocytological study of the increase in myometrial gap junctions (and connexin 43) in rats and humans during pregnancy. *American Journal of Obstetrics & Gynecology*, **167**(2), 559–567.

Tai, C., de Groat, W. C., and Roppolo, J. R. 2005. Simulation of nerve block by high-frequency sinusoidal electrical current based on the Hodgkin-Huxley model. *IEEE Transactions of Neural Systems and Rehabilitation Engineering*, **13**(3), 415–422.

Thomson, A. J., Telfer, J. F., Young, A., Campbell, S., Stewart, C. J., Cameron, I. T., Greer, I. A., and Norman, J. E. 1999. Leukocytes infiltrate the myometrium during human parturition: further evidence that labor is an inflammatory process. *Human Reproduction*, **14**, 229–236.

Thorbert, G. 1978. Regional changes in structure and function of adrenergic nerves in guinea-pig uterus during pregnancy. *Acta Obstetricia et Gynecologica Scandinavica*, **57**, 2–32.

Thorburn, G. D. and Challis, J. R. G. 1979. Endocrine control of parturition. *Physiological Reviews*, **59**, 863–918.

Thorvaldsdóttir, H., Robinson, J. T., and Mesirov, J. P. 2012. Intergrative genomics viewer (IGV): high-performance genomics data visualization and exploration. *Briefings in Bioinformatics*, **14**(2), 178–192.

Tichenor, J. N., Hansen, E. T., and Buxton, I. L. 2005. Expression of stretch-activated potassium channels in human myometrium. *Proceedings of the Western Pharmacology Society*, **48**, 44–48.

Tong, D., Lu, X., Wang, H-W., Plante, I., Lui, E., Laid, D. W., Bai, D., and Kidder, G. M. 2009. A dominant loss-of-function GJA1 (Cx43) mutant impairs parturition in the mouse. *Biology of Reproduction*, **80**(6), 1099–1106.

Tong, W-C., Choi, C. Y., Karche, S., Holden, A. V., Zhang, H., and Taggart, M. J. 2011. A computational model of the ionic currents, Ca^{2+} dynamics and action potentials underlying contraction of isolated uterine smooth muscle. *PLoS One*, **6**(4), e18685.

Tribe, R. M., Moriarty, P., and Poston, L. 2000. Calcium homeostatic pathways change with gestation in human myometrium. *Biology of Reproduction*, **63**(3), 748–755.

Tytler, P., Ireland, J., and Fitches, E. 1996. A study of the structure and function of the pronephros in the larvae of the turbot (*Scophthalmus maximus*) and the herring (*Clupea harengus*). *Marine and Freshwater Behaviour and Physiology*, **28**, 3–18.

Ulmsten, U., Wingerup, L., Belfrage, P., Ekman, G., and Wiqvist, N. 1982. Intracervical application of prostaglandin gel for induction of term labor. *Obstetrics & Gynecology*, **59**, 336–339.

van den Berg, H. A. 2011. *Mathematical Models of Biological Systems*. Oxford, UK: Oxford University Press.

van Eldik, R. and Hubbard, C. D. (eds). 2009. *Advances in Inorganic Chemistry*. Vol. 61. Massachusetts, USA: Academic Press.

Veenstra, R. D., Wang, H-Z., Westphale, E. M., and Beyer, E. C. 1992. Multiple connexins confer distinct regulatory and conductance properties of gap junctions in developing heart. *Circulation Research*, **71**(5), 1277–1283.

Veenstra, R. D., Wang, H-Z., Beyer, E. C., and Bring, P. R. 1994. Selective dye and ionic permeability of gap junction channels formed by connexin45. *Circulation Research*, **75**(3), 483–490.

Verselis, Y. K., Ginter, C. S., and Bargiello, T. A. 1994. Opposite voltage gating polarities of two closely related connexins. *Nature*, **368**(6469), 348–351.

Villar, A., D'Ocon, M. P., and Anselmi, E. 1985. Calcium requirement of uterine contraction induced by PGE_1: importance of intracellular calcium stores. *Prostaglandins*, **30**, 491–496.

Vogel, R. and Weingart, R. 1998. Mathematical model of vertebrate gap junctions derived from electrical measurements on homotypic and heterotypic channels. *Journal of Physiology*, **510**(1), 177–189.

Wagner, G. P., Kin, K., and Lynch, V. J. 2012. Measurement of mRNA abundance using RNA-seq data: RPKM measure is inconsistent among samples. *Theory in Biosciences*, **131**(4), 281–285.

Wang, H-Z., Li, J., Lemanski, L. F., and Veenstra, R. D. 1992. Gating of mammalian cardiac gap junction channels by trans-junctional voltage. *Biophysical Journal*, **63**(1), 139–151.

Webb, R. C. 2003. Smooth muscle contraction and relaxation. *Advances in Physiology Education*, **27**, 201–206.

Weimar, J. R., Tyson, J. J., and Watson, L. T. 1992a. Diffusion and wave-propagation in cellular automaton models of excitable media. *Physica D*, **55**(3–4), 309–327.

Weimar, J. R., Tyson, J. J., and Watson, L. T. 1992b. Third generation cellular automaton for modeling excitable media. *Physica D*, **55**(3–4), 328–339.

Weiss, S., Jaermann, T., Schmid, P., Staempfli, P., Boesiger, P., Niederer, P., Caduff, R., and Bajka, M. 2006. Three-dimensional fiber architecture of the nonpregnant human uterus determined *ex vivo* using magnetic resonance diffusion tensor imaging. *The Anatomical Record Part A: Discoveries in Molecular, Cellular, and Evolutionary Biology*, **288A**, 84–90.

Wetzstein, R. and Renn, K. H. 1970. Zur Anordnung der glatten Muskulatur im Corpus Uteri des Menschen. *Verhandlungen der Anatomischen Gesellschaft*, **64**, 461–468.

Willecke, K., Eiberger, J., Degen, J., Eckardt, D., Romualdi, A., Güldenagel, M., Deutsch, U., and Söhl, G. 2002. Structural and functional diversity of connexin genes in the mouse and human genome. *The Journal of Biological Chemistry*, **383**(5), 725–737.

Wilson Jr., L. 1983. Effects of estradiol and progesterone on uterine prostaglandin levels in the pregnant rat. *Prostaglandins*, **26**(1), 47–54.

Winterhager, E., Stutenkemper, R., Traub, O., Beyer, E., and Willecke, K. 1991. Expression of different connexin genes in rat uterus during decidualization and at term. *European Journal of Cell Biology*, **55**(1), 133–142.

Wolfs, G. and Rottinghuis, H. 1970. Electrical and mechanical activity of the human uterus during labour. *Archiv für Gynäkologie*, **208**(4), 373–385.

Wolfs, G. M. J. A. and van Leeuwen, M. 1979. Electromyographic observations on the human uterus during labour. *Acta Obstetricia et Gynecologica Scandinavica*, **58**, 1–61.

Wood, N. S., Marlow, N., Costeloe, K., Chir, B., Gibson, A. T., and Wilkinson, A. R. 2000. Neurologic and developmental disability after extremely preterm birth. *New England Journal of Medicine*, **343**(6), 378–384.

World Health Organization. 2013 (Last retrieved: 6 August 2014). *Preterm birth statistics*. `www.who.int/mediacentre/factsheets/fs363/en/`.

Wray, S., Kupittayanant, S., Shmygol, A., Smith, R. D., and Burdyga, T. 2001. The physiological basis of uterine contractility: a short review. *Experimental Physiology*, **86**(2), 239–246.

Wulff, C., Dickson, S. E., Duncan, W. C., and Fraser, H. M. 2001. Angiogenesis in the human corpus luteum: simulated early pregnancy by HCG treatment is associated with both angiogenesis and vessel stabilization. *Human Reproduction*, **16**(12), 2515–2524.

Wuttke, W. 1987. *Human Physiology*. 2nd edn. Berlin, Germany: Springer.

Young, R. C. 2007. Myocytes, myometrium, and uterine contractions. *Annals of the New York Academy of Sciences*, **1101**, 72–84.

Zakar, T. and Hertelendy, F. 2007. Progesterone withdrawal: key to parturition. *American Journal of Obstetrics & Gynecology*, **196**(4), 289–296.

Zhang, A., Cheng, T. P., Altura, B. T., and Altura, B. M. 1992. Extracellular magnesium regulates intracellular free Mg^{2+} in vascular smooth muscle cells. *Pflügers Archiv – European Journal of Physiology*, **421**(4), 391–393.

Zhang, H. and Holden, A. V. 1995. Chaotic meander of spiral waves in the FitzHugh-Nagumo system. *Chaos, Solitons & Fractals*, **5**(34), 661–670.

Appendix A

Flow diagrams representing the structure of the simulations

The mathematical models were coded using Wolfram *Mathematica*. The flow diagrams presented below represent the procedures used in the simulations. The full, annotated *Mathematica* code can be found on my e-portfolio page at the website below.

`go.warwick.ac.uk/rachelsheldon/simulationcode`

A.1 Fully connected lattice

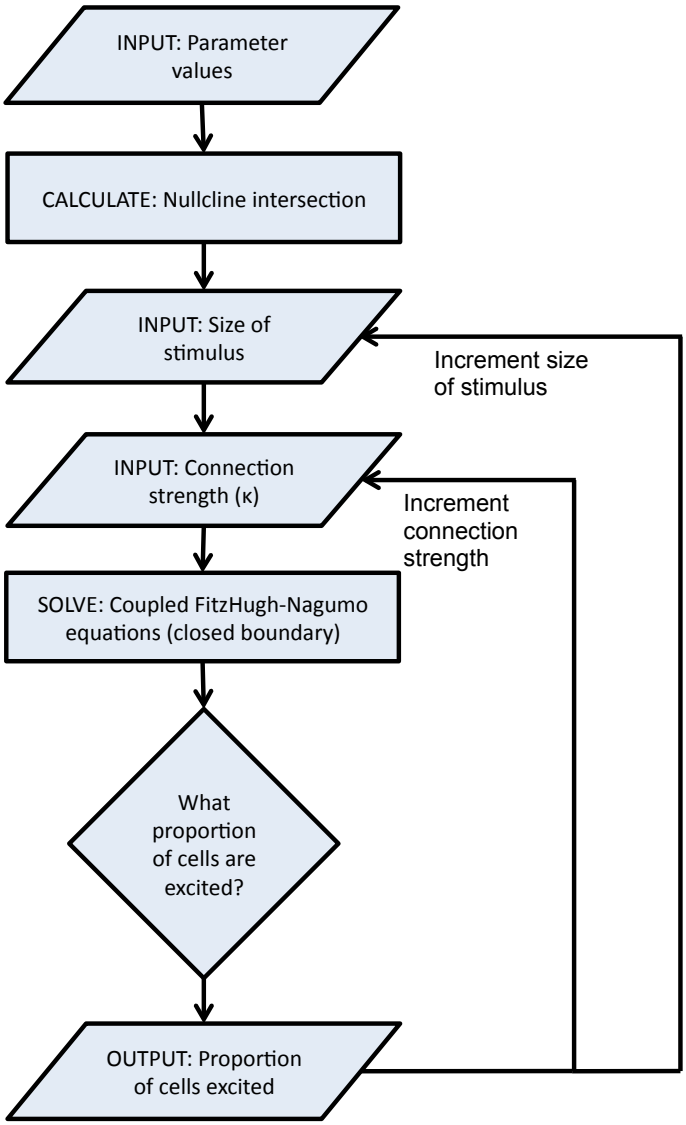

Figure A.1: Flow chart representing the fully connected lattice simulations.

A.2 Symmetrical coupling — the Bernoulli Lattice

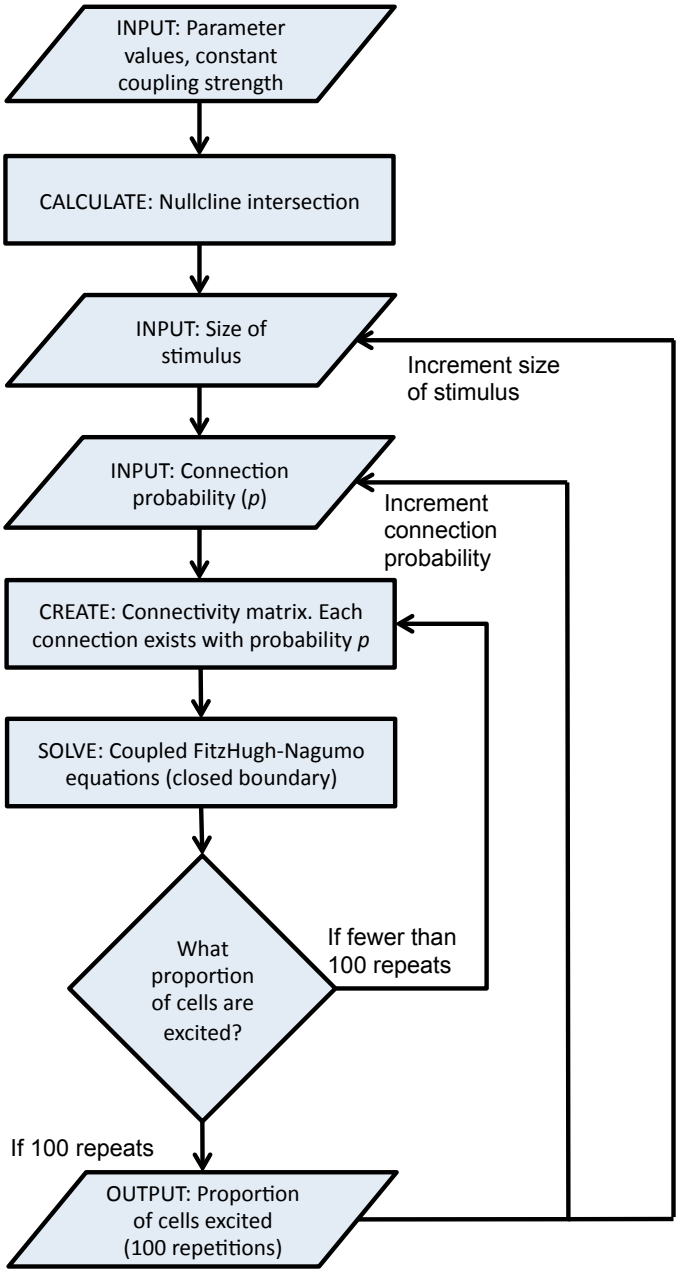

Figure A.2: Flow chart representing the Bernoulli Lattice simulations.

A.3 Symmetrical coupling — Uniformly distributed

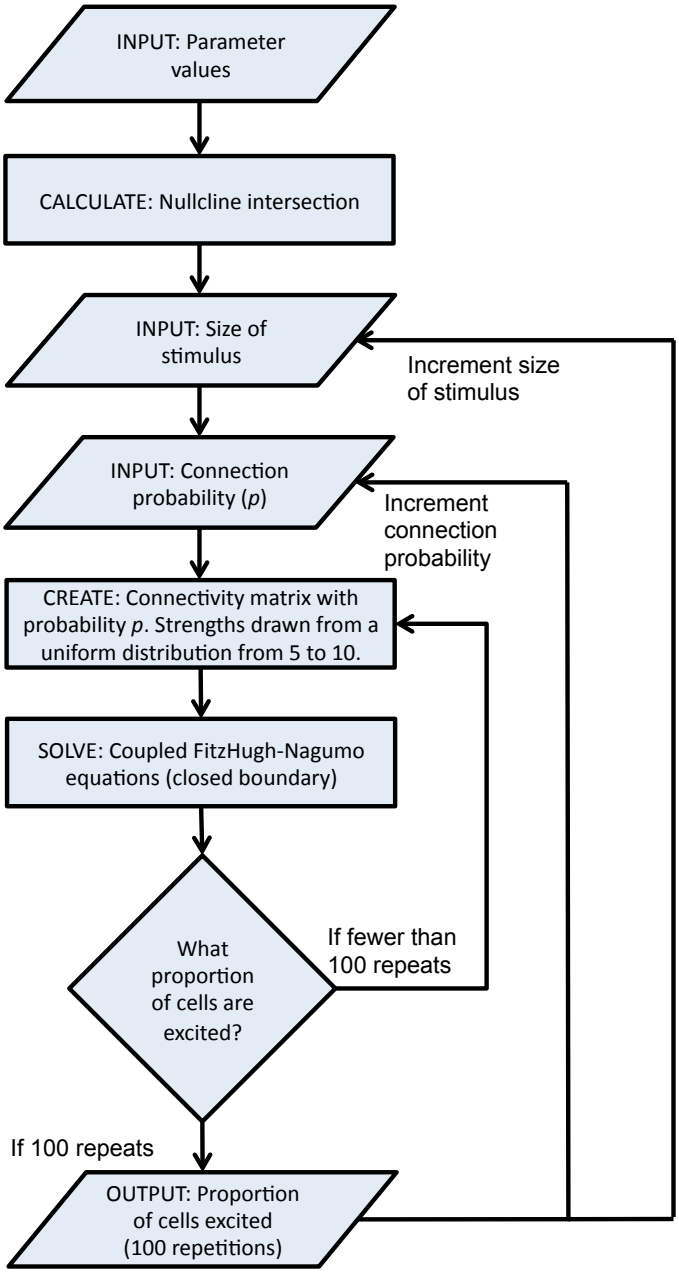

Figure A.3: Flow chart of simulations with uniformly distributed connection strengths.

A.4 Spatial correlation

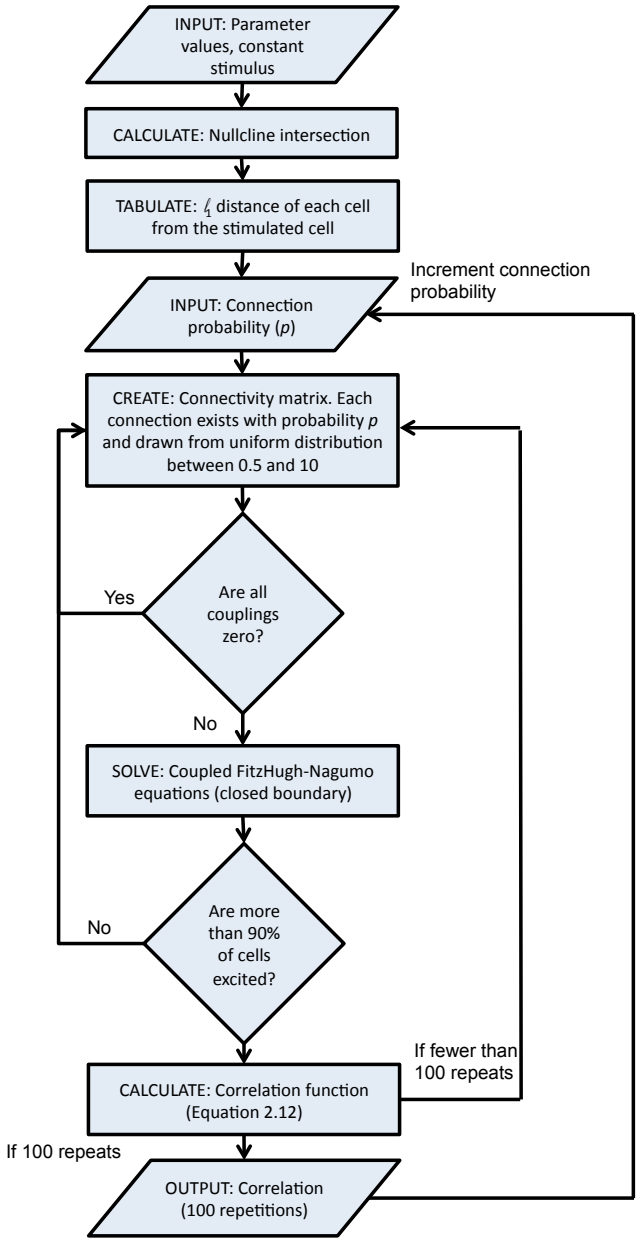

Figure A.4: Flow chart of simulations for determining spatial correlation. Repeat, replacing "Are more than 90 % of cells excited?" with "Are fewer than 10 % of cells excited?"

A.5 Asymmetrical coupling — Cell capacitance

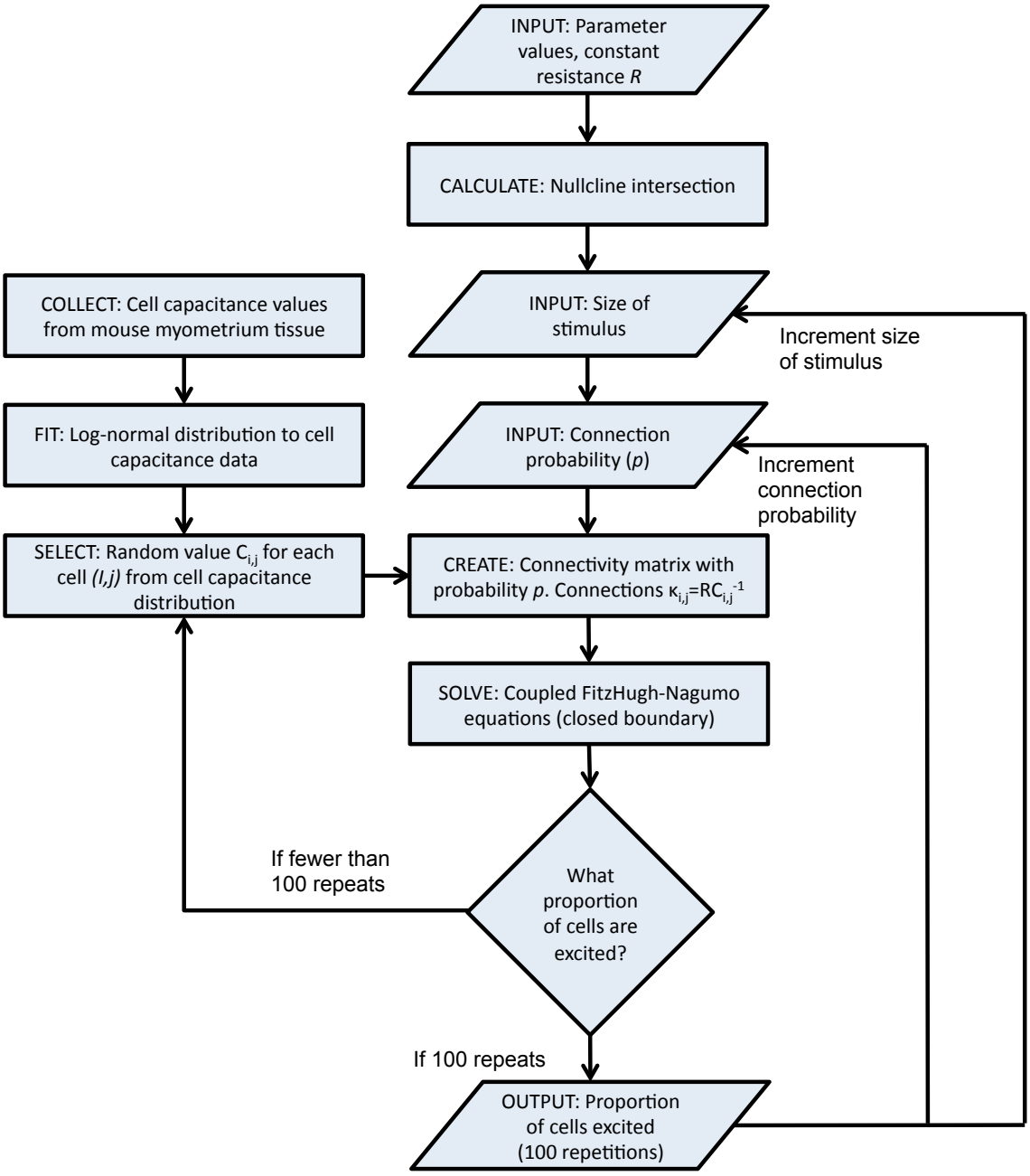

Figure A.5: Flow chart of simulations with experimental cell capacitance data.

A.6 Variation in resting membrane potential

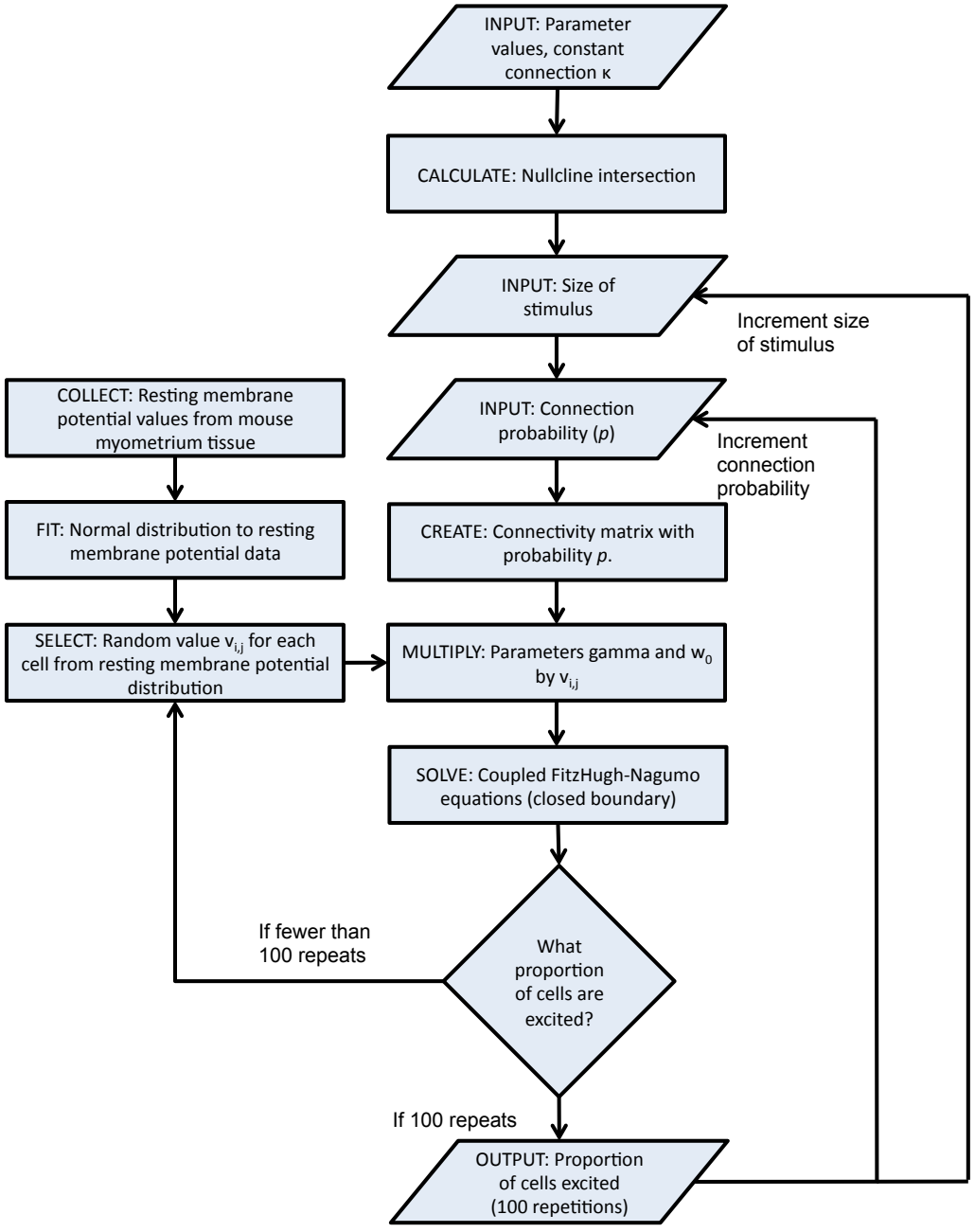

Figure A.6: Flow chart of simulations with resting membrane potential data.

A.7 Combining cell capacitance and resting membrane potential

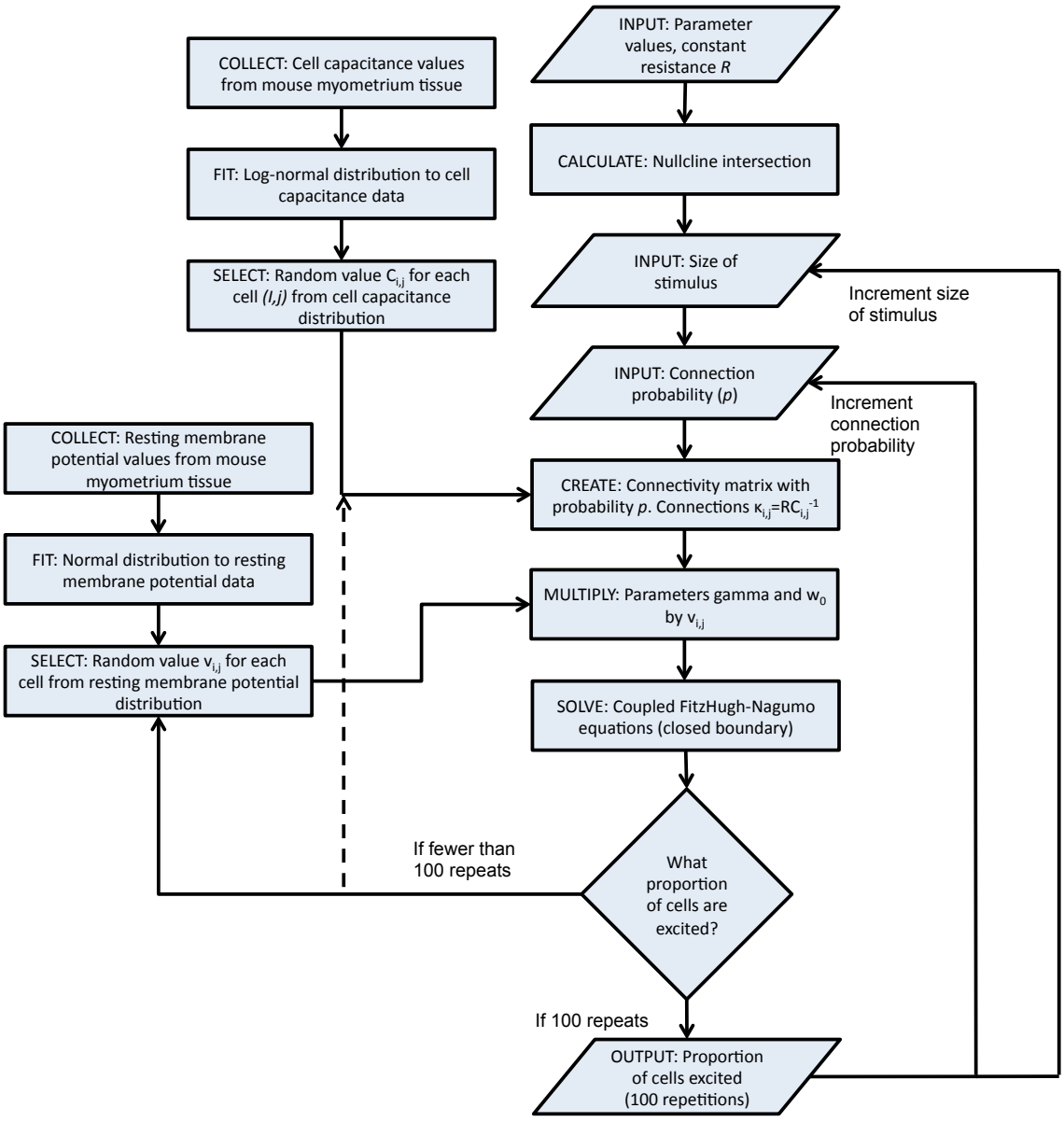

Figure A.7: Flow chart of simulations with both cell capacitance and resting membrane potential data.

A.8 Pacemaker cells

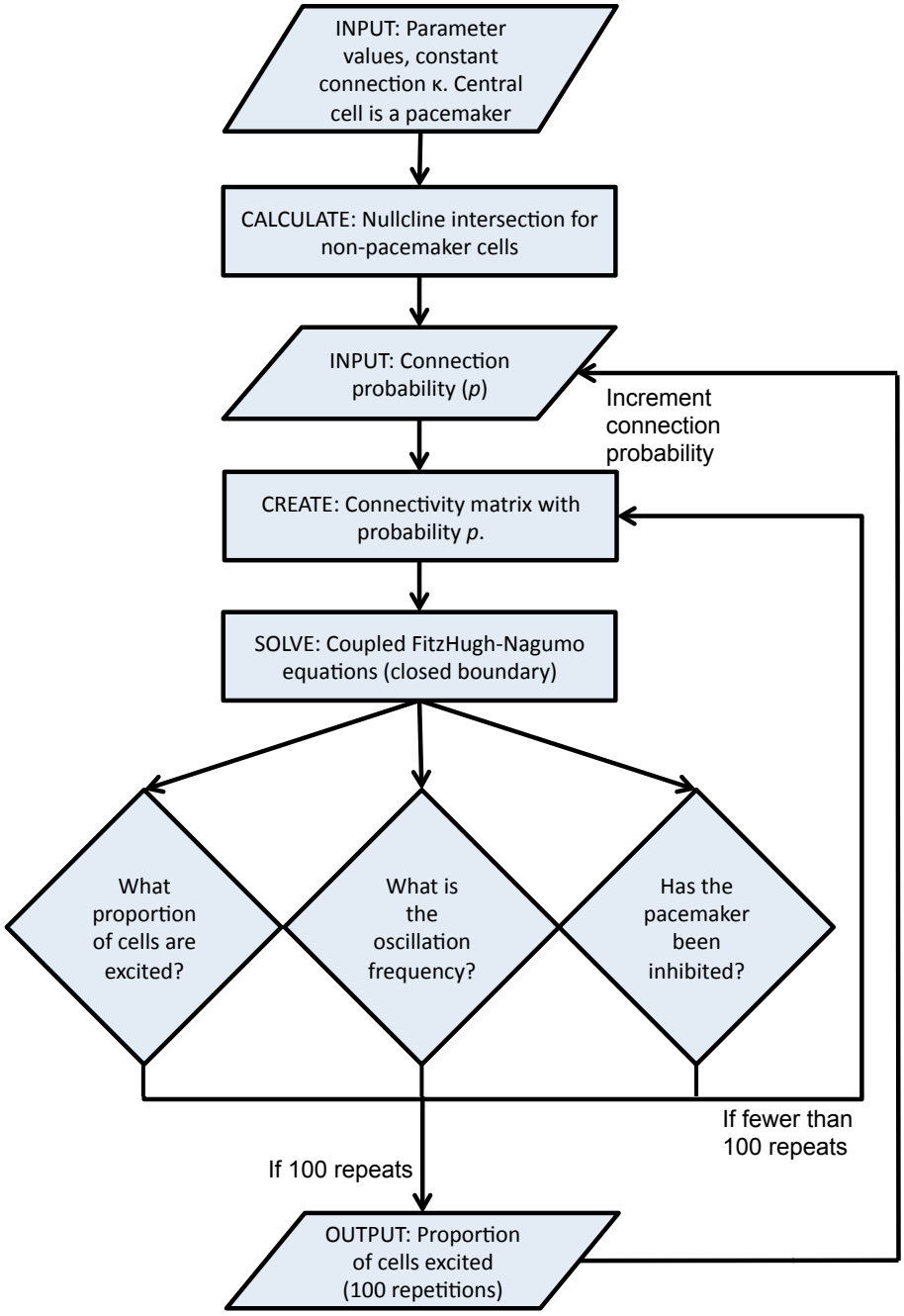

Figure A.8: Flow chart of simulations with a pacemaker as the inciting stimululs.

A.9 Voltage-dependent gap junctions

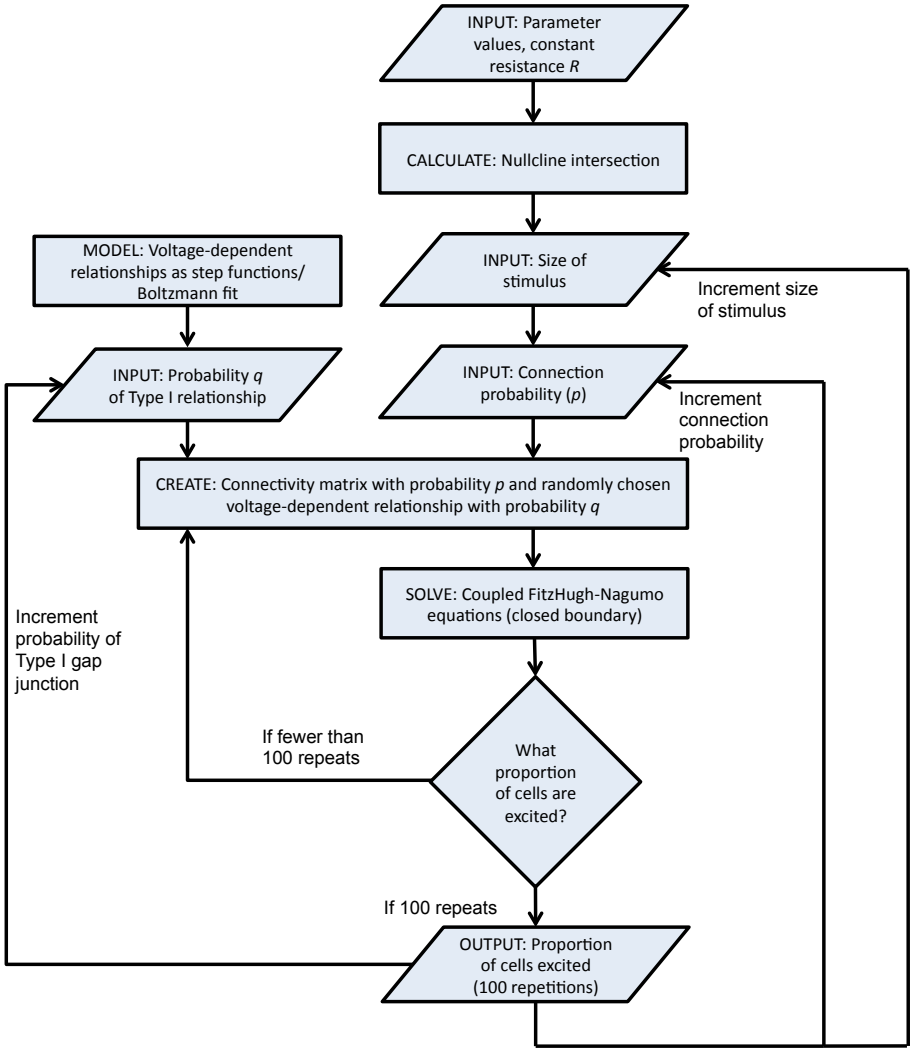

Figure A.9: Flow chart of simulations with voltage-dependent gap junctions. The process is the same regardless of step function model or Boltzmann distribution fit. Models with gating kinetics are dealt with in a similar fashion with additional state variables when solving the FitzHugh-Nagumo equations – there is now a conductance variable for each inter-cell connection which is associated with the Type I/Type II selection.